Photons, Missing Energy and the Quest for Supersymmetry at the LHC

Dissertation
zur Erlangung des Doktorgrades
des Departement Physik
der Universität Hamburg

vorgelegt von
Ulla Gebbert
aus Hamburg

Hamburg
2012

Gutachter der Dissertation:	Prof. Dr. Peter Schleper Prof. Dr. Teruki Kamon
Gutachter der Disputation:	Prof. Dr. Johannes Haller Dr. Isabell Melzer-Pellmann
Datum der Disputation:	21.3.2012
Vorsitzender des Prüfungsausschusses:	Priv. Doz. Dr. Michael Martins
Vorsitzender des Promotionsausschusses:	Prof. Dr. Peter Hauschildt
Leiter des Departments Physik:	Prof. Dr. Daniela Pfannkuche
Dekan der Fakultät für Mathematik, Informatik und Naturwissenschaften:	Prof. Dr. Heinrich Graener

Abstract

In this thesis a search for supersymmetry in events with at least one photon, jets and missing transverse energy ($\not\!\!E_{\mathrm{T}}$) in an integrated luminosity of $4.32\,\mathrm{fb}^{-1}$ of pp collisions at $\sqrt{s}$ =7 TeV is presented. The data is recorded by the CMS detector in 2011. Final states with photons are expected in models with gauge mediated supersymmetry breaking, where the lightest supersymmetric particle is the gravitino. The gravitino leaves the detector without energy deposition and thus leads to missing transverse momentum in the event.

$\not\!\!E_{\mathrm{T}}$ is crucial to distinguish the signal from the Standard Model events and is reconstructed from all energy deposits in the detector. Due to the non-linearity of the response in the calorimeter, additional corrections are required. In this thesis, a data driven technique to determine the correction for unclustered energy deposits, using the transverse momentum balance between a Z boson and the hadronic recoil, is presented.

For the search for supersymmetry the $\not\!\!E_{\mathrm{T}}$ distribution measured in data is compared to the expected Standard Model distribution. For this purpose the main Standard Model background processes from QCD multi- and photon-jet or electro-weak processes are modelled using data events. No excess over the Standard Model expectation is observed. Exclusion limits at the 95% CL are set and interpreted in the GMSB parameter space.

Zusammenfassung

Diese Arbeit zeigt eine Suche nach supersymmetrischen Endzuständen mit mindestens einem Photon, Jets und fehlender transversaler Energie. Endzustände mit Photonen werden in supersymmetrischen Modellen mit eich-induzierter Brechung (GMSB) vorhergesagt. Hierbei ist das leichteste supersymmetrische Teilchen das Gravitino, welches keine Energie im Detektor hinterlässt und so zu fehlender transversaler Energie im Ereignis führt.

Die fehlende transversale Energie berechnet sich aus allen gemessenen Energiedepositionen der verschiedenen Detektorkomponenten. Aufgrund des nicht linearen Ansprechverhaltens des hadronischen Kalorimeters müssen zusätzlich Korrekturen angewandt werden, um ein Maß für die tatsächlich fehlende transversale Energie zu erhalten. Hier wird eine datengetriebene Methode vorgestellt, mit der Korrekturen für die nicht in Jets zusammengefassten Energiedepositionen aus $Z \to ee$-Daten berechnet werden können. Die in ca. $36\,\mathrm{pb}^{-1}$ 7 TeV Daten gemessene Korrektur wird vorgestellt und die resultierende fehlende transversale Energie in verschiedenen Ereignistopologien diskutiert.

Die Suche nach Supersymmetrie wurde mit $4.32\,\mathrm{fb}^{-1}$ Proton-Proton-Kollisionen durchgeführt, die 2011 mit dem CMS-Detektor am LHC aufgezeichnet wurden. Die gemessene Verteilung der fehlenden transversalen Energie wird mit der im Standard-Modell vorhergesagten Verteilung verglichen. Hierzu werden die erwarteten Hauptuntergründe mit datengetriebenen Methoden vorhergesagt. Die Messung zeigt keine signifikante Abweichung von der Standard-Modell-Erwartung. Die Ergebnisse werden im Rahmen der eich-induzierten Brechungsmodelle interpretiert und Ausschlugrenzen mit einer statistischen Sicherheit von 95% berechnet.

Contents

1

Introduction

Since the start of planning in the late 1980s, particle physicists have been eagerly awaiting the start up of the 'Large Hadron Collider' (LHC), the world's largest circular particle collider. After a construction phase of more than 10 years, the first proton-proton collisions at the LHC finally took place in November 2009. Since March 2010 the LHC has been operated at a centre-of-mass energy ($\sqrt{s}$) of 7 TeV[1], opening unprecedented possibilities to search for physics within and beyond the Standard Model.

The Standard Model of particle physics is an experimentally very well probed theory of the elementary particles and their interactions. But it leaves many important issues like, e.g. the origin of dark matter unsolved. This raises the question about a possibly more fundamental theory like, e.g. supersymmetry (SUSY). Many theories beyond the Standard Model predict a variety of new particles with masses in the energy regime accessible at the LHC ($\lesssim 1\,\text{TeV}$). The 'Compact Muon Solenoid' (CMS) is one of four particle detectors built to record and analyse the proton-proton collisions at the LHC. In 2010 and 2011 it recorded $\sim 5\,\text{fb}^{-1}$ collisions at $\sqrt{s} = 7\,\text{TeV}$.

In this thesis a search for supersymmetry at CMS in events with at least one photon is presented. Photons are produced naturally in SUSY models with gauge-mediated supersymmetry breaking (GMSB) if the next-to-lightest SUSY particle (NLSP) is the neutralino. The neutralino NLSP can only decay into

[1] Here and in the following $\hbar = c = 1$ applies.

the gravitino, the lightest supersymmetric particle (LSP) and a neutral standard model boson. The created standard model boson is either a photon, or if the mass difference between the NLSP and the LSP is large enough, a Z or a Higgs boson. The branching fraction depends on the neutralino mixing matrix. Both, the single photon final states as well as the diphoton final states, are of interest for SUSY pair production, because one photon might not be detected due to the limited geometrical or kinematical acceptance of the detector. Furthermore eventually only one neutralino NLSP decays into a photon, while the other decays via a Z or a Higgs boson into leptons or predominantly into jets[1]. The case of a charged NLSP, i.e. a stau, is not studied in this thesis.

In supersymmetric models the LSP usually interacts gravitationally or via the weak interaction, i.e. in GMSB models the LSP is the graviton. Thus it is expected to leave the particle detectors of the LHC without any energy deposit. The magnitude of the resulting transverse momentum imbalance ($\not\!\!E_{\mathrm{T}}$) is an important quantity to identify events where supersymmetric particles occur, and to distinguish them from Standard Model processes, where only neutrinos lead to such an imbalance. Thus a good understanding of the $\not\!\!E_{\mathrm{T}}$ measurement and knowledge about the instrumental causes for high $\not\!\!E_{\mathrm{T}}$ is crucial for all searches for supersymmetry.

Technically the measurement of the momentum imbalance is very challenging, as it is sensitive to electronic noise, limited resolution and geometrical or kinematical acceptance of the detector. Furthermore, the non-linearity of the response in the calorimeter for neutral and charged hadrons, together with other instrumental effects, introduces a bias in the measurement of missing transverse momentum. To remove this bias the energy deposits clustered in jets are corrected in a first correction step, while the remaining 'unclustered' energy deposits are corrected in a second step.

After a short phenomenological introduction to the Standard Model and a short outline of the basic concepts of supersymmetry, the possible final states with photons at the LHC are discussed in more detail in Chapter 2. The event

[1] In case of a small mass difference between the lightest chargino and neutralino the lightest chargino will also decay directly via a W boson.

reconstruction with the CMS detector, including the reconstruction and identification of particles, is described in Chapter 3.

The measurement of the missing transverse energy is discussed in Chapter 4, where a method to derive the corrections to the unclustered energy deposits from $Z \to ee$ events is presented. The resulting $\not\!\!E_{\mathrm{T}}$ scale and resolution are measured in different event topologies. Furthermore two important causes of artificial high $\not\!\!E_{\mathrm{T}}$ are discussed: punch-through of high energetic jets and contributions due to non-functioning detector regions.

In Chapter 5, the search for supersymmetry in final states with at least one photon, jets and missing transverse momentum is presented. This includes a data driven estimation of the main Standard Model backgrounds. These are direct photon-jet production and QCD multi-jet production, where one jet fakes a photon and background due to electroweak electron production, i.e. $W \to e\nu$, where one electron fakes a photon. The expected Standard Model background is compared to the events observed in $4.32\,\mathrm{fb}^{-1}$ of data for different signal regions and the obtained results are interpreted in the GMSB parameter space.

2

Theoretical Background

The Standard Model of Particle Physics (SM) [1] is a description of the elementary particles and their fundamental interactions. It is a experimentally very well probed theory which has shown its strength with the early prediction of particles discovered in later experiments, e.g. the W and Z boson (1983 [2; 3]), the top quark (1995 [4; 5]) and the τ neutrino (2000 [6]).

Although the Standard Model has been incredibly successful in explaining the experimental results, there are many important issues not solved in the Standard Model. Probably the most conspicuous one is the predicted but not yet discovered Higgs particle, which is needed to account for the masses of particles.

A theoretically well motivated extension of the Standard Model is supersymmetry (SUSY), but so far there is no experimental evidence for this theory. At the LHC a possible production of supersymmetric particles leads to a wide variety of final states - including those with at least one photon, jets and missing transverse momentum.

After a short phenomenological introduction to the Standard Model and a discussion of some of its caveats, the basic concept of supersymmetry is outlined in this chapter. The focus is given to supersymmetric models with gauge mediated SUSY breaking and the resulting possible experimental signatures with photons following David Shihs (et al.) work [7; 8; 9]. Sec. 2.1 is mainly based on [10], while Sec. 2.1.1 and 2.2 mostly rest on [11] and [12].

2.1 The Standard Model

Within the Standard Model particles are classified in two categories: bosons and fermions. Matter consists of fermions which carry a half-integer spin and are further split into leptons and quarks. Bosons have integer spin and act as mediators of the three fundamental forces described within the Standard Model:

- The **electromagnetic force** is mediated by photons between all particles with electric charge.
- The **weak force** has three massive bosons acting as a mediator (W^+, W^- and Z^0). The way particles interact under the weak force is determined by their weak isospin I_3. The weak isospin of a particle depends on its handedness or chirality, which for massless particles corresponds to its helicity state[1]. All left-handed fermions as well as the W and Z bosons take part in the weak interaction.
- The **strong force** is mediated by gluons between all coloured particles. Colour is the charge of the strong force, which is carried by all quarks and gluons. The Standard Model describes three colours: red, blue and green.

The Standard Model consists of six leptons grouped in three generations classified by their charge (Q), electron number (L_e), muon number (L_μ) and tau number (L_τ). The first generation consists of the electron (e^-) and its electromagnetic neutral partner, the electron neutrino (ν_e), both carrying a electron number of +1. Similarly the muon (μ^-) and the muon neutrino (ν_μ) fall into the second generation ($L_\mu = +1$), while the tau (τ^-) and tau neutrino (ν_τ) build the third generation ($L_\tau = +1$). There are also six antileptons with reversed charge and lepton number.

Similarly, there are six quarks classified by their charge and flavour grouped again in three generations. The first generation consists of the up- and down-quark (u,d), the second of the strange- and charm-quark (s,c) and the third

[1]The helicity describes the direction of the spin with respect to the direction of flight. Particles with positive helicity are called right-handed, particles with negative helicity left-handed

generation holds the bottom- and top-quark (b,t). The u, c and t quarks have a charge of $+\frac{2}{3}$, while the d, s and b quarks carry a charge of $-\frac{1}{3}$. As for the leptons, all quarks have a corresponding antiparticle with reversed charge and flavour. Furthermore, each quark comes in three colours.

In each lepton and quark generation the left-handed partners form a weak isodoublet with a isospin $I_3 = \pm 1/2$, while the right handed fermions have $I_3 = 0$ and thus are isospin singlets.

Mathematically the Standard Model is a quantum field theory, describing the interaction between the particles with gauge symmetries. The gauge group of the Standard Model is $SU(3)_C \otimes SU(2)_L \otimes U(1)_Y$. Here, $SU(3)_C$ is the gauge group of the strong force, while $SU(2)_L \otimes U(1)_Y$ combines the electromagnetic and weak forces.

The gravity is not yet included in the Standard Model as there is no complete quantum theory available. However, the assumed mediator of gravity is called graviton, and often mentioned also in the context of the Standard Model.

Spontaneous Symmetry Breaking and the Higgs Mechanism

To ensure local gauge invariance the gauge fields have to be massless as it is the case for the strong and electromagnetic interaction. However, the gauge bosons of the weak force, the W and Z bosons, are known to have a mass around 80, respectively 91 GeV [13]. To still accommodate the massive gauge fields in a local gauge invariant theory, the mechanism of spontaneous symmetry breaking and the Higgs Mechanism needs to be included.

Spontaneous symmetry breaking occurs if the ground state of the system does not share the symmetry of the Lagrangian. In the Standard Model the spontaneous symmetry breaking is caused by the Higgs field [14; 15; 16], where the potential function of the corresponding complex SU(2) doublet Φ is described by:

$$V(\Phi) = -\mu^2 \Phi^* \Phi + \frac{1}{4}\lambda(\Phi^* \Phi)^2 \tag{2.1}$$

where μ and λ are real parameters. The minima of the potential lie on a circle of radius

$$|\Phi| = \sqrt{2}\mu/\sqrt{\lambda} \equiv v/\sqrt{2}, \tag{2.2}$$

so that for low energies the symmetry is broken as illustrated in Fig. 2.1.

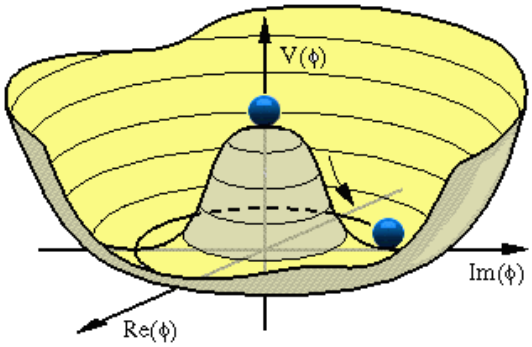

Figure 2.1: Higgs potential function (Eq. 2.1) [17]

This minimal value is the expectation value of the quantum field in the quantum vacuum, called vacuum expectation value. The parameter v in Equation 2.2 sets, in principle, the scale of all masses in the Standard Model, which get their masses by coupling to the Higgs field.

Accordingly the mass of the Higgs boson itself is, neglecting radiative corrections,

$$M_H = v\sqrt{\frac{\lambda}{2}}, \tag{2.3}$$

where λ is the strength of the Higgs self-interaction in the higgs potential (Eq. 2.1).

Measurements of other Standard Model parameters set the weak scale v to

$$v \approx 246 \text{ GeV}. \tag{2.4}$$

Without assuming a very large self-interaction in the higgs sector[1], this sets the Higgs boson mass to be in the order of a few hundred GeV. However, the Higgs boson is the only Standard Model particle which has not been discovered so far in any experiment. The lower bound on the Higgs boson mass has been set to $m_H \geq 114.4$ GeV at the 95% confidence level by the LEP experiments [18]. Recent results from the CMS collaboration exclude Higgs boson masses between

[1]The possibility of a large self-interaction is generally not favoured as non-pertubative calculations would be introduced, and these are difficult to handle.

127 GeV and 600 GeV at the 95% confidence level [19]. At the low end of the explored mass range (110-600 GeV) an excess of events observed for hypothesised Higgs boson masses makes the observed limits weaker than expected[1]. More data is needed to ascertain the origin of this excess. The ATLAS collaboration reports similar results [20].

Electroweak Unification

The combination of the gauge theory of the electromagnetic force (quantum electrodynamics, QED) and the weak force is described in the Glashow-Salam-Weinberg model [21; 22; 23] within a $SU(2)_L \otimes U(1)_Y$ gauge group. The charge of $SU(2)_L$ is the weak isospin and the corresponding gauge mediators are three massless W bosons (W^1,W^2,W^3). The $U(1)_Y$ has one massless gauge boson, the B^0. The charge of the $U(1)_Y$ is called weak hypercharge. As described above the Higgs Mechanism leads to a spontaneous symmetry breaking of the electroweak symmetry and thus to a mixing of the four massless bosons to the three massive mediators of the weak force (W^+,W^-,Z^0) and the massless mediator of the electromagnetic force, the photon (γ):

$$|W^{\pm}\rangle = |W^1\rangle \pm i|W^2\rangle \tag{2.5}$$

$$|\gamma\rangle = \cos\ \theta_W|B^0\rangle + \sin\ \theta_W|W^3\rangle \tag{2.6}$$

$$|Z^0\rangle = -\sin\ \theta_W|B^0\rangle + \cos\ \theta_W|W^3\rangle \tag{2.7}$$

The angle θ_W is the Weinberg angle described by the couplings of the two forces. Due to the dependence on θ_W the mass of the $W^{\pm}$ boson (M_W) and the Z^0 boson (M_Z) differ, and can be described by:

$$M_Z = \frac{M_W}{cos\ \theta_W}. \tag{2.8}$$

The mass scale of the W and Z boson depends on the vacuum expectation value of the Higgs field $v/\sqrt{2}$ and the gauge coupling constant g of the $SU(2)_L$

[1] The expected exclusion range was 117-543 GeV.

group. E.g. the mass of the $W^{\pm}$, without the inclusion of radiative corrections, is given by:

$$M_W = gv/\sqrt{2} \sim 80 \text{ GeV}. \tag{2.9}$$

The lifetime of the massive bosons is in the order of 10^{-25} s. After this time they decay predominantly into quarks (70%) [13]. The relatively short lifetime leads to a reach of the weak force in the order of $\sim 10^{-18}$ m.

The coupling of the electroweak force is not constant, but dependent on the distance between the two charges. For small distances the coupling increases, which can be physically interpreted as vacuum polarisation, where virtual electron-positron pairs interact with the photon partially screening the charge.

Quantum Chromodynamics

The strong force is described by a $SU(3)_C$ gauge group with a quantum field theory called quantum chromodynamics (QCD) [24]. The $SU(3)_C$ symmetry seems to be unbroken in nature. Within QCD the gauge bosons of the strong force, the gluons, are massless as they do not couple to the Higgs field. To ensure the gauge invariance of the theory eight gluon states occur, each carrying one of the three colours and an anticolour.

Similarly to the electroweak force the coupling of the strong force is not constant but depending on the distance between the coloured particles. As in the electroweak case part of the colour charge is screened by interactions with virtual quark-antiquark pairs and, again, the screening of the charge increases for small distances. However, for the strong force, a second effect plays an important role for the energy dependence of the strong coupling. This effect is called confinement and occurs due to the interaction between the gluons themselves. These additional gluon loops decrease the coupling of the strong force for short distances.

As the second effect is much stronger than the screening of the colour charge, the confinement leads to the fact that coloured particles, like quarks, can not be isolated and the coupling increases strongly with the distance between the particles. Therefore, the potential energy increases rapidly for large distances

between two coloured particles, which leads to the production of new quark-antiquark pairs. These couple with the original quarks to colourless bound states, which are not affected by the colour confinement. The resulting colourless bound states are classified in two categories: mesons, consisting of a quark and an antiquark with the same colour (or anti-colour), or, baryons, consisting of three quarks or antiquarks with different colour. Despite of the fact that the mediator bosons are massless, the confinement of the quarks leads to a very short reach of the strong force ($\sim 10^{-15}$).

On the other hand, for small distances, within the colourless bound states, the strong coupling becomes relatively weak, and the behaviour of the quarks can be described as if they were single, isolated particles, which is called asymptotic freedom.

2.1.1 Beyond the Standard Model

Although the Standard Model provides an experimentally well probed theoretical framework to describe the known particles and their electroweak and strong interactions[1], it possesses structural defects and it leaves many important issues unaddressed.

Unification of the Forces

The successful combination of the quantum field theories of the weak and the electromagnetic forces raises the question whether a further unification of the forces in one 'theory of everything' is possible. In Grand Unified Theories (GUTs) the strong interaction is linked to the electroweak interaction within a gauge group G with one single coupling. The group G consists of the gauge groups of the three unified forces:

$$G \subset SU(3)_C \otimes SU(2)_L \otimes U(1)_Y. \tag{2.10}$$

In the GUTs the coupling of the three forces converge at a common value at extremely high energies in the order of $M \gtrsim 10^{15}\,\mathrm{GeV}$. The energy where the

[1] Already in this description one of the caveats of the Standard Model becomes clear - gravity, the fourth fundamental interaction is not yet included as no adequate quantum field theory has been developed yet.

unification occurs is called GUT scale. Below this scale the symmetry of the group G is spontaneously broken, leading to the known running of coupling constants as described in the Standard Model.

Though theoretically very interesting, the Standard Model in its current version is not a GUT theory as the extrapolation of the couplings in the Standard Model does not lead to a unification at high scales.

Dark Matter

Several cosmological experiments have shown that the universe seems to constitute of much more than visible matter [25]. To account for this dark matter was postulated and it is assumed that it contributes to ∼23% of the energy in the universe [26]. However, the consistence of dark matter, not interacting electromagnetically, is widely unknown until today. The neutrino is an example of hot dark matter within the Standard Model, as it interacts, besides gravity, only via the weak force. However, hot dark matter is not able to explain the formation of galaxy clusters and the observed galactic rotational curves. Futhermore, the mass of the neutrino is much too small to explain the large amount of dark matter observed by the experiments, which leaves the question about the origin of dark matter unsolved within the Standard Model.

Naturalness of the Standard Model

In Sec. 2.1 the discussion about the masses in the Standard Model and their dependence from the weak scale v has been at tree level without considering any higher order loop corrections. Due to the renormalisability of the Standard Model the theory should deliver finite results for all higher-order correction. However, at least at very high energies near the Planck scale ($\sim 10^{19}$ GeV) significant contributions from gravity are expected. But, even if we just assume that the Standard Model is valid up to a scale Λ very different from the weak scale v, higher order corrections lead to large corrections of the Higgs boson mass for every Standard Model particle that couples to the Higgs field. For example the Higgs self interaction at one-loop order leads to a positive correction $\sim \lambda\Lambda^2\Phi^*\Phi$

to the mass term $-\mu\Phi^*\Phi$ in Eq. 2.1. The coefficient $-\mu^2$ can then be replaced by the more physical, one-loop corrected value $-\mu^2_{phys}$:

$$-\mu^2_{phys} = -\mu^2 - A\lambda\Lambda^2. \tag{2.11}$$

A is a numerical factor, which is not important for the main argument — the corrected mass term in the Higgs potential, and thus the Higgs boson mass itself depends on the square of the scale Λ[1]:

$$M_H = \sqrt{2}\mu_{phys}. \tag{2.12}$$

As discussed above, the physical Higgs boson mass needs to be in the order of ~ 100 GeV to reach the phenomenologically fixed value of v. For a large scale of Λ, e.g. the Planck scale, this relies on a remarkable cancellation in the order of 10^{-34} between the Lagrangian parameter $-\mu^2$ and Λ^2. This high-level of needed fine-tuning of the parameters doubts the naturalness of the Standard Model in its current version.

In addition to the discussed caveats the large number of free parameters in the model, like the masses of the quarks and leptons, the mass differences between the generations and the number of generations itself, indicate that there might be a more fundamental theory about the particles and their interactions. In this context many theories have been discussed - but until now no significant experimental evidence for either has been found.

2.2 Supersymmetry

Supersymmetry (SUSY) is a theoretically well motivated candidate for an extension of the Standard Model introduced in the early 1970s. It introduces a new symmetry between bosons and fermions by using an algebra with a generator Q changing the spin of each particle by $\frac{1}{2}$ and thus changing bosons to fermions and vice versa:

$$Q|\text{boson}\rangle = |\text{fermion}\rangle, \text{Q}|\text{fermion}\rangle = |\text{boson}\rangle \tag{2.13}$$

[1] Ultimately all Standard Model masses depend on v and thus on μ_{phys}.

Each supermultiplet, which is an irreducible representation of the supersymmetric algebra, contains fermion and boson states and contains an equal number of fermionic and bosonic degrees of freedom. Particles in one supermultiplet are called superpartners and have the same mass. As the generator of supersymmetry commutes with the generator of gauge transformations, the superpartners have furthermore the same electrical charge, same isospin and same colour.

One of the main qualifying arguments for SUSY is that it solves the fine-tuning problem of the Standard Modelas first proposed in the early 1980s. If the coupling of bosons and fermions to the Higgs field is equal, the contributions from higher-order loop corrections cancel if there is a scalar particle with same mass for each Standard Model fermion. However, in the energy regime covered so far no sign of the supersymmetric particles has been found, which implies that supersymmetry is broken. Still the remaining contributions from higher-order corrections to $-\mu^2_{phys}$ are small, as long as the masses of the supersymmetric particles are not larger than $\sim$1 TeV[1].

Besides the hierarchy problem also some of the other caveats of the Standard Model can be solved within supersymmetric theories. In the beginning of the 1990s it was shown [27] that the supersymmetric particles change the coefficients in the renormalisation equation such that the couplings of the three forces described in the Standard Model unify at energies around $\sim 2 \cdot 10^{16}\,\tilde{\text{GeV}}$ as shown in Fig. 2.2. Furthermore some of the new particles are good candidates for dark matter particles [28].

2.2.1 The Minimal Super Symmetric Standard Model

The minimal supersymmetric extension of the Standard Model is called Minimal Supersymmetric Standard Model (MSSM). It is only one of many possible SUSY models, but it is called minimal as it introduces only one new degree of freedom in the superspace.

[1] In this case the theory is still renormalisable and the corrections to $-\mu^2_{phys}$ are depending only logarithmically on Λ. This is called soft SUSY breaking and its assumption is one of the reasons to search for SUSY at the LHC, where sparticles masses up to the TeV scale should be visible in the experiments.

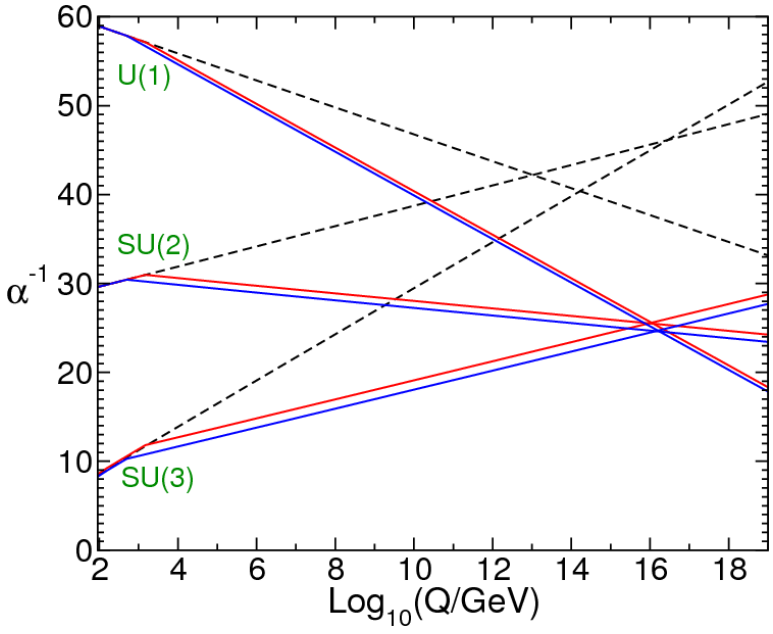

Figure 2.2: Two-loop renormalisation group evolution of the inverse gauge couplings in the Standard Model (dashed lines) and the MSSM (solid lines).

Particles in the MSSM

As the number of fermionic and bosonic degrees of freedom is equal in each multiplet, the minimal extension of the Standard Model leads to one superpartner for each Standard Model particle. The superpartners of the fermions with two helicity states (L,R) form a chiral multiplet with a boson (spin 0) as their superpartner. The bosons of the Standard Model (spin 1) are combined with their superpartner, a fermion (spin 1/2), in a gauge multiplet. To complement the SUSY particle spectrum the graviton (spin 2) is added in another supermultiplet together with its superpartner the gravitino (spin 3/2). The superpartners of the Standard Model particles are denoted with a ˜ above the corresponding Standard Model notation. The partners of the fermions are called sfermions, e.g. selectron ($\tilde{e}$), smuon ($\tilde{\mu}$), stau ($\tilde{\tau}$), etc., while the partners of the gauge bosons are called gauginos, e.g. gluino ($\tilde{g}$), wino ($\tilde{W}$), etc..

In the Standard Model the Higgs sector is described by one Higgs doublet, while in the MSSM two Higgs doublets are needed to give mass to all particles.

One of the doublets H_u couples only to up-type quarks, while the other H_d couples only to down-type quarks. The two Higgs doublets with their superpartners have eight degrees of freedom. Three are needed to give mass to the Standard Model $W^{\pm}$ and Z boson, while the others build five Higgs particles by mixing between the Higgs doublets. This results in three neutral superpositions of the H_u and H_d (two scalar Higgs particles (h^0,H^0) and a pseudoscalar A^0), and two charged Higgs bosons ($H^{\pm}$) originating from the mixture of the H_u^+ and H_d^-.

As in the Standard Model, the supersymmetric eigenstates of the theory are not necessarily the mass eigenstates, but broken symmetries can lead to a mixing between particles with same quantum numbers. The gluino is the only gauge boson which can not mix with any of the other gauginos, but the higgsinos mix with the supersymmetric partners of the electroweak bosons. Electroweak symmetry breaking leads to a mixing of the superpartners of the neutral wino ($\tilde{W}^0$), the bino ($\tilde{B}^0$) and the higgsinos ($\tilde{H}_u^0$,$\tilde{H}_d^0$) to four neutral mass eigenstates, the neutralinos ($\tilde{\chi}_{1...4}^0$):

$$\begin{pmatrix} \tilde{\chi}_1^0 \\ \tilde{\chi}_2^0 \\ \tilde{\chi}_3^0 \\ \tilde{\chi}_4^0 \end{pmatrix} = \begin{pmatrix} M_1 & 0 & -c_\beta\ s_W\ m_Z & s_\beta\ s_W\ m_Z \\ 0 & M_2 & c_\beta\ c_W\ m_Z & -s_\beta\ c_W\ m_Z \\ -c_\beta\ s_W\ m_Z & c_\beta\ c_W\ m_Z & 0 & -\mu \\ s_\beta\ s_W\ m_Z & -s_\beta\ c_W\ m_Z & -\mu & 0 \end{pmatrix} \begin{pmatrix} \tilde{W}^0 \\ \tilde{B}^0 \\ \tilde{H}_d^0 \\ \tilde{H}_u^0 \end{pmatrix} \tag{2.14}$$

with $c_\beta \equiv \cos\beta$,$s_\beta \equiv \sin\beta$,$c_W \equiv \cos\theta_W$ and $s_W \equiv \sin\theta_W$. θ_W is the Weinberg angle and $\tan\beta$ the ratio between the vacuum expectation values of the two Higgs doublets. m_Z is the mass of the Z boson, while $M_{1,2}$ are the mass parameters of the wino and bino. μ is the Higgs boson mass parameter.

Similarly the charged higgsinos and winos mix to two charged mass eigenstates, the charginos ($\tilde{\chi}_{1,2}^{\pm}$):

$$\begin{pmatrix} \tilde{\chi}_1^+ \\ \tilde{\chi}_2^+ \end{pmatrix} = \mathbf{X} \begin{pmatrix} \tilde{W}+ \\ \tilde{H_u}^+ \end{pmatrix}, \begin{pmatrix} \tilde{\chi}_1^- \\ \tilde{\chi}_2^- \end{pmatrix} = \mathbf{X} \begin{pmatrix} \tilde{W}- \\ \tilde{H_d}^- \end{pmatrix} \tag{2.15}$$

with

$$\mathbf{X} = \begin{pmatrix} M_2 & \sqrt{2}\ m_W\ \sin\beta \\ \sqrt{2}\ m_W\ \cos\ \beta & \mu \end{pmatrix} \tag{2.16}$$

Here θ_W, β ,M_2 and μ are denoted as above, while m_W is the mass of the W boson. The charginos and neutralinos are ordered in dependence of their masses, where the numbering starts with the lightest gaugino.

Not only the gauginos, but also the sfermion gauge eigenstates can mix and build new mass eigenstates if the mixing sfermions have the same colour and electrical charge. Neglecting the mixing between the first two generations of sfermions, the $MSSM$ introduces 35 new particles, which are summarised in Table 2.1.

Superpotential and R parity

The supersymmetric interactions are described with the so called superpotential:

$$W_{MSSM} = \bar{u} y_u Q H_u - \bar{d} y_d Q H_d - \bar{e} y_e L H_d + \mu H_u H_d \tag{2.17}$$

Here $\bar{u}$, Q, H_u, $\bar{d}$, H_d, e and L are the superfields of the corresponding supermultiplet[1], y_i are Yukawa matrices describing the mixing and coupling of scalars to fermions. μ is again the Higgs boson mass parameter.

In principle additional terms violating the lepton or baryon number are allowed. Therefore a new quantum number, the R parity is defined in supersymmetry:

$$P_R = (-1)^{3(B-L)+2S}, \tag{2.18}$$

where B is the baryon number, L the lepton number and S the spin quantum number. All Standard Model particles have $P_R = +1$, while all supersymmetric particles have $P_R = -1$. If R parity is conserved, this leads to the conservation of baryon and lepton numbers. As a result in a collision of Standard Model particles supersymmetric particles can only be produced in pairs. Furthermore the final state of the decay of a supersymmetric particle always contains a stable supersymmetric particle, the lightest supersymmetric particle (LSP). In some SUSY breaking models the LSP is a good candidate to explain the origin of dark matter [28], which would solve one of the main open questions of the Standard Model.

[1] $\bar{u}$, Q and $\bar{d}$ are the supermultiplets containing squarks and quarks, while L and e describe the sleptons and leptons. Respectively H_d and H_u contain the Higgs and higgsino particles.

Name	Spin	P_R	Gauge Eigenstates	Mass Eigenstates
Higgs Bosons	0	+1	$H_u^0\ H_d^0\ H_u^+\ H_d^-$	$h^0\ H^0\ A^0\ H^\pm$
Squarks	0	-1	$\tilde{u}_L\ \tilde{u}_R\ \tilde{d}_L\ \tilde{d}_R$ $\tilde{s}_L\ \tilde{s}_R\ \tilde{c}_L\ \tilde{c}_R$ $\tilde{t}_L\ \tilde{t}_R\ \tilde{b}_L\ \tilde{b}_R$	see left see left $\tilde{t}_1\ \tilde{t}_2\ \tilde{b}_1\ \tilde{b}_2$
Sleptons	0	-1	$\tilde{e}_L\ \tilde{e}_R\ \tilde{\nu}_e$ $\tilde{\mu}_L\ \tilde{\mu}_R\ \tilde{\nu}_\mu$ $\tilde{\tau}_L\ \tilde{\tau}_R\ \tilde{\nu}_\tau$	see left see left $\tilde{\tau}_1\ \tilde{\tau}_2\ \tilde{\nu}_\tau$
Neutralinos	1/2	-1	$\tilde{B}^0\ \tilde{W}^0\ \tilde{H}_u^0\ \tilde{H}_d^0$	$\tilde{\chi}_1^0\ \tilde{\chi}_2^0\ \tilde{\chi}_3^0\ \tilde{\chi}_4^0$
Charginos	1/2	-1	$\tilde{W}^\pm\ \tilde{H}_u^+\ \tilde{H}_d^-$	$\tilde{\chi}_1^\pm\ \tilde{\chi}_2^\pm$
Gluino	1/2	-1	$\tilde{g}$	$\tilde{g}$
Gravitino	3/2	-1	$\tilde{G}$	$\tilde{G}$

Table 2.1: The particles of the MSSM. The mixture between the first and second sfermion generation is neglected. The four Higgs bosons ($P_R = +1$) are no supersymmetric particles, but an extension of the Standard Model Higgs sector.

2.2.2 Gauge Mediated Breaking of Supersymmetry

Possible soft breaking terms added to the superpotential of the MSSM are quite constrained in order to ensure the renormalisability of the theory and avoid the reintroduction of quadratic divergences. Nevertheless 105 additional free parameters are needed to characterise the SUSY breaking terms. The SUSY breaking is assumed to take place in a sector, separate from the visible particles, called 'hidden' sector. Different models of SUSY breaking have been studied; one appealing breaking scenario called $mSUGRA$ (minimal supergravity) assumes that the interaction between the hidden sector and the Standard Model particles is gravitational.

Another one, called GMSB (gauge mediated SUSY breaking), introduces a second hidden sector containing messenger fields for the communication between the hidden sector and the visible particles [29]. Hereby the messenger fields underlie the Standard Model gauge interactions and couple to the SUSY breaking hidden sector. All soft mass breaking terms arise dynamically and depend on the scale of the messenger fields M_{mess} and the scale of SUSY breaking in the hidden sector F.

Gauge mediation is a very attractive scenario for the MSSM as it solves the SUSY flavor problem, by naturally suppressing flavour-changing neutral currents due to the Standard Model gauge interaction between the messenger fields and the visible sector[1]. Furthermore it provides a calculable framework, which allows the derivation of a phenomenological predictive framework.

Recently a model-independent framework for GMSB was formulated: General Gauge Mediation (GGM) [7]. This allows to identify features of GMSB in general and make predictions for possible final states observable at the LHC.

GGM encompasses all models where the theory decouples into the MSSM and a separate hidden SUSY breaking sector in the limit that the MSSM gauge couplings $\alpha_i \to 0$. This includes models with both, weakly and strongly coupled messenger fields, where any number of messenger and SUSY breaking fields can be accommodated. However, models based on nontrivial embeddings of the Standard

[1] In other models, like mSUGRA, the corresponding couplings have to be set to zero to avoid lepton flavour violation.

Model gauge group into larger groups are not included (e.g. $SU(5)_{GUT}$). The Higgs sector is not discussed in detail, but it is just assumed that tan β and μ can be set freely [9].

Within the framework of GGM the most common predictions of all GMSB models can be derived. These include, among others[1], a gravitino LSP with a light mass in the order of $\sim$ eV - GeV:

$$m_{LSP} = \frac{F}{\sqrt{3}M_{pl}}, \tag{2.19}$$

where m_{LSP} is the mass of the gravitino, M_{pl} is the Planck scale and F the SUSY breaking scale introduced above.

Widely known features like a bino or stau NLSP can be part of a large set of models, while they are not in general a prediction of gauge mediation. This is important as the NLSP type is one of the key quantities determining the inclusive signatures at a collider if R-parity conservation is assumed. In this case the NLSP always decays into its Standard Model partner plus the gravitino. These decays can be prompt or delayed depending on the interaction between NLSP and the gravitino. Thus, besides the type of the NLSP, also its lifetime τ_{NLSP} is strongly influencing the collider signatures:

$$\tau_{NLSP} \sim \frac{F^2}{m^5_{\mathrm{NLSP}}}. \tag{2.20}$$

In the following the decay of the NLSP to the gravitino is assumed to be prompt. This results in final states with high p_{T} objects (determined by the NLSP type) and missing transverse energy due to the gravitino leaving the detector without any energy deposition. A schematic Feynman diagram of a typical GGM event at a collider is shown in Fig. 2.3.

At the LHC the typical production will be coloured superpartners, e.g. squarks and gluinos. Their decays will produce Standard Model particles, mostly quarks, and end with a decay of the NLSP to its Standard Model partner and a gravitino. As within the GGM framework the type of the NLSP is not limited, it results in a very rich variety of possible final states [9]. This includes possible final states with high p_{T} photons if the NLSP is gaugino-like.

[1] see [7] for a complete list of common features

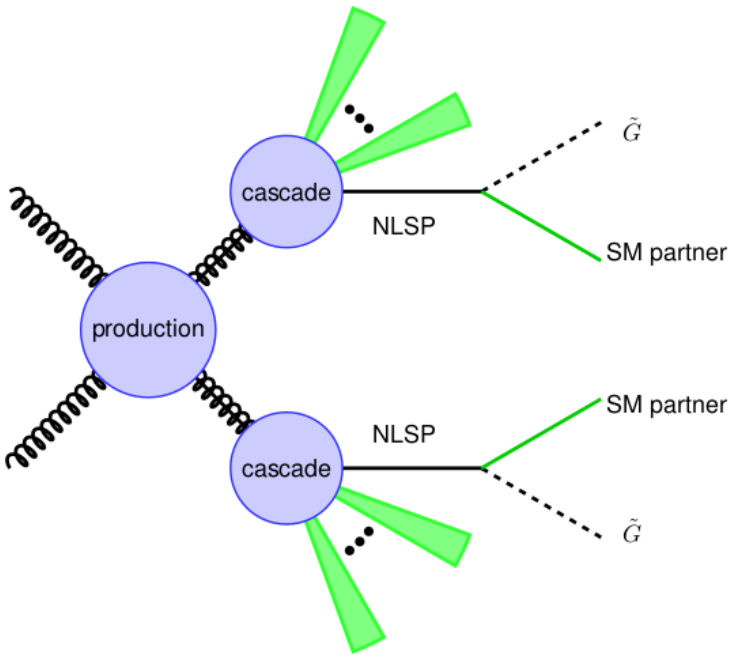

Figure 2.3: Schematic diagram [9] of a GGM event showing two decay chains ending with a decay of the NLSP to its Standard Model partner and a gravitino.

2.2.2.1 Experimental Signatures with Photons

Final states with photons are experimentally interesting as photons can be identified with relatively high purity and efficiency at the collider experiments. If in addition missing transverse energy occurs in the events as it is expected within GGM, the Standard Model background is widely suppressed which makes the channel experimentally well accessible.

If the NLSP is gaugino-like, in general, the NLSP will be a mixture of binos, winos and higgsinos. For simplicity the focus can be set on gauge eigenstate limits separating the possible final states for each gaugino. This leads to three different scenarios: bino-like NLSP, wino-like NLSP and higgsino-like NLSP[1]. To

[1]If the NLSP is a neutral higgsino it typically produces a Z or a h boson. The branching ratio is strongly model dependent, so that it is useful to define two extreme cases in which the higgsino decays only to Z or only to h plus gravitino as outlined here [8]

focus on final states with photons, models with higgsino-like neutralinos, where no photons in the final state are expected, are not discussed here further[1].

A bino-like neutralino decays predominantly in photons with a branching fraction $\sim \cos^2\theta_W$, while the decay to Z bosons is sub dominant ($\sim \sin^2\theta_W$). For a neutral wino-like neutralino the branching ratios are flipped, so that the decay goes dominantly to Z as shown in Fig. 2.4. The branching fraction of bino and neutral wino NLSPs is mostly determined by the Weinberg angle θ_W. In addition, at low masses, the decay to Z bosons is kinematically suppressed.

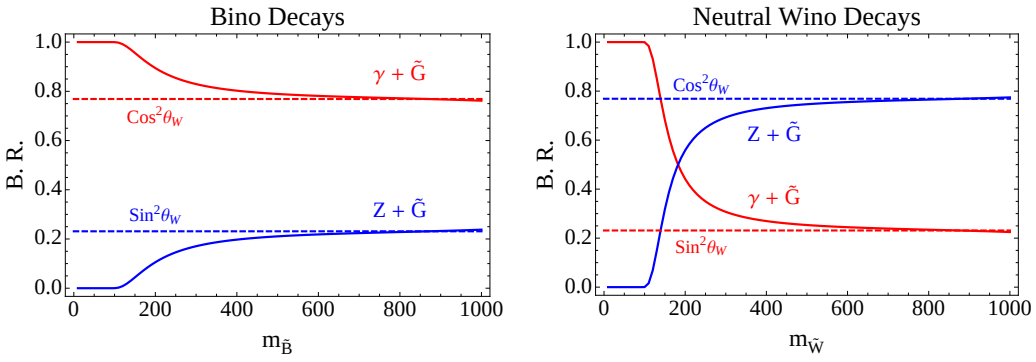

Figure 2.4: Branching ratio of bino- and wino-like neutralino to photons and Z bosons in dependence of the neutralino mass [8].

If the neutralino is wino-like, the splitting between the charged and the neutral wino is generally small [30] and thus the neutral and charged winos become co-NLSPs. In this case the charged wino will also decay directly into the gravitino and a $W^{\pm}$ [8].

As discussed in Sec. 2.2.1 R-parity conservation leads to pair production of supersymmetric particles and thus two NLSPs are expected in each event. Therefore the most likely final state for a pure bino-like neutralino contains two photons and two gravitinos plus eventually produced additional Standard Model particles. A Feynman diagram of such a decay is shown in Fig. 2.5. Besides this signature, final states with only one photon can occur if one of the NLSPs decays into a Z boson, instead of a photon. A corresponding Feynman diagram is shown in Fig. 2.6(a).

[1] see e.g. [8] and [9] for a detailed discussion of higgsino-like final states

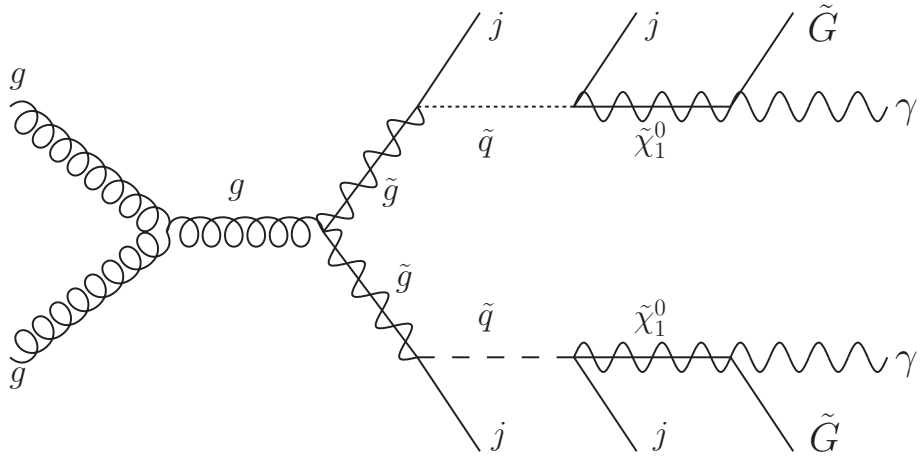

Figure 2.5: Sample Feynman diagram of an typical diphoton final state expected within the GGM framework for a bino-like neutralino.

Experimentally the search for final states with at least one photon is promising as it includes also the diphoton final states, which are not included in dedicated searches for the diphoton final state, where one of the photons fails the detector acceptance criteria.

For the wino-like NLSP the probability for a diphoton final state is quite suppressed. However, even if the wino-like neutralino is not decaying dominantly into photons, final states with a single high p_{T} photon still are not negligible, especially for low wino masses. This raises the opportunity to search for a wino-like neutralino in final states with one photon. An example Feynman diagram of such a decay is shown in Fig. 2.6(b). Compared to inclusive searches looking for hadronic final states (e.g. [31; 32]), this has the advantage of suppressed Standard Model backgrounds due to the clear experimental signature of the photon. First limits on the wino- and bino-like neutralino have already been set at the Tevatron [33; 34], but the LHC experiments have by now superseeded these limits as summarised here [9].

To allow the calculation of cross sections as model independent as possible the GGM predictions can be formulated in a simplified scenario as discussed in detail here [8; 35]. The main idea is to use minimal spectra, which include the NLSP, together with squarks and gluinos for coloured production. All other masses

are assumed to be decoupled[1]. All squark flavours are set to be approximately degenerate except for right-handed up-type squarks, which are decoupled. The production is assumed to be coloured production, i.e. squark and gluino production, as the production cross sections are much larger than for direct production of the neutralinos [9].

For the interpretation of the search for supersymmetry in photon final states presented in chapter 5 two bino-like scenarios have been studied: one with a fixed neutralino mass of 375 GeV and varying squark and gluino masses, the other with a decoupled squark mass[2] and varying gluino and neutralino masses. For the interpretation of the results in a model with a wino-like neutralino only the scan in squark and gluino mass has been performed, while the neutralino mass has been set to 375 GeV as in the bino-like scenario. The three corresponding simplified GGM spectra are summarised in Table 2.2.

The resulting NLO cross sections[3] for both scenarios in the squark-gluino mass plane and in the neutralino-gluino plane are visualised in Fig. 2.7.

Table 2.2: Summary of studied GGM benchmark scenarios with a bino- and wino-like neutralino.

Parameter	Bino-like $\tilde{\chi}_1^0$		Wino-like $\tilde{\chi}_1^0$
fixed mass	$M_{\tilde{\chi}_1^0}$	$M_{\tilde{q}}$	$M_{\tilde{\chi}_1^0}$
$M_{\tilde{g}}$ [GeV]	400-2000	400-2000	400-2000
$M_{\tilde{q}}$ [GeV]	400-2000	2500	400-2000
$M_{\tilde{\chi}_1^0}$ [GeV]	375	150-1050	375
μ [GeV]	2500	2500	2500
tan β	2	2	2
$c\tau_{\text{NLSP}}$ [mm]	0.1	0.1	0.1

[1] In the simplified GGM spectra analysed here all decoupled masses are set to 2500 GeV.

[2] In this scenario all light squark masses are set to 2500 GeV.

[3] The NLO cross sections have been calculated with PROSPINO [36], the corresponding renormalisation uncertainties and the PDF uncertainty on the cross section are shown in App. A.1.1.

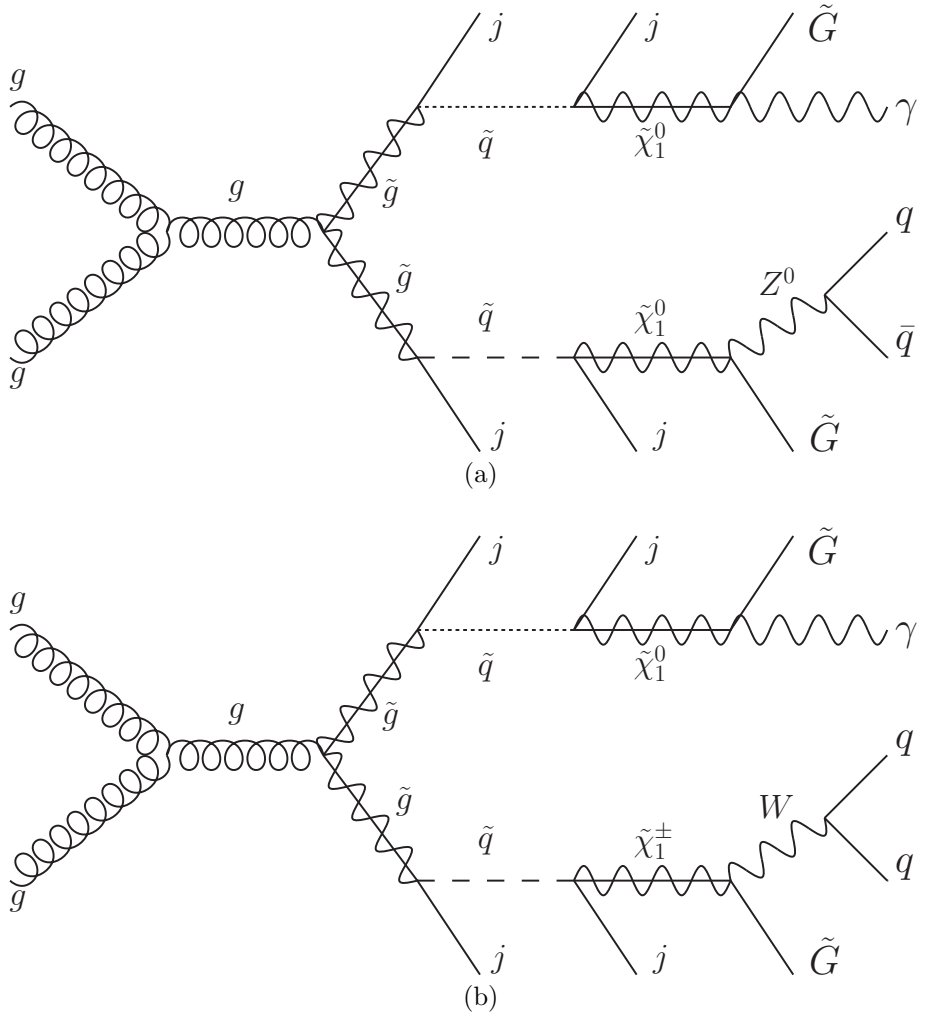

Figure 2.6: Sample Feynman diagram of an typical single photon final state expected within the GGM framework for a (a) bino-like and (b) wino-like neutralino.

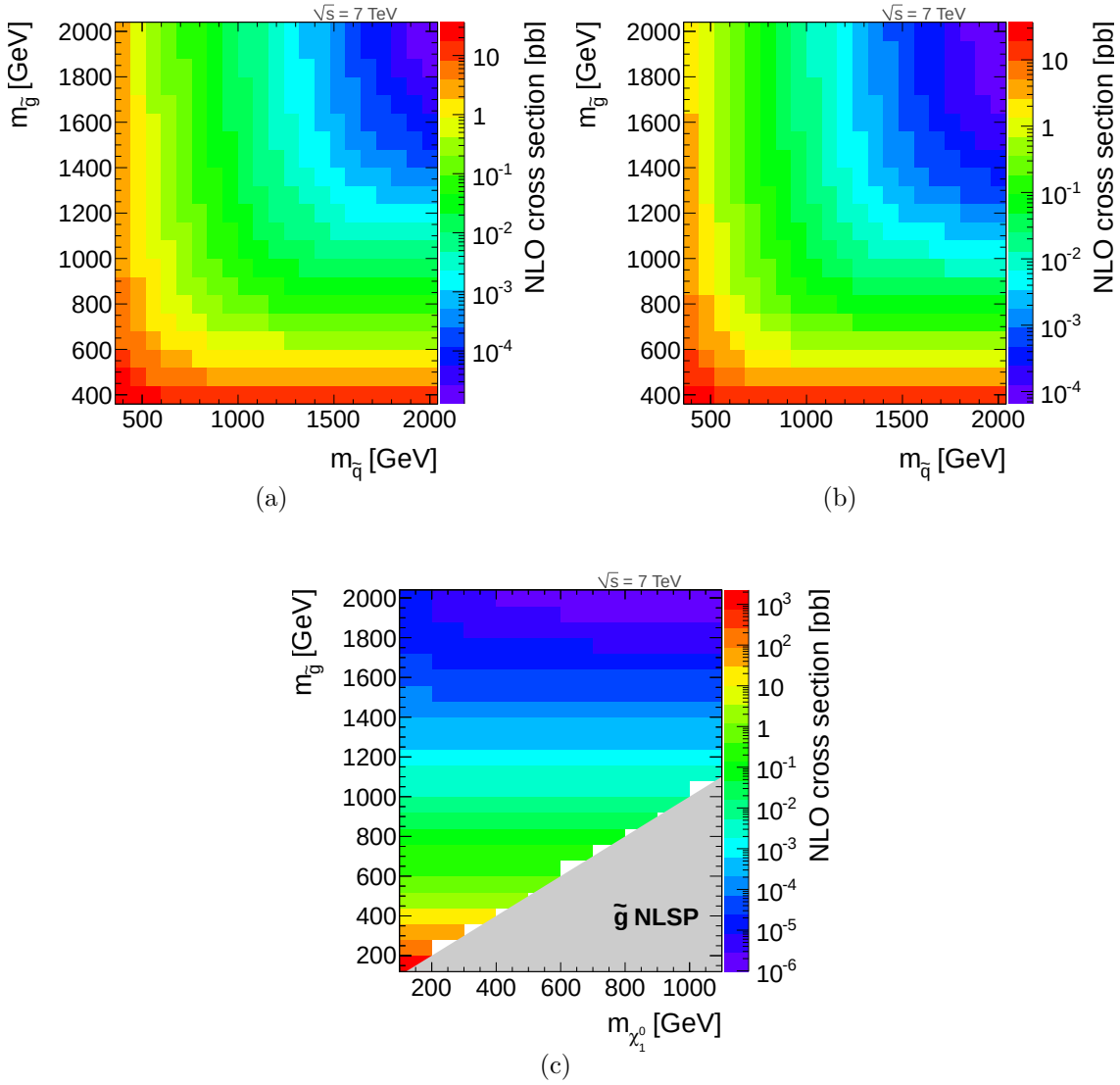

Figure 2.7: NLO cross sections in the squark-gluino mass plane of (a) bino- and (b) wino-like neutralino with mass $M_{\tilde{\chi}_1^0} = 375$ GeV and (c) in the neutralino-gluino mass plane of a bino-like neutralino.

3

Event Reconstruction with the CMS Detector

The Large Hadron Collider (LHC) [37] is a circular hadron collider designed for proton-proton collisions at a centre-of-mass energy of 14 TeV and a luminosity of $\mathcal{L} = 10^{34}\,\mathrm{cm}^{-2}\,\mathrm{s}^{-1}$. Besides protons, it can collide also heavy ions (Pb) with a maximum energy of 5.5 TeV and a luminosity of $\mathcal{L} = 10^{27}\,\mathrm{cm}^{-2}\,\mathrm{s}^{-1}$. The LHC is designed to reach these unprecedented energy scales, enabling the search for possible physics beyond the Standard Model and extending the reach of the ongoing search for the Higgs boson. Depending on the cross section of the physics process under study, σ, the expected number of events per second is $N = \mathcal{L}\sigma$, where $\mathcal{L}$ is the machine luminosity. For the LHC the luminosity is given by

$$\mathcal{L} = \frac{N_b^2 n_b f_{rev} \gamma}{4\pi\epsilon_n \beta^*} F, \tag{3.1}$$

where N_b is the number of particles per bunch, n_b the number of bunches per beam and f_{rev} the revolution frequency. γ is the Lorentz factor and F a reduction factor due to the crossing angle. The normalised transverse emittance, ϵ_n, is a measurement of the parallelism of the beam. Together with the beam size at the interaction point, β^*, it defines the width of the beam[1]. The design luminosity for proton collisions can be reached with 2808 bunches colliding every 25 ns.

[1]The nominal design luminosity corresponds to $\epsilon_n = 3.75$ μm and $\beta^* = 0.55$ m for proton-proton collisions.

The LHC is operated by the european organisation for nuclear research (CERN) and located near Geneva in the former 26.7 km tunnel of the LEP machine. It has two multiple-purpose experiments, ATLAS [38] and CMS [39], which are designed for the peak luminosity for proton-proton operation. Furthermore there are two experiments designed for lower luminosity: LHCb [40] focusing on b-physics and TOTEM [41] for the detection of protons from elastic scattering at small angles. The ALICE experiment [42] is optimised for the heavy-ion collisions and thus capable of running with the peak luminosity for this operation mode. Figure 3.1 shows an overview of the LHC and its experiments.

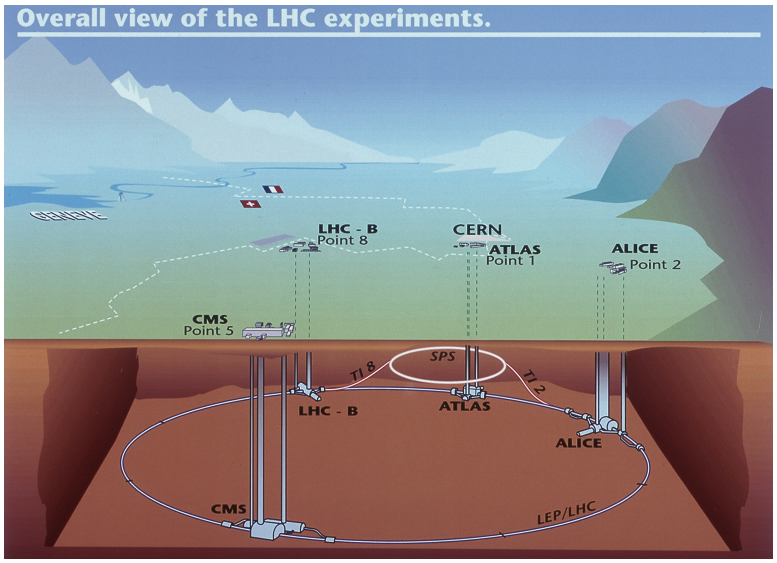

Figure 3.1: Overview of the LHC and its experiments [43].

The first proton-proton collisions took place in November 2009 at a centre-of-mass energy of 900 GeV. This was raised before the end of the year to 2360 GeV making the LHC the highest-energy particle accelerator on the earth. Since March 2010 the LHC has been operated at a centre-of-mass energy of 7 TeV. This energy is planned to be increased to 8 TeV in 2012. Then, after a two-year shut-down, the LHC is expected to be operated at the original design energy of 14 TeV in 2015. However, already during the runs in 2010 and 2011 the instantaneous luminosity has been increased steadily. This was achieved by tuning the beam parameters

leading to a maximum instantaneous luminosity of $\mathcal{L} = 3.55 \cdot 10^{33}\,\mathrm{cm}^{-2}\,\mathrm{s}^{-1}$ in October 2011. In 2010 CMS recorded a total integrated luminosity of $43\,\mathrm{pb}^{-1}$, whereas in 2011, due to the rapidly increasing luminosity, CMS recorded $5.2\,\mathrm{fb}^{-1}$of proton-proton collisions. The integrated luminosity versus time delivered to the LHC experiments in 2011 is shown in Fig.3.2 [44].

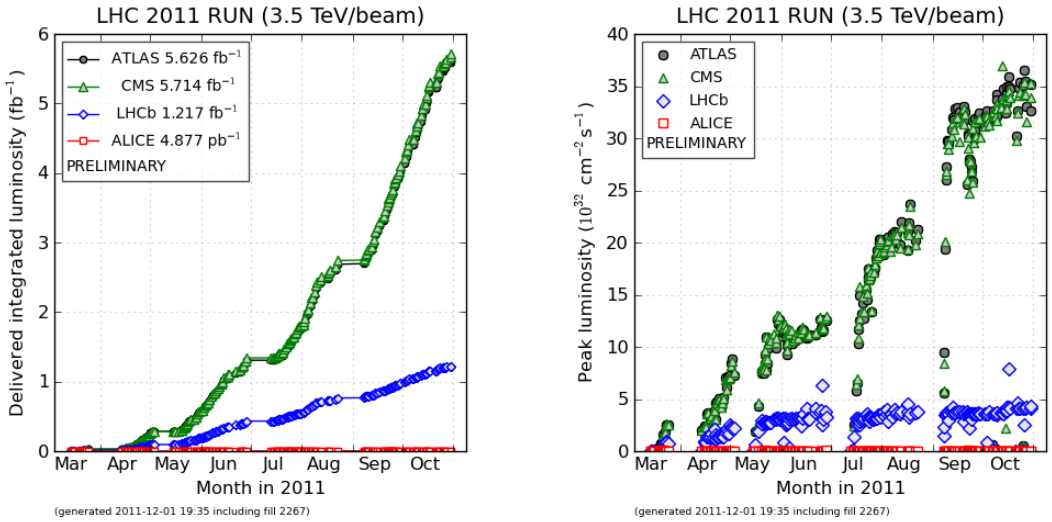

Figure 3.2: (a) Integrated and (b) peak luminosity versus time delivered to the LHC experiments in 2011[44].

3.1 Kinematic Definitions

CMS uses a right-handed coordinate system, with the origin in the centre of the detector. The x-axis is pointing to the centre of the LHC, the y-axis is pointing up, and the z-axis is pointing in the beam direction. The polar angle, θ, is measured from the z-axis, whereas the azimuthal angle, ϕ, is measured relative to the x-axis in the x-y-plane. The pseudorapidity η is defined as:

$$\eta = -\ln \tan(\frac{\theta}{2}). \tag{3.2}$$

The Lorentz invariant distance between two relativistic objects, ΔR , is given by:

$$\Delta \mathrm{R} = \sqrt{(\Delta\eta)^2 + (\Delta\varphi)^2}. \tag{3.3}$$

At the LHC, and all other hadron colliders, the initial momentum of the colliding particles is not known and consequently it is not possible to measure, e.g. the momentum balance of a collision directly. However, it is known that the initial particles have no momentum transverse to the beamline. Thus transverse quantities can be utilised to measure the energy and momentum of the particles. These quantities refer to the components in the x-y-plane, i.e. the transverse momentum, p_{T}, is:

$$p_{\mathrm{T}} = p \cdot \sin\,\theta \tag{3.4}$$

and transverse Energy, E_{T}, is:

$$E_{\mathrm{T}} = E \cdot \sin\,\theta. \tag{3.5}$$

Missing transverse momentum ($\vec{\not{E}}_{\mathrm{T}}$) is the vectorial sum of transverse momenta, while its magnitude is called missing transverse energy ($\not{E}_{\mathrm{T}}$).

3.2 The CMS Detector

The ambitious LHC physics programme focusing on the search for the Higgs boson and physics beyond the Standard Model sets high requirements for the experiments. The CMS detector [39] is designed to meet these requirements focusing on:

- a good resolution and reconstruction efficiency in the inner tracker for charged particles and an efficient triggering and tagging of τ's and b-jets. This is particularly important for the searches for the Higgs boson, e.g. $H \to b\bar{b}$ and searches for supersymmetry with b/τ-jets.

- a good electromagnetic energy resolution for the measurement of photons and electrons in a wide geometric coverage and an efficient photon and lepton isolation at high luminosities. This is again important for the Higgs searches ($H \to \gamma\gamma$), but also for searches for supersymmetry (GMSB) or new massive vector bosons ($Z' \to e^+e^-$).

- a good resolution of $\not{E}_{\mathrm{T}}$ and dijet mass requiring a hadronic calorimeter with a large hermetic coverage and with fine lateral segmentation. This is needed for many searches for new physics (e.g. supersymmetry), where often final states with large $\not{E}_{\mathrm{T}}$ are expected.

- a good identification of muons and their transverse momenta in a wide range of the detector, a good dimuon mass resolution and the possibility to measure the charge of the muon in the muon system. This allows, e.g. the search for heavy Higgs bosons in the four muon final state $H \to ZZ \to \mu^+\mu^-\mu^+\mu^-$ or the measurement of possible new massive vector boson ($Z' \to \mu^+\mu^-$).

The CMS detector is a typical cylindrical high-energy particle detector composed of several layers of subdetectors arranged around the beam line. One of the main distinguishing features of the CMS detector is the superconducting solenoid, providing a 3.8 T magnetic field, which is used to divert charged particles. The measure of the solenoid, 13 m long and 5.9 m inner diameter, drives the compact design of the CMS detector, accommodating inner tracker and the calorimetry inside the bore of the magnet coil and integrating also the muon system within the return yoke of the solenoid.

The different subcomponents of the detector sum up to a length of 21.6 m, a diameter of 14.6 m and a weight of 12500 tons. A schematic picture of the CMS detector and its subcomponents is shown in Fig. 3.3.

3.2.1 The Inner Tracker

The inner tracker measures charged particles within the $|\eta| < 2.5$ pseudorapidity range. To ensure a good resolution and measure possible secondary vertices from τ or b decays hybrid pixel detectors are installed close to the interaction vertex. In the barrel region three pixel layers at radii r of 4.4 to 10.2 cm are installed. Further away from the interaction point ($r \geq 20$ cm) the particle flux is low enough to enable the use of silicon microstrip detectors, which are placed at r between 20 and 110 cm in the barrel region of the detector. In addition the forward region is instrumented with 2 pixel and 9 microstrip layers.

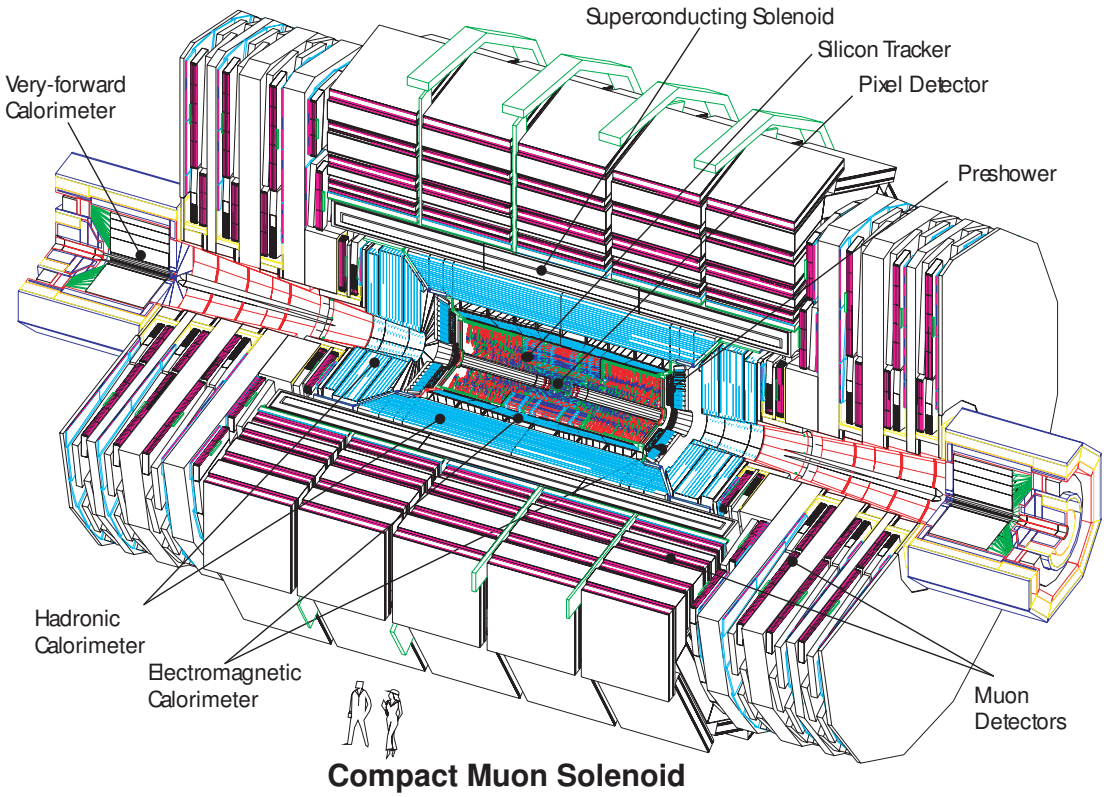

Figure 3.3: Schematic picture of the CMS detector and its subcomponents [39].

Overall the inner tracker consists of 1440 silicon pixel and 15148 silicon strip detector modules, providing an impact parameter resolution of ~ 15 μm and a p_{T} resolution of about 1.5% for 100 GeV particles [45].

3.2.2 The Electromagnetic Calorimeter

The electromagnetic calorimeter (ECAL) is located outside the inner tracker. It is used mainly to measure the energy of photons and electrons. It consists of 61200 lead tungstate crystals mounted in the central barrel part of the detector, completed by 7324 crystals in each of the two endcaps. The energy resolution of the ECAL is better than 0.5% for unconverted photons with $E_{\mathrm{T}} > 100$ GeV. The barrel region of the ECAL (EB) provides coverage in pseudorapidity $|\eta| < 1.479$, which is extended in the endcaps (EE) up to $|\eta| < 3.0$.

The lead tungstate crystals have short radiation lengths, are fast and radiation hard, which makes them very useful for LHC calorimetry. However, the light yield of the crystals is relatively low, which poses high requirements on the used photodetectors operated in the 4T magnetic field.

The basic building block of the ECAL front end electronics is a group of 25 crystals: a trigger tower in EB or a supercrystal in EE. The 25 crystals are grouped in a 5x5 geometry. Each trigger tower contains a motherboard (MB), a low voltage regulator board (LVRB), 5 very front end (VFE) boards and a front end (FE) card. Each VFE card contains amplification and digitisation for the signals from 5 crystals, the signals from the 5 VFEs are collected on the FE card. In the barrel each FE is served by three optical links: one for sending the data, one for the transfer of the trigger primitive measurement and a third link which transmits control, clock and trigger signals.

About 99% of the ECAL crystals have been fully operational during the 7 TeV data taking [46]. The remaining 1% of crystals are either non-functioning or have a high level of electronic noise and are thus masked for the reconstruction. While overall this has small impact on the event reconstruction, it becomes important for events with high $\not\!\!E_{\mathrm{T}}$ and high jet activity, where the probability that a jet hits an affected detector area is increasing.

3.2.3 The Hadron Calorimeter

The hadronic calorimeter (HCAL) is surrounding the ECAL, but still located mostly inside the magnet coil. To suppress non-Gaussian tails in the measurement of hadron showers and $\not\!\!E_{\mathrm{T}}$ it is important to avoid energy losses of the hadrons outside the calorimetry as far as possible. To achieve the required hermetic coverage the HCAL consists of four subdetectors: the hadron barrel (HB) and hadron endcap (HE) located inside the solenoid magnet cover a pseudorapidity range of $|\eta| < 1.4$ and $1.3 < |\eta| < 3.0$ respectively. The hadron forward (HF) lies close to the beam pipe but far from the interaction point covering very high pseudorapidities ($3 < |\eta| < 5$). The hadron outer (HO) ($|\eta| < 1.26$) is placed outside the solenoid, in the barrel region.

Besides the HF, the HCAL is a sandwich sampling calorimeter using brass as absorber material. Brass was chosen to maximise the amount of absorber inside the magnet and is well suited as it has a relatively short hadronic interaction length λ[1] and is not magnetic. The active medium consists of plastic scintillator tiles, which are read out with optical fibres connected to hybrid photodiodes (HPDs). In the HF the absorber material is steel. The hadrons emit Cherenkov light in radiation-hard Quartz fibres, which is read out and amplified by photomultipliers.

The material thickness of the HB in terms of hadronic interaction lengths reaches up to $\sim 10\ \lambda$ for $|\eta| \sim 1.3$. But for smaller pseudorapidities the material thickness decreases to a minimal thickness of $\sim 6\ \lambda$ in the central part of the HB. The ECAL adds $\sim 1\ \lambda$ in this region, but still late showering high energetic hadrons might punch-through the HB depositing parts of their energy outside. To measure parts of this leaking energy the HO is located outside the solenoid in the barrel region. But even including the HO very high energetic hadron showers might deposit parts of their energy further outside in the detector, e.g. the muon system. The material thickness in interaction lengths for the calorimetry and the muon system is shown in Fig. 3.4 in dependence of the pseudorapidity.

For $|\eta|$ <1.48 the HCAL cells map onto the 5x5 ECAL crystal arrays forming 'calorimeter towers'. For larger pseudorapidities the size of the towers increases and the corresponding ECAL cluster contains less crystals. The calorimeter towers are used to combine the measurement of ECAL and HCAL, resulting in the reconstruction of hadrons with a resolution of $\Delta E/E \approx 100\%/\sqrt{E[GeV]} \oplus 5\%$.

3.2.4 The Muon System

The Muon System is the outermost subsystem of the CMS detector. It is located outside the magnetic coil and integrated partly in the iron return yoke of the solenoid. It consists of four muon stations covering the region up to $|\eta| < 2.4$. In the muon barrel region (MB) aluminium drift tube chambers (DT) are used to ensure a high resolution measurement of the muons. The endcaps of the

[1]The interaction length is the distance in a material after which the energy loss of a relativistic particle due to nuclear interactions is reduced by a factor 1/e.

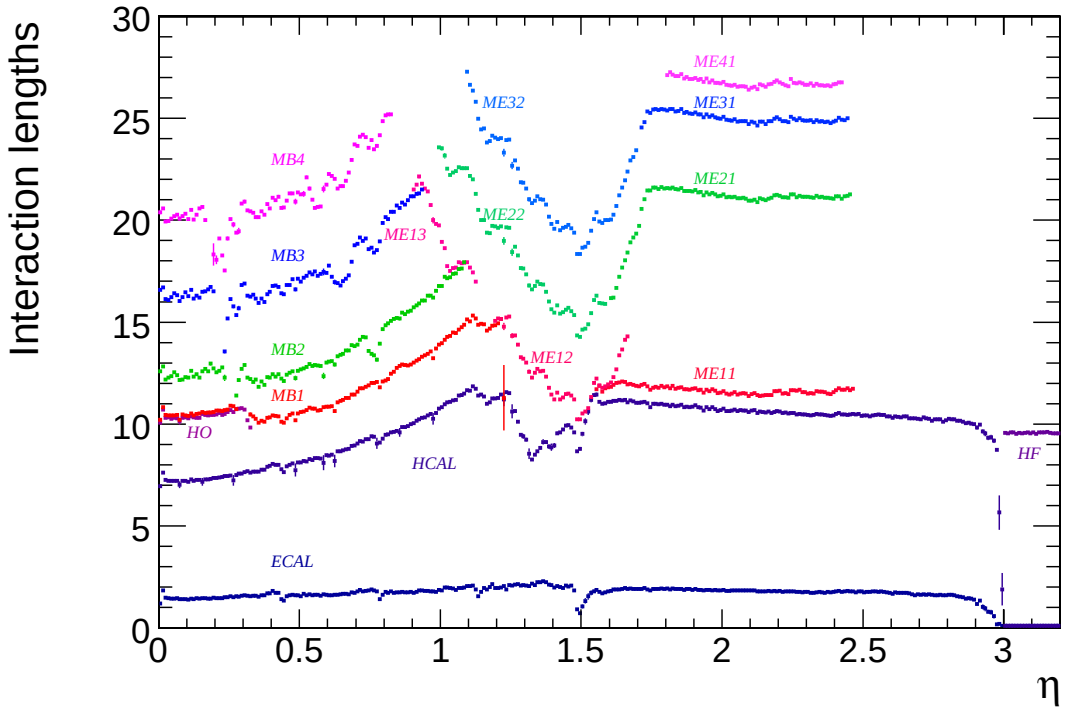

Figure 3.4: Material thickness in hadronic interaction lengths after the ECAL, HCAL, and at the depth of each of the four muon stations (MB,ME) as a function of pseudorapidity [39].

muon system (ME) are equipped with cathode strip chambers (CSCs). The CSCs provide a faster response time than the DTs, which is needed due to higher muon rates in the forward region. Resistive plate chambers (RPCs) are installed in both detector regions to complement the measurement of the CSCs and DTs. The RPCs have a much lower momentum resolution than the other muon detectors, but an excellent time resolution and a fast response time. Therefore, the RPCs are used to identify the correct bunch crossing. The muon detectors are arranged in both detector regions in 4 stations numbered from the inside out. Combining the track measurement in the inner tracker and the measurement from the muon system results in a p_{T} resolution between 1 and 5% up to a p_{T} of $\sim$1 TeV.

3.2.5 Trigger and Data Acquisition

The LHC bunch-crossing rate at the design luminosity of the LHC corresponds to $\sim 10^9$ interactions per second. This exceeds the available data processing rate, which is in the order of $\sim$300 Hz, by a factor of $\sim 10^7$. To achieve this drastic reduction factor CMS uses a two-level trigger system. The level-1 trigger (L1) [47] is composed of custom hardware processors. It uses information from the calorimeters and the muon system, where in a first step local triggers are activated if energy above a threshold is deposited in the calorimeter towers or track patterns are recognised in the muon system. The output of these local triggers is ordered by quality and forwarded to a global trigger, which decides if the event is processed further. The output rate of the L1 trigger is about 30 kHz with a total latency of less than 3.2 μs. The high level trigger (HLT) [48] builds the second stage of the trigger system and decreases the processed event rate to the required $\sim$300 Hz. It is a software trigger where different algorithms use almost the full event data, i.e. including also the information from the tracker. Several hundred HLT paths select different combinations of particles giving suitable input for the various CMS data analyses.

3.3 Event Cleaning and Basic Event Selection

A basic event selection and cleaning has been applied throughout all presented studies to reduce the effects of known sources of noise and preselect good collision events.

Therefore events with more than 10 tracks and a fraction of high-purity tracks larger than 25% are rejected. This reduces events where beam particles are traversing the pixel detector longitudinally leading to large occupancies and many fake tracks. Furthermore a well identified primary vertex is required in order to further reject noise events and identify good collision candidates. The selection is based on the number of degrees of freedom of the vertex (ndof > 4), the vertex z-coordinate ($|z| \leq 24$), and the radial distance of the vertex from the beam-pipe centre ρ ($\rho \leq 2$ cm).

Anomalous signals in the calorimeters are mostly due to particles hitting the transducers or striking the sensors and random discharges of the readout detector (HCAL). In the HF, scintillation and Cherenkov light affect the measurement of the photomultiplier tubes. Also punch-through particles exiting the back of the calorimeter can introduce additional $\not\!\!E_{\mathrm{T}}$ to the measurement in the HF. In the HB and HE electronic noise from the hybrid photo diode (HPD) and readout box (RBX) can affect the readout of one up to all 72 channels in a RBX. For most of the anomalous signals in the calorimeters a basic event cleaning is applied by default in the CMS reconstruction software (CMSSW) based on information about charge sharing between neighbouring channels, timing and pulse shape [49; 50]. The identified unphysical measurements in the ECAL or HCAL are thus excluded for reconstruction of higher level objects as jets or $\not\!\!E_{\mathrm{T}}$.

3.4 Particle Reconstruction and Identification

For a physics measurement the detector signals need to be translated into meaningful physics quantities. CMS uses a wide variety of reconstruction algorithms to calculate momentum four-vectors and other object specific variables from the measurements of the different CMS subsystems. To identify and distinguish the resulting physics objects, i.e. jets, muons, electrons and photons, different, analysis-specific identification criteria are used. In the following the key features of the reconstruction and the identification criteria of the objects used in the later analyses are summarised. The measurement of the $\not\!\!E_{\mathrm{T}}$ is described in more detail in Chapter 4.

3.4.1 Jets

Quarks and gluons produced in high-energy proton-proton collisions can not be observed directly, due to their colour charge and the resulting confinement. Instead quark-antiquark pairs are created, building a shower of new colour neutral particles (hadrons or mesons), called a jet. Thus jets are mainly reconstructed from the measurements in the ECAL and HCAL. But also the information from the inner tracker can be utilised to improve the reconstruction. Jets considered

here are clustered with the anti-k_{T} clustering algorithm [51] with a size parameter R =0.5. CMS uses three different jet reconstruction algorithms. Calorimeter jets (CaloJets) are reconstructed using only the energy deposits in the calorimeter towers. The jet-plus-track (JPT) algorithm utilises the transverse momentum of well measured tracks in the inner tracker and removes the corresponding, expected calorimeter deposits from the calculation [52]. The particle-flow (PF) jets are reconstructed by clustering four-momentum vectors of particle-flow candidates reconstructed by the particle-flow algorithm [53] utilising all detector components. The non-linearity of the response in the calorimeter for neutral and charged hadrons raises the need of jet energy corrections (JEC) to correct the jet, on average, back to hadron level [54]. Several levels of jet energy corrections are available including:

- **Offset (L1)**: These corrections are applied to subtract energy not associated with the high p_{T} scattering. CMS has developed three different methods to correct the offset introduced due to contributions from noise and pile up [54]. Here, the jet-area method ($L1Fast$) is applied, where for each event an average transverse momentum ρ is estimated per unit area. Depending on the jet area the jet is then corrected in dependence of ρ. For particle-flow jets charged hadrons not originating from the primary vertex can be identified and are in the following excluded from the jet reconstruction. Thus the identified charged hadrons are also excluded from the calculation of ρ in this case.

- **Relative jet corrections (L2)**: Before the application of JEC the response of the jets is dependent on the pseudorapidity. The level 2 corrections remove this dependency by correcting each jet relative to a jet in the central region of the detector.

- **Absolute jet corrections (L3)**: These corrections are designed to remove the p_{T} dependence of the jet response and correct the jet back to the hadron level.

- **Residual corrections**: Comparison between data and Monte Carlo simulation (MC) shows slight differences between the jet response in data and

MC. Therefore these, relatively small, additional corrections are applied on data only in dependence of η and p_{T} of the jets.

If not indicated otherwise, jets are corrected up to Level 3 in the following. For data the residual corrections are applied in addition. Offset corrections are only applied for results showing data recorded in 2011.

As a simple quality requirement loose jet identification (JetID) criteria are defined. For calorimeter jets the criteria are [55]:

- electromagnetic energy fraction (EMF) > 0.01,
- fraction of jet energy from the hottest (i.e. of highest energy) hybrid photo diode < 0.98,
- number of hits (i.e. cells) making up 90% of the jet's energy ($n90hits$) > 1.

The corresponding definition for particle-flow jets referring to the reconstructed charged or neutral hadrons and photons is [55]:

- number of constituents > 1,
- neutral hadron fraction < 0.99,
- neutral electromagnetic fraction < 0.99,
- charged hadron fraction > 0 if $|\eta| > 2.4$,
- charged multiplicity > 0 if $|\eta| > 2.4$,
- charged electromagnetic fraction < 0.99 if $|\eta| > 2.4$.

3.4.2 Photons

The excellent energy resolution and high granularity of the CMS ECAL allows a high precision measurement of isolated photons. Photon candidates are reconstructed from local deposits in the ECAL, which are summed up into superclusters.

The material in front of the calorimeter can cause conversion of photons and bremsstrahlung from electrons and positrons. This leads to a spread of the photon

decay remnants due to the strong magnetic field. Therefore, the reconstructed superclusters are extended in ϕ and corrected as a function of the ratio of the supercluster size in ϕ to the size in η. Additional corrections are applied to compensate for variations along η in the amount of tracker material, the E_{T} dependence of conversions and bremsstrahlung and the η dependence of lateral energy leakage. For simulated signal photons, the corrections are in the order of 1% of the uncorrected supercluster energy [56].

The reconstruction of the photon is based on the ratio of the energy deposited within a 3×3 array of ECAL crystals centred around the seed crystal of the supercluster to the total energy of the supercluster, called $r9$. The energy of the photon candidate is estimated depending on this quantity, which gives a measure if the photon is converted or not. For high values of $r9$, i.e. $r9 > 0.94(0.95)$ in the barrel (endcap), the energy of the 5×5 crystals around the crystal with the highest energy deposit is used as photon energy instead of the supercluster energy [56]. Besides this, the $r9$ variable is also used to avoid the reconstruction of photons (or electrons) from single noisy crystals.

Photons produced in decays of neutral hadrons in jets, e.g. π^0, tend to be less isolated and have a wider shower transverse profile. Thus further variables including isolation and shower shape variables are used to increase the purity of the photon identification. The applied identification criteria for photons include cuts on the following variables:

- **ECAL isolation** ($\mathrm{Iso}_{\mathrm{ECAL}}$): the sum of the ECAL energy in an annular region around the photon in $\eta - \phi$ plane with inner radius ΔR=0.06 and outer radius ΔR=0.3. A three crystal wide strip along ϕ is excluded.

- **HCAL isolation** ($\mathrm{Iso}_{\mathrm{HCAL}}$): the sum of the HCAL energy in an annular region around the photon $\eta - \phi$ plane with inner radius ΔR=0.15 and outer radius 0.3.

- **Tracker isolation** ($\mathrm{Iso}_{\mathrm{Track}}$): the scalar sum of the p_{T} of the tracks in a hollow cone around the photon with inner radius ΔR=0.04 and outer radius ΔR=0.3.

- **Combined isolation** ($\mathrm{Iso}_{\mathrm{comb}}$): the combined isolation is the sum of ECAL, HCAL and tracker isolation.

- **Hadronic energy fraction** ($\frac{Had}{Em}$): the ratio between the HCAL energy in an annular region around the photon with outer radius ΔR=0.15 and the ECAL supercluster energy.

- **Supercluster shape** $\sigma_{i\eta i\eta}$: $\eta - \eta$ element of the $\eta - \phi$ covariance matrix, which is a measure for the extent of the supercluster in η:

$$\sigma^2_{i\eta i\eta} = \frac{\Sigma_i^{5\times5} w_i (i\eta_i - i\eta_{seed})^2}{\Sigma_i^{5\times5} w_i}, \; w_i = max(0, 4.7 + \ln\frac{E_i}{E_{5\times5}}) \tag{3.6}$$

  i is an index within the 5×5 electromagnetic cluster, thus E_i and $i\eta_i$ are the energy and η index of the corresponding crystal, while $i\eta_{seed}$ is the η index of the seed crystal. $E_{5\times5}$ is the energy of the 5×5 crystals around the seed crystal.

- **Pixel seed veto**: To avoid the misidentification of electrons as photons, photons are required not to match any track reconstructed in the pixel detector that is consistent with the primary vertex.

The used selection criteria for isolated photons (γ) are summarised in Table 3.1. The criteria have been optimised using MC simulation for Standard Model processes and possible GGM signal. The resulting photon efficiency has been measured on data and the ratio of photon efficiencies between data and MC simulation was found to be [57]:

$$\frac{\epsilon_e^{data}}{\epsilon_e^{MC}} = 0.99 \pm 0.04. \tag{3.7}$$

The calorimeter isolation variables are strongly dependent on the number of pile up interactions in the event. To minimise the pile up dependence of the photon identification, the ECAL and HCAL isolations are corrected for this effect using again the average transverse momentum ρ per unit area. The average calorimeter isolations show a linear dependence on ρ and the obtained slope is used to calculate the pile up corrected isolations [57]:

$$\mathrm{Iso}_{\mathrm{ECAL}}^{\mathrm{Corr}} = \mathrm{Iso}_{\mathrm{ECAL}} - 0.1474 \cdot \rho \tag{3.8}$$

and

$$\mathrm{Iso}_{\mathrm{HCAL}}^{\mathrm{Corr}} = \mathrm{Iso}_{\mathrm{HCAL}} - 0.0467 \cdot \rho. \tag{3.9}$$

The pile up corrected combined isolation is then defined as

$$\mathrm{Iso}_{\mathrm{comb}}^{\mathrm{Corr}} = \mathrm{Iso}_{\mathrm{HCAL}}^{\mathrm{Corr}} + \mathrm{Iso}_{\mathrm{ECAL}}^{\mathrm{Corr}} + \mathrm{Iso}_{\mathrm{Track}}. \tag{3.10}$$

To identify jets with high electromagnetic energy deposits, i.e. due to π^0 hadrons occuring in the shower, a second object (γ_{Jet}) is defined by loosening the isolation cuts. It is defined such, that it is still similar to a photon in terms of resolution, while disjunctive from the tighter photon definition (γ). The γ_{Jet} will be used for a data driven estimate of Standard Model background in the presented search for supersymmetry. The main difference to the photon identification are looser isolation criteria as summarised in Table 3.1. To avoid overlap with the tight photons, the γ_{Jet} is required to fail either the photon isolation or the selection criteria on the shower shape variable $\sigma_{i\eta i\eta}$.

Table 3.1: Summary of photon and jet-photon fakeable object identification criteria.

Cut	γ	γ_{Jet}
Pixel Seed	no	no
$\mathrm{Iso}_{\mathrm{comb}}^{\mathrm{Corr}}$[GeV]	< 6	$< (min(30, 0.3 \cdot p_{\mathrm{T}}))$
$\sigma_{i\eta i\eta}$	< 0.011	< 0.014
$\frac{Had}{Em}$	< 0.05	< 0.05
$r9$	< 1	< 1
additional requirements	-	$\mathrm{Iso}_{\mathrm{comb}}^{\mathrm{Corr}} \geq 6$ GeV $\|\|$ $\sigma_{i\eta i\eta} \geq 0.011$

3.4.3 Electrons

Electrons are identified using similar criteria on isolation and shower shape as photons. The main difference is that electron candidates must match a charged particle track within $\Delta\eta$ and $\Delta\phi$, while they are still isolated from additional tracks. Furthermore, electrons are required to be within the fiducial region of the

calorimeter ($|\eta|$ <1.4442 or 1.5660< $|\eta|$ <2.5); additional selection criteria for the rejection of converted photons are not applied.

The electron requirements applied for the $\not\!\!E_{\mathrm{T}}$ studies presented in the next chapter are summarised in Table 3.2. These differ slightly from the electron definition used for the search for supersymmetry. In the latter an electron identification very similar to the described photon identification is used to estimate the background from electroweak processes. This electron object (γ_e) is required to pass all tight photon identification criteria, except for the pixel match veto requirement, which is inverted instead.

Table 3.2: Summary of electron identification criteria.

Cut	barrel	endcap
Pixel Seed	yes	yes
track match $\Delta\phi$	< 0.8	< 0.7
track match $\Delta\eta$	< 0.007	< 0.01
$\mathrm{Iso}_{\mathrm{ECAL}}$ [GeV]	$< 2 \cdot p_{\mathrm{T}}$	$< 0.06 \cdot p_{\mathrm{T}}$
$\mathrm{Iso}_{\mathrm{HCAL}}$ [GeV]	$< 0.12 \cdot p_{\mathrm{T}}$	$< 0.05 \cdot p_{\mathrm{T}}$
$\mathrm{Iso}_{\mathrm{Track}}$ [GeV]	$< 0.15 \cdot p_{\mathrm{T}}$	$< 0.15 \cdot p_{\mathrm{T}}$
$\sigma_{i\eta i\eta}$	< 0.011	< 0.003
$\frac{Had}{Em}$	< 0.05	< 0.07

Often the electron (or muon) energy deposits in the calorimeter are in a first step also reconstructed as jets. The jets used for the search for supersymmetry presented later, are cleaned from these jets. For this purpose another very loose electron selection is defined requiring electrons with a minimum transverse momentum of 15 GeV, $|\eta|$ <2.6 and a combined isolation smaller than $0.2 \cdot p_{\mathrm{T}}$.

3.4.4 Muons

Muon candidates are required to have a track in the inner tracker matching the track reconstructed in the muon system. The ECAL and HCAL isolation are required to be inconsistent with the expected energy deposit of the muon in the calorimeters and also the tracker isolation is expected to be small.

A loose muon selection is defined requiring muons with a minimum transverse momentum of 15 GeV, $|\eta|$ <2.6 and a combined isolation smaller than $0.2 \cdot p_{\mathrm{T}}$ is defined. This definition is used later, similar to the loose electron definition, to identify jets reconstructed from the muon energy deposits.

4

Measuring the Missing Transverse Energy

4.1 Reconstruction and Correction

Neutral weakly interacting particles leave a typical collider detector, like CMS, without any significant response in one of the detector components. The resulting imbalance in the total measured transverse momentum is the only way to deduce the presence of such a particle, which is important for both, Standard Model precision measurements and searches for new particles.

For the Standard Model, the only particle leaving the detector without detection is the neutrino, consequently $\not\!\!E_{\mathrm{T}}$ is an important observable for measurements of the decays of W bosons and top quarks, where it is used in the event reconstruction and to reject background events without neutrinos. Beyond the Standard Model, many theories predict final states with new weakly[1] interacting particles, e.g. the Gravitino in GMSB SUSY models as described in Sec. 2. Again, the $\not\!\!E_{\mathrm{T}}$ has large values in the events of interest and the observable is utilised to reject background events with smaller $\not\!\!E_{\mathrm{T}}$.

Technically, the $\not\!\!E_{\mathrm{T}}$ is defined as the negative vector sum over all reconstructed final state particles and hence is sensitive to mismeasurement of particle momen-

[1] 'weakly' denotes here particles leaving the detector without significant energy deposit, they take part in the weak interaction and/or the gravitation only.

tum caused by, e.g. detector malfunction and noise, particles hitting poorly instrumented regions of the detector, cosmic-rays, and beam halo particles.

During the data taking in 2009 and 2010 CMS commissioned three distinct algorithms for the reconstruction of $\not\!\!E_{\mathrm{T}}$ [58; 59] corresponding to the three available jet reconstruction algorithms. The 'Calo $\not\!\!E_{\mathrm{T}}$' algorithm uses only energy deposits in the calorimeters (ECAL, HCAL), where the direction of towers, relative to the centre of the detector, is used to define pseudo-particles. The track-corrected $\not\!\!E_{\mathrm{T}}$ (TC $\not\!\!E_{\mathrm{T}}$) extends the Calo $\not\!\!E_{\mathrm{T}}$ by including the transverse momentum of well measured tracks in the inner tracker and removing the corresponding, expected calorimeter deposits from the calculation [60]. The particle-flow $\not\!\!E_{\mathrm{T}}$ (PF $\not\!\!E_{\mathrm{T}}$) is calculated from the objects reconstructed by the particle-flow algorithm [53] utilising all detector components.

For Calo $\not\!\!E_{\mathrm{T}}$ the main source of underestimating the magnitude of $\not\!\!E_{\mathrm{T}}$ is the non-linearity of the response in the calorimeter for neutral and charged hadrons. In addition, charged particles are bent in the magnetic field, which leads to a displacement of the calorimetric energy deposits, especially for particles with low p_{T}. To remove the resulting bias on the $\not\!\!E_{\mathrm{T}}$ scale two correction steps are applied as described below in more detail.

Naturally, both effects are much smaller for the algorithms, which are not relying on the calorimeter information only. For PF $\not\!\!E_{\mathrm{T}}$ charged hadrons are reconstructed from tracks, and a correction factor is already applied intrinsically to the neutral hadron and photon energy leading to a reconstruction of the particles near to the correct energy scale. But due to, e.g. limited reconstruction efficiency of low energy tracks and calorimeter clusters, masked cells and cracks in calorimeters, limited muon acceptance in the forward region, nuclear interaction in the tracker and asymmetric photon conversions or electron bremsstrahlung in the tracker, the application of additional corrections to jets and $\not\!\!E_{\mathrm{T}}$ still improves the energy scale calibration of the particle-flow objects. Similarly also the TC $\not\!\!E_{\mathrm{T}}$ is expected to profit from additional corrections[1].

[1]However, the following studies focus on the other two algorithms, which are expected to differ most in their performance. The performance of TC $\not\!\!E_{\mathrm{T}}$ is expected to range between the other two algorithms.

A first step of corrections, referred to as 'type-I correction', utilises the jet energy corrections, which have been developed to correct the jets to the hadron level [61]. The difference between uncorrected and corrected jets is propagated to the $\not\!\!E_{\mathrm{T}}$ for all jets that have less than 0.9 of their energy in the ECAL[1] and a corrected transverse momentum $p_{\mathrm{T}} \geq$ 20 (10) GeV for Calo (PF) $\not\!\!E_{\mathrm{T}}$.

Since jet energy corrections are unreliable at low energies, only corrected jets above the mentioned thresholds are considered. This leads to a distortion of the type-I corrected MET at low energies, which can be reduced by applying a correction to the remaining 'unclustered' energy deposits not considered within the type-I corrections. This includes energy deposits not reconstructed in jets at all and jets below the type-I correction threshold, both are denoted by 'unclustered energy' in the next sections. The correction improves significantly the $\not\!\!E_{\mathrm{T}}$ energy scale and is called 'type-II correction'.

In the following a strategy to derive the type-II correction from $Z \to ee$ events is discussed and the resulting scale for PF and Calo $\not\!\!E_{\mathrm{T}}$ derived on $36 \pm 4\,\mathrm{pb}^{-1}$ of the 2010 data is presented (Sec. 4.2). The results from data are compared to the type-II correction scale obtained using the generator information of simulated events. The resulting scale and resolution for $\not\!\!E_{\mathrm{T}}$ after the different correction steps are shown in Sec. 4.3. In Sec. 4.3.1, $Z \to ee$ events are studied showing the improvement of scale and effects on resolution due to the type-II corrections. In addition the performance in dijet events after each correction step is presented in Sec. 4.3.2 for PF and Calo $\not\!\!E_{\mathrm{T}}$, probing the derived correction in another event topology. The presented studies are also documented in detail in [62; 63] and some of the results have been published here [59; 64]. In Sec. 4.4 several sources of instrumental mismeasurement, which can lead to additional contributions in the tail of the $\not\!\!E_{\mathrm{T}}$ distribution are discussed.

[1] With this selection criteria on the electromagnetic fraction of the jet, electrons and photons possibly reconstructed as jets are not corrected, but assumed to be already well calibrated.

4.2 Derivation of Type-II $\not\!\!E_{\mathrm{T}}$ Corrections

4.2.1 Event Selection for $Z \to ee$ events

For the derivation of the type-II corrections and for their validation $Z \to ee$ events from data are used. These events were recorded during the 2010 LHC run using the CMS two-level trigger system. The selection was based on the presence of at least one electron with transverse energy above a threshold of 15 or 17 GeV. To account for the different thresholds applied on trigger level the offline selection for electrons is requiring a transverse energy above 20 GeV such that the trigger efficiency for $Z \to ee$ events is estimated to be above 99%. In addition to the offline selection of electrons the identification criteria described in Sec. 3.4.3 are applied to all electrons[1]. To reject possible background at least two electrons with an invariant mass of the two leading electrons between 60 and 120 GeV are required.

The MC simulated events, shown for comparison, are usually scaled to a luminosity of 36 pb^{-1}, but in plots comparing data and simulation the number of simulated events is scaled directly to the data. Pile up is already included in the simulation, which is weighted such that the distribution of the number of primary vertices matches the corresponding distribution in data, i.e. 2.7 on average for the 2010 data.

4.2.2 Derivation of Type-II Scale

In the $Z \to ee$ event topology, the hadronic recoil u_T balances the transverse momentum of the Z boson as the events have basically no intrinsic $\not\!\!E_{\mathrm{T}}$. This balance between the $\vec{p}_{\mathrm{T}}$ of the Z boson ($\vec{q}_{\mathrm{T}}$) and the recoil can be utilised to get a measure for the correct scale of the unclustered energy, as the electrons and thus the $\vec{q}_{\mathrm{T}}$ are measured with high precision. In addition $Z \to ee$ events form an ideal sample for the derivation of the type-II corrections as the Z bosons are usually produced with low $\vec{q}_{\mathrm{T}}$ and the recoil is dominated by unclustered energy and soft

[1] For the particle-flow corrections the particle-flow electrons (and jets) are used. In this case the offline event selection is also done with particle-flow electrons, while the online trigger selection is always using the standard electrons.

jets. The 'unclustered energies', i.e. energy deposits not reconstructed in jets and jets below the type-I correction threshold, are combined to a single object called $\vec{U}_{\mathrm{T}}$. The kinematic definitions of the described $Z \to ee$ event topology are illustrated in Fig. 4.1. For the derivation of the type-II scale, only events without any jet above the type-I threshold are used to minimise the influence of the jet energy scale (JES)[1].

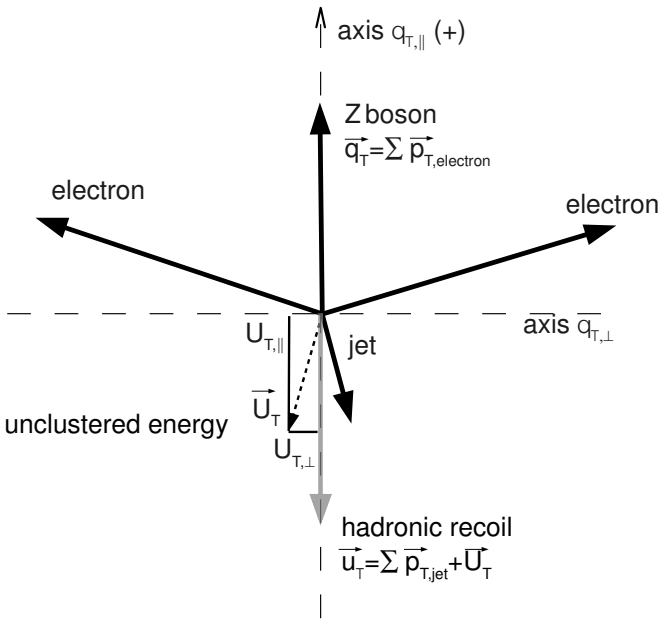

Figure 4.1: Kinematic definitions for $Z \to ee$ events.

$\vec{U}_{\mathrm{T}}$ is split into components parallel and perpendicular to $\vec{q}_{\mathrm{T}}$ to separate effects from other components, such as noise, underlying event, etc. from the measurement of the unclustered energy. The projection along the $q_{\mathrm{T},\|}$ axis ($U_{\mathrm{T},\|}$) is chosen for the derivation of the correction, because the range of the energy spectrum of the unclustered energy over all events along this axis is larger compared to, e.g. the orthogonal axis, where on average no unclustered energy is expected.

[1] In Sec. 4.3.1 the whole sample, including events with jets, is used for the validation of the corrections.

In general the $\not\!\!E_{\mathrm{T}}$ can be divided into individual contributions from jets, isolated muons, isolated electrons and photons, and unclustered energies. Isolated muons, electrons and photons are expected to require no scale correction, since their energy is measured with high resolution. The contribution due to the unclustered energy is the difference between the reconstructed $\not\!\!E_{\mathrm{T}}$ and the sum of the other contributions. As described above unclustered energies are handled as a single object $\vec{U}_{\mathrm{T}}$ and thus, for $Z \to ee$ events, it can be defined as:

$$\vec{U}_{\mathrm{T}} = -\vec{\not\!\!E}_{\mathrm{T}_{uncorr}} - \sum \vec{p}_{\mathrm{T},jet,uncorr} - \sum \vec{p}_{\mathrm{T}electron}, \tag{4.1}$$

where $\vec{p}_{\mathrm{T},jet,uncorr}$ is the momentum of an uncorrected jet with a corrected $p_{\mathrm{T}} \geq 20$ (10) GeV for Calo (PF) $\not\!\!E_{\mathrm{T}}$ and less than 0.9 of their energy in the ECAL. For PF $\not\!\!E_{\mathrm{T}}$ the type-II scale has been derived for several jet energy thresholds. A jet threshold of 10 GeV shows the best performance for the type-I corrections with respect to resulting scale and resolution and is therefore used in the following [59]. The distribution of q_{T} and U_{T} is shown in Fig. 4.2 for Calo $\not\!\!E_{\mathrm{T}}$ and in Fig. 4.3 for PF $\not\!\!E_{\mathrm{T}}$[1].

The mean of the parallel component of the measured unclustered energy projected to q_{T} is shown in Fig. 4.4(a) in dependence of q_{T} for Calo $\not\!\!E_{\mathrm{T}}$ and in Fig. 4.5(a) for PF $\not\!\!E_{\mathrm{T}}$. The mean and its uncertainty have been obtained by fitting a Gauss function[2] to the $U_{\mathrm{T},\parallel}$ in each q_{T} bin. Exemplary distributions and the results from the fit in individual q_{T} bins are shown in App. A.3.1. Large error bars are due to low statistics in the corresponding distribution, or, in individual bins, due to a failure of the fitting algorithm[3].

The relative response of the unclustered energy in each event is defined as

$$R = \frac{q_{\mathrm{T}} - U_{\mathrm{T},\parallel}}{q_{\mathrm{T}}}. \tag{4.2}$$

[1] As the applied jet threshold is smaller for PF $\not\!\!E_{\mathrm{T}}$ than for Calo $\not\!\!E_{\mathrm{T}}$, the total number of events passing the selection is smaller in this case.

[2] The fit has been performed in the $\pm 2\ \sigma$ range around the mean of the histogram.

[3] Also, in some high q_{T} bins, the number of events is very low, leading to an underestimation of the corresponding uncertainty on the mean. However, the effect on the resulting type-II scale is negligible as the result is dominated by the lower q_{T} region.

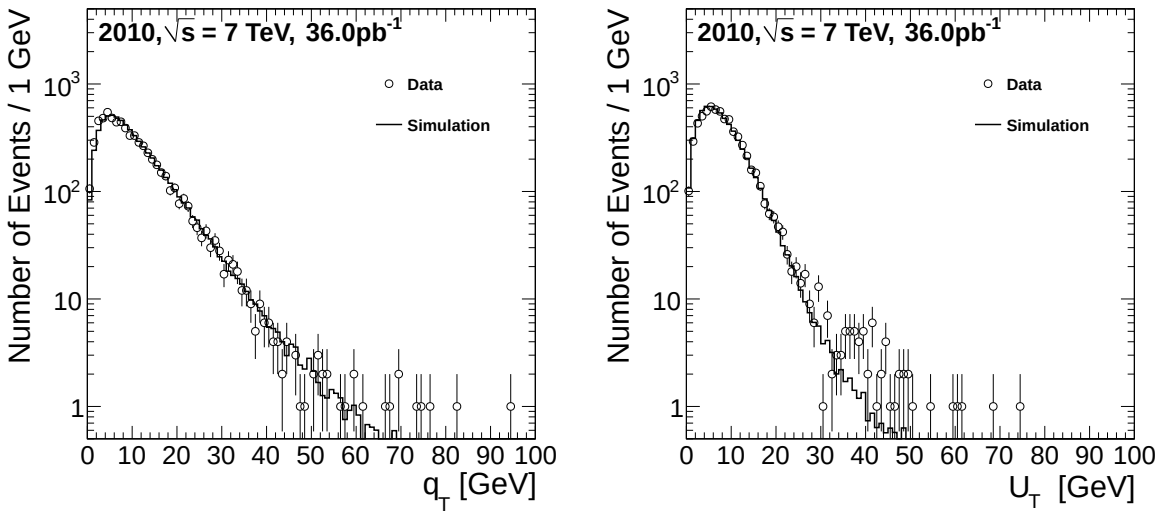

(a) (b)

Figure 4.2: Calo $\not\!\!E_{\mathrm{T}}$: Distribution of (a) q_{T} and (b) U_{T} in the selected $Z \to ee$ sample without jets.

R is measured in the same bins of q_{T} as the average parallel component $< U_{\mathrm{T},\parallel} >$. The mean of the relative response in each bin, $< R >$, is shown in Fig. 4.4(b) for Calo $\not\!\!E_{\mathrm{T}}$ and in Fig. 4.5(b) for PF $\not\!\!E_{\mathrm{T}}$. The mean and uncertainty are again obtained by fitting a Gauss function in each q_{T} bin as described above for the $U_{\mathrm{T},\parallel}$ distribution. Exemplary distributions and the results from the fit in individual q_{T} bins are also shown in App. A.3.1.

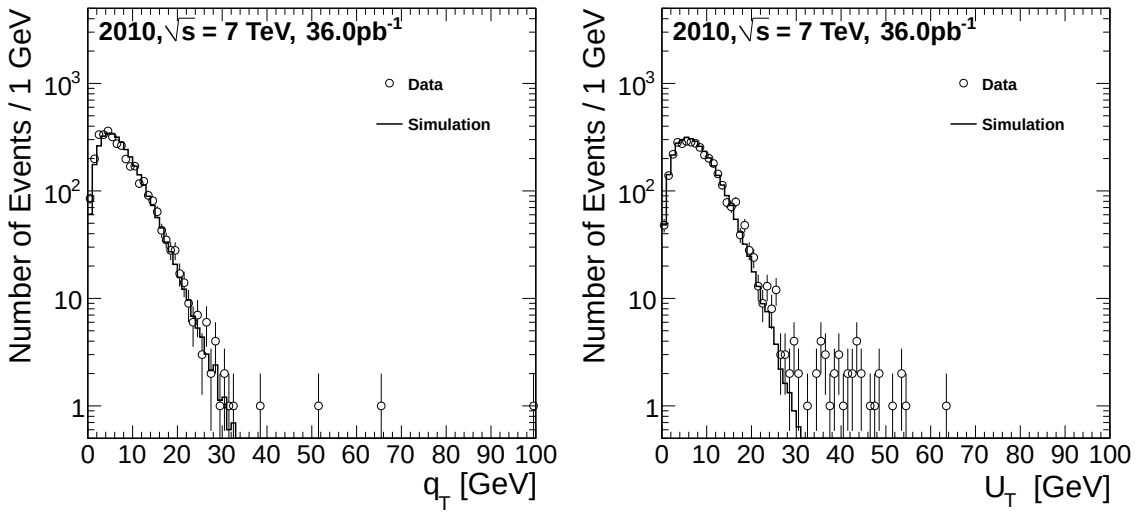

(a) (b)

Figure 4.3: PF $\not\!\!E_{\mathrm{T}}$: Distribution of (a) q_{T} and (b) U_{T} in the selected $Z \to ee$ sample without jets.

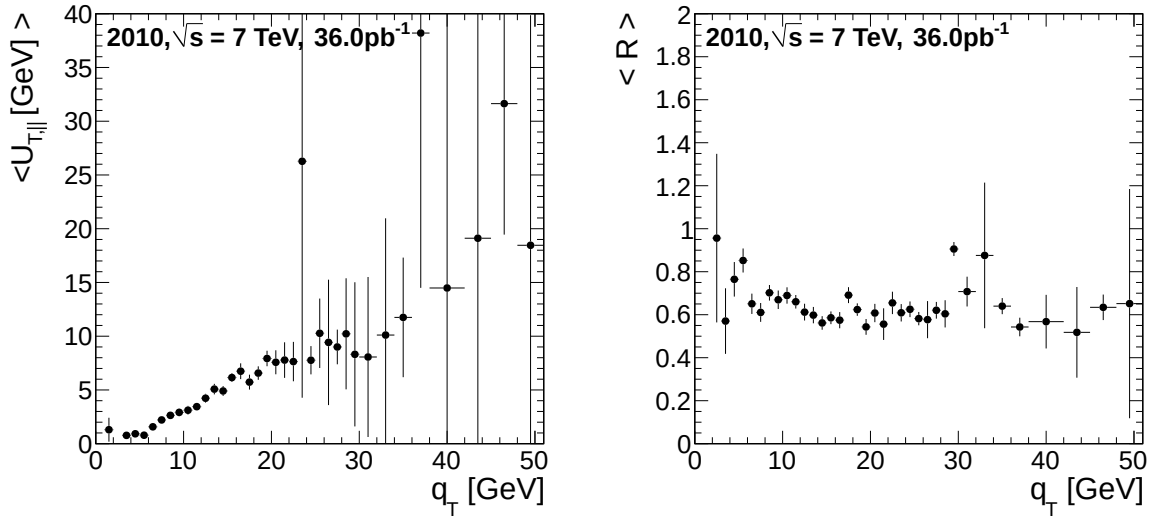

(a) (b)

Figure 4.4: Calo $\not\!\!E_{\mathrm{T}}$:(a) Average parallel projection of U_{T} and (b) average relative response R of unclustered energy in bins of q_{T}.

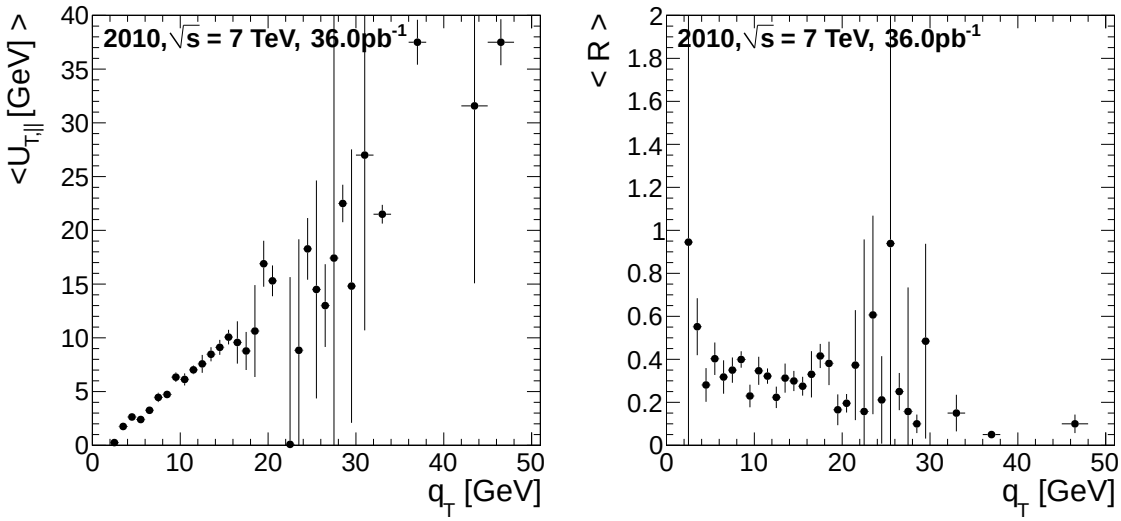

(a) (b)

Figure 4.5: PF $\not\!\!E_{\mathrm{T}}$: (a) Average parallel projection of U_{T} and (b) average relative response R of unclustered energy in bins of q_{T}.

Ideally the resulting correction should be applicable to different event topologies. Therefore it should not be obtained directly from the relative response measured in dependence of q_T. Instead the correction is derived in bins of $< U_{T,\parallel} >$ utilising both plots from Fig. 4.4 (4.5 for PF $\not\!\!E_T$). These figures have the same binning, and, in order to account for the lower number of entries at high q_T, the bin size is increased for larger values of q_T. In each bin of q_T the average $U_{T,\parallel}$ is measured and the resulting correction factor U_{Scale} is calculated as

$$U_{Scale}(< U_{T,\parallel} >) =< \frac{1}{|R-1|} > \tag{4.3}$$

The resulting correction factor for unclustered energy is shown in Fig. 4.6 for Calo $\not\!\!E_T$ and PF $\not\!\!E_T$.

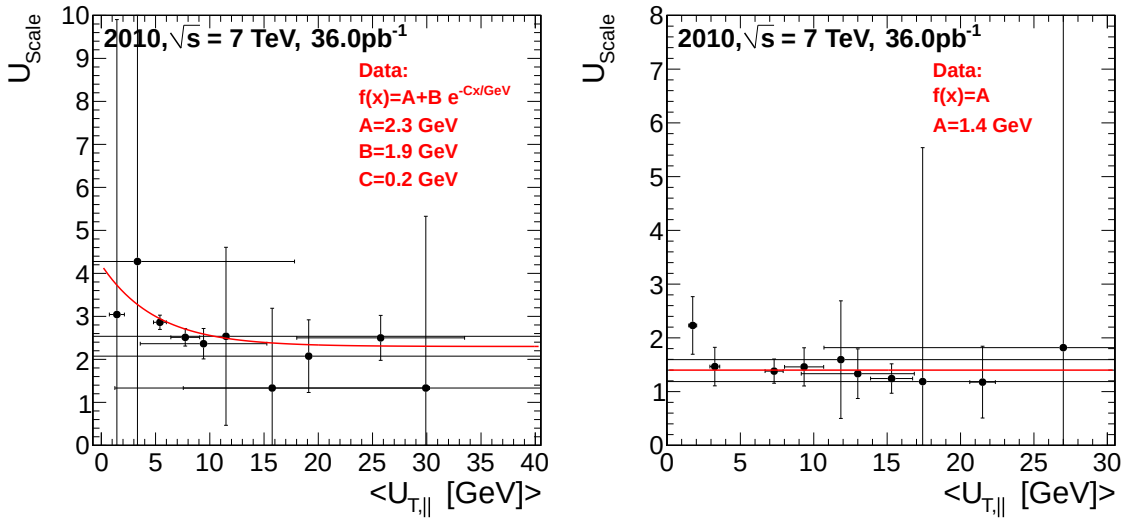

(a) Calo $\not\!\!E_T$ (b) PF $\not\!\!E_T$

Figure 4.6: Resulting correction factor derived on data level in dependence of average $U_{T,\parallel}$ for (a) Calo $\not\!\!E_T$ and (b) PF $\not\!\!E_T$.

The statistical uncertainty of the mean of $U_{T,\parallel}$ in each q_T bin translates into a horizontal uncertainty in Fig. 4.6. Due to the small size of the 2010 dataset some uncertainties are very large and it is difficult to determine a functional form of the correction from data only. But, as a validation, the method has been applied on MC simulation as well and the resulting correction factors are shown

in Fig. 4.7. For ease of comparison the correction factors obtained from data are shown again in the same figure. However, points with a very large uncertainty are not displayed to improve the readability. For the fitted correction function all points, as shown in Fig. 4.6 were used.

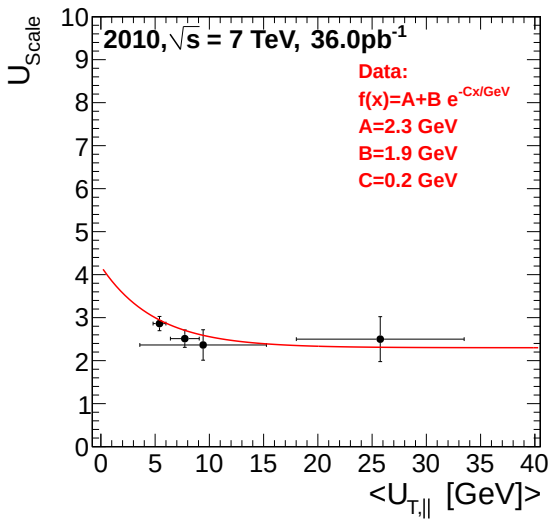

(a) Calo $\not\!\!E_{\mathrm{T}}$

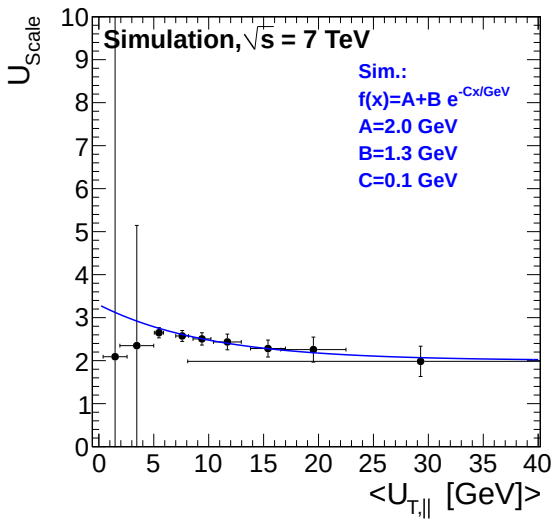

(b) Calo $\not\!\!E_{\mathrm{T}}$

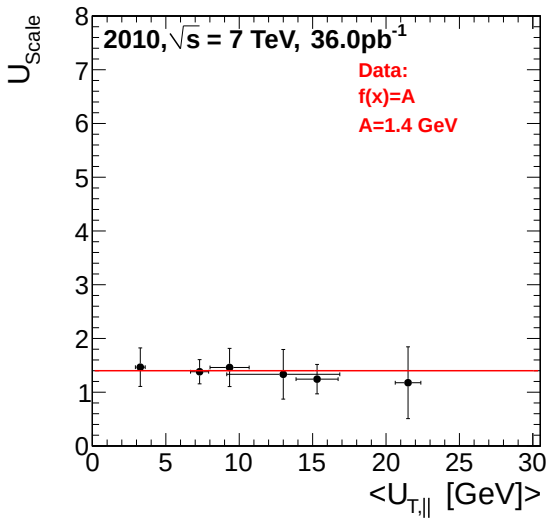

(c) PF $\not\!\!E_{\mathrm{T}}$

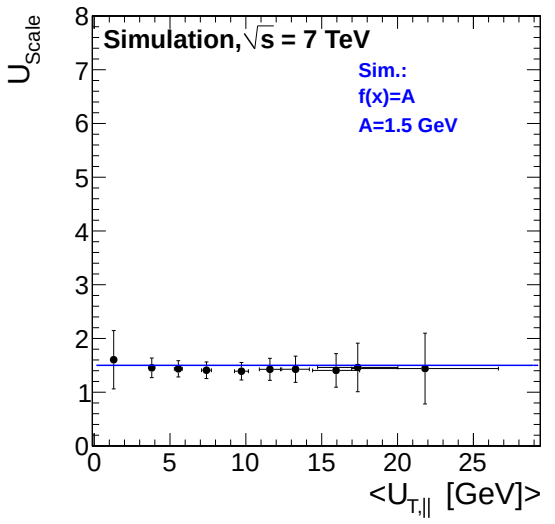

(d) PF $\not\!\!E_{\mathrm{T}}$

Figure 4.7: Resulting correction factor derived on data level from (left column) data and (right column) simulation in dependence of average $U_{\mathrm{T},\parallel}$. Data points with large uncertainties are removed to improve the readability of the plot. For the fit of the correction function all points, as shown in Fig. 4.6 are used.

For Calo $\not\!\!E_{\mathrm{T}}$, a function of the form

$$A + B \cdot e^{-C \cdot x/GeV} \tag{4.4}$$

is found to describe the distribution in simulation, where x is $< U_{\mathrm{T},\parallel} >$. The resulting parameters and their uncertainties from the fit are

$$A = 2.0 \pm 0.7,\ B = 1.3 \pm 0.5 \text{ and } C = 0.1 \pm 0.1.$$

Fitting the same function on the data yields

$$A = 2.3 \pm 0.4,\ B = 1.9 \pm 1 \text{ and } C = 0.2 \pm 0.2,$$

which is, within the statistical uncertainties, in good agreement with the results obtained from simulation.

As expected the derived scale for PF $\not\!\!E_{\mathrm{T}}$ is smaller than for Calo $\not\!\!E_{\mathrm{T}}$. Furthermore, the energy dependence of the scale factor is smaller. Therefore, a single scale factor is derived by fitting a constant A to the distribution of U_{Scale}. The resulting correction factor for particle-flow is

$$A = 1.4 \pm 0.2$$

for data and

$$A = 1.5 \pm 0.1$$

for simulation. As for Calo $\not\!\!E_{\mathrm{T}}$ the value measured from data agrees well with the expectation from simulation, which underlines the high quality of simulation and the good understanding of the CMS detector.

For both algorithms another approach using only simulation has been tested, which uses the generator information as estimator for the unclustered energy instead of q_{T} [63]. Again, the resulting correction scale was found to be in good agreement with the results measured on data level.

As the measured direction of $\vec{U}_{\mathrm{T}}$ is affected by noise and underlying event, it is expected that the average value of U_{T} is higher than the average $U_{\mathrm{T},\parallel}$. As $U_{\mathrm{T},\parallel}$ is only accessible in some event topologies similar to $Z \to ee$, the type-II correction in general is calculated by multiplying directly the U_{T} with the correction factor $U_{Scale}(U_{\mathrm{T},\parallel})$.

4.2.3 Systematic Uncertainties

The main systematic uncertainty for the data driven derivation of the type-II scale is currently the size of the used data sample resulting in large uncertainties of the fitted parameters. This uncertainty has been propagated to the $\not\!\!E_{\mathrm{T}}$ for the validation of dijet events and will be discussed in Sec. 4.3.2.

Another systematic uncertainty arises from the different jet flavour composition of the $Z \to ee$ sample on which the type-II correction is estimated, compared to other samples like for instance photon-jet. While in the photon-jet sample the leading jet is very likely a quark jet (90%), the jet-flavour composition of the leading jet in the $Z \to ee$ events is about 60% quarks and 40% gluons at transverse momenta of 20 GeV as shown in Fig. 4.8. If the unclustered energy is dominated by jets just below the threshold of 20 GeV, the derived $Z \to ee$ correction factor overcorrects if applied on a quark-jet dominated sample, because of the different flavour-dependent jet-response, i.e. $\sim$ 10% at a jet momentum of 20 GeV[54]. For a pure gluon-jet sample the derived correction will instead be too small by at most 6%. Therefore the systematic uncertainty due to jet flavour composition is estimated to be smaller than 6% for Calo $\not\!\!E_{\mathrm{T}}$.

For particle-flow jets the flavour-dependence of the jet-response is smaller than for calorimeter only jets, i.e $\sim$ 3% at a jet momentum of 10 GeV[54]. At transverse momenta below 10 GeV the $Z \to ee$ events contain about 50% quarks and 50% gluons leading to a maximal uncertainty due to jet flavour composition for PF $\not\!\!E_{\mathrm{T}}$ in the order of 1.5%.

In addition, systematic uncertainties can arise from out-of-cone showering of jets, that are already intrinsically considered in the corrected jet energy and thus in the type-I MET corrections, and can be double-counted as unclustered energy. Another source of systematic uncertainty is the application of the correction directly to the measured direction of U_{T} instead of $U_{\mathrm{T},\parallel}$. As explained before U_{T} is expected to be larger due to noise and underlying event and therefore leads to a small systematic overcorrection of the unclustered energy. The average difference between the U_{T} and $U_{\mathrm{T},\parallel}$ was measured from $Z \to ee$ data as $\sim$4 GeV. The resulting effect on the $\not\!\!E_{\mathrm{T}}$ scale was found to be small compared to the effects from jet energy corrections.

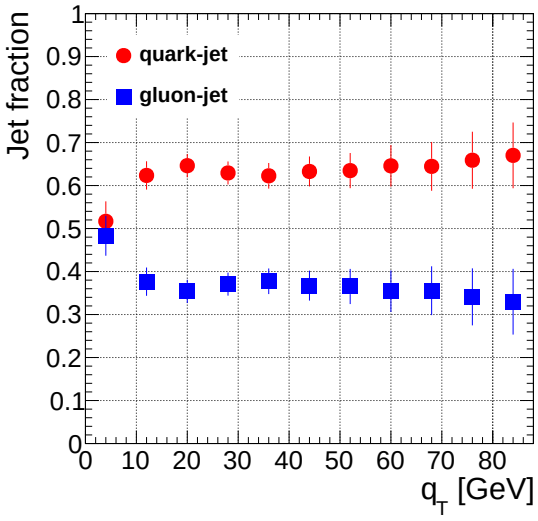

Figure 4.8: MC prediction (PYTHIA [65]) for quark and gluon fraction of leading jets in $Z \to ee$ events.

4.3 Scale and Resolution

For the following measurement of the $\not\!\!E_{\mathrm{T}}$ scale and resolution the data is corrected with the type-II scale obtained from data, while the type-II scale obtained from simulation is used for simulation. The performance of the corrections is studied by applying them to $Z \to ee$ and dijet events comparing the resulting data and MC distributions. To validate the scale of $\not\!\!E_{\mathrm{T}}$ after the application of type-I and type-II corrections, the parallel and perpendicular components of $\not\!\!E_{\mathrm{T}}$ to different axes defined for each event topology are studied. For $Z \to ee$ events the hadronic recoil is calculated and studied in addition to $\not\!\!E_{\mathrm{T}}$.

4.3.1 $Z \to ee$ Events

To validate the derived type-II scale, the $\not\!\!E_{\mathrm{T}}$ parallel and perpendicular projections to the direction of the reconstructed Z boson are studied after the application of the type-I and the type-II corrections. Furthermore, the scale of the $\not\!\!E_{\mathrm{T}}$ is validated looking at the ratio between the hadronic recoil u_{T} and the $\not\!\!E_{\mathrm{T}}$ in dependence of the reconstructed Z boson p_{T} (q_{T}). Again the hadronic recoil is also projected to the axis parallel to the Z direction ($u_{\parallel}$). In the following,

these distributions are shown for both studied $\not\!\!E_T$ algorithms: calorimeter only and particle-flow.

4.3.1.1 Performance in Events without Jets

As discussed before, the type-II corrections are derived from a sample without jets above the type-I threshold to minimise the dependence on the JES. As a first closure test for the correction the $\not\!\!E_T$ scale and resolution is measured in the same event sample. The resulting parallel and perpendicular projections of the $\not\!\!E_T$ against q_T are shown in Fig. 4.9 for PF $\not\!\!E_T$ and in Fig. 4.10 for Calo $\not\!\!E_T$.

As only events without jets used for the type-I correction are selected the results for uncorrected and type-I corrected $\not\!\!E_T$ are identical by construction. Thus the type-I corrected $\not\!\!E_T$ is not shown in the corresponding figures. The expected adjustment of the $\not\!\!E_T$ scale after the application of the type-II correction is visible over the whole range of q_T. As expected, the perpendicular component of $\not\!\!E_T$ is small and no significant shift is introduced by the correction. The results from data and simulation agree within the statistical uncertainties.

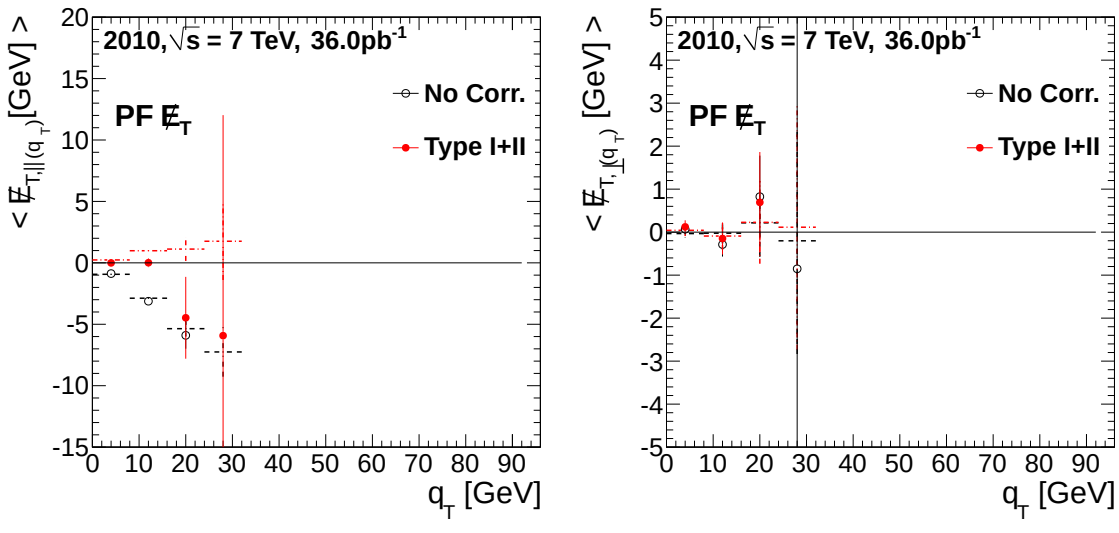

(a) (b)

Figure 4.9: PF $\not\!\!E_T$ (no jets): Uncorrected and type-II corrected $\not\!\!E_T$ (a) parallel and (b) perpendicular to Z direction in dependence of q_T compared with Monte Carlo simulation (dashed lines).

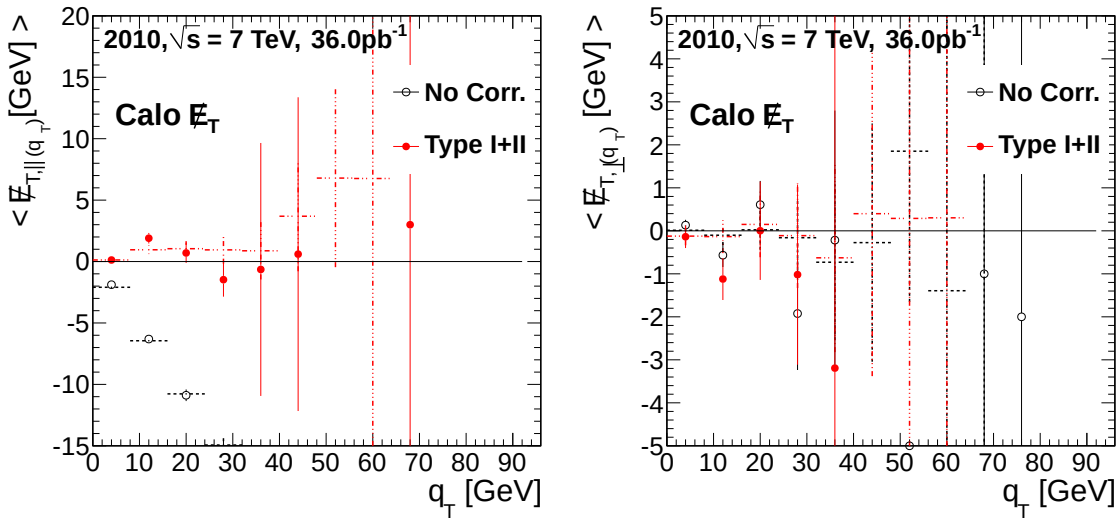

(a) (b)

Figure 4.10: Calo $\not\!\!E_T$ (no jets): Uncorrected and type-II corrected $\not\!\!E_T$ (a) parallel and (b) perpendicular to Z direction in dependence of q_T compared with Monte Carlo simulation (dashed lines).

4.3.1.2 Performance in Inclusive Events

The performance of uncorrected, type-I and type-II corrected $\not\!\!E_T$ in all selected $Z \to ee$ events, including events with jets, is shown in Fig. 4.11 for PF $\not\!\!E_T$ and Fig. 4.12 for Calo $\not\!\!E_T$.

For both algorithms the extension to the whole $Z \to ee$ dataset shows an overcorrection of the $\not\!\!E_T$ scale in events with jets. This is expected due to the jet energy scale (JES) dependence on the flavour composition of the jets. The JES is derived using QCD dijet events which have a different quark-gluon mixture than $Z \to ee$ events leading to an overcorrection of the jets and too large type-I corrections and thus leading to the overcorrection of $\not\!\!E_T$ scale visible in the inclusive $Z \to ee$ events. It is expected, that additional flavour corrections [66] will reduce this effect.

To study the size of the overcorrection due to the flavour dependencies of the JES, the vector sum of the difference between the transverse momenta of corrected jets ($\vec{p_T}_{j,corr}$) and corresponding jets on generator level ($\vec{p_T}_{j,gen}$) has

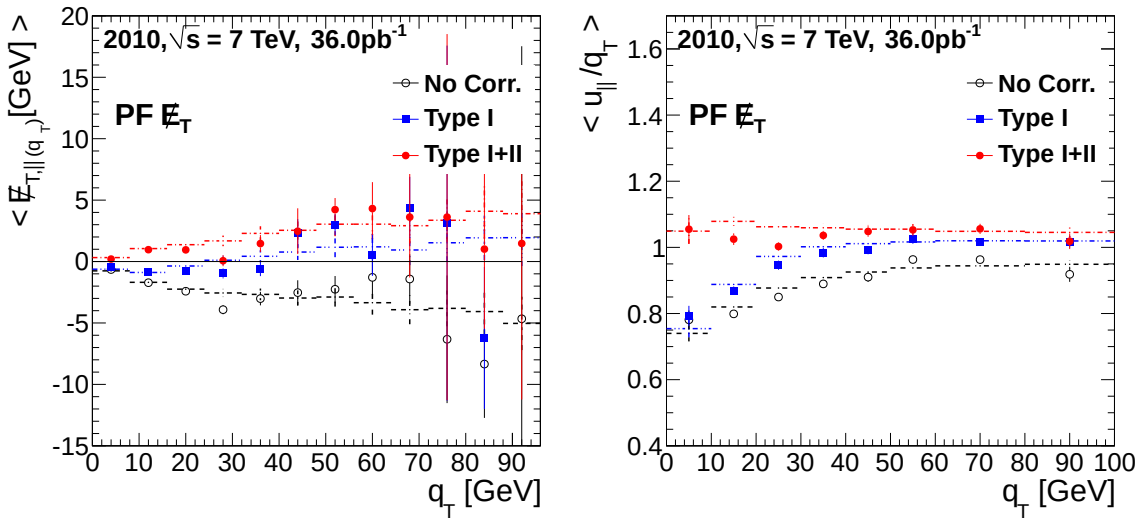

(a) (b)

Figure 4.11: PF $\not\!\!E_{\mathrm{T}}$ (inclusive jets): (a) $\not\!\!E_{\mathrm{T}}$ parallel to Z direction and (b) ratio of hadronic recoil projected to Z direction ($u_{\parallel}$) and q_{T} in dependence of q_{T}. Monte Carlo simulation is shown for comparison (dashed lines).

been computed for each event in the simulated sample:

$$\vec{\Delta}_{jet} = \sum (\vec{p_{\mathrm{T}}}_{j,corr} - \vec{p_{\mathrm{T}}}_{j,gen}). \tag{4.5}$$

The average of the magnitude of this vector, $< \Delta_{jet} >$, is measured in dependence of q_{T} showing the size of the resulting offset of the $\not\!\!E_{\mathrm{T}}$ scale due to the flavour dependence of the jet energy corrections (Fig. 4.13(a)). The size of this offset corresponds well to the offset visible in Fig. 4.11(a). For further crosscheck the resulting offset is subtracted from the hadronic recoil in each event

$$(\frac{u_{\parallel}}{q_{\mathrm{T}}})_{\Delta_{jet}} = \frac{u_{\parallel} - \Delta_{jet}}{q_{\mathrm{T}}},$$

leading to a validation of the type-II $\not\!\!E_{\mathrm{T}}$ scale in inclusive events assuming perfect jet energy correction of the reconstructed jets. The resulting $\not\!\!E_{\mathrm{T}}$ scale is visible in Fig. 4.13(b) showing $(\frac{u_{\parallel}}{q_{\mathrm{T}}})_{\Delta_{jet}}$ in dependence of q_{T}[1]. The overcorrection is completely removed and a slight under-correction of $\not\!\!E_{\mathrm{T}}$ scale after type-II corrections

[1] Fig. 4.13 shows the described influence of jet energy corrections for PF $\not\!\!E_{\mathrm{T}}$, the corresponding results for Calo $\not\!\!E_{\mathrm{T}}$ show similar results and are attached in A.3.2.

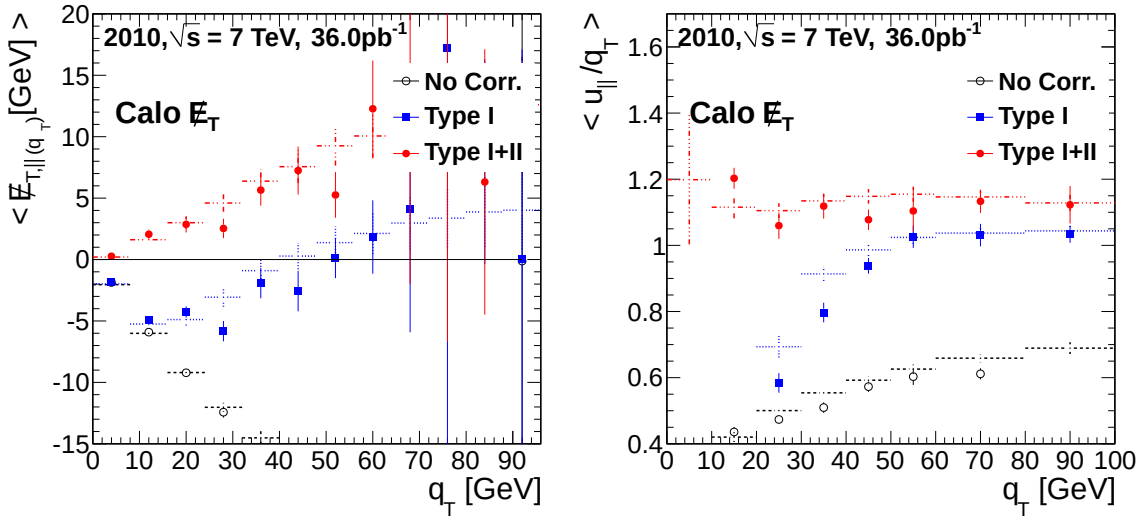

Figure 4.12: Calo $\not\!\!E_{\mathrm{T}}$ (inclusive jets): (a) $\not\!\!E_{\mathrm{T}}$ parallel to Z direction and (b) ratio of hadronic recoil projected to Z direction ($u_{\parallel}$) and q_{T} in dependence of q_{T}. Monte Carlo simulation is shown for comparison (dashed lines).

emerges. By deriving the correction from inclusive events, the type-II corrected $\not\!\!E_{\mathrm{T}}$ could be adjusted further for this effect. However, within the uncertainties due to the JES corrections the type-I and type-II corrections show a good performance and the improvement of the $\not\!\!E_{\mathrm{T}}$ scale after application of the derived type-II corrections is visible, especially for low q_{T}.

The type-I and type-II corrections lead to an upscaling of the $\not\!\!E_{\mathrm{T}}$ and, therefore, to an expected widening of the $\not\!\!E_{\mathrm{T}}$ distribution. Due to this expected and necessary upscaling, the $\not\!\!E_{\mathrm{T}}$ scale is adjusted, but it is difficult to compare the performance of the different correction steps with respect to the resolutions directly. To account for the different scales the $\not\!\!E_{\mathrm{T}}$ response in dependence of q_{T} as shown before (e.g. Fig. 4.11(b)) is used. The scale corrected response is then defined as the width of the $\not\!\!E_{\mathrm{T}}$ distribution divided by the $\not\!\!E_{\mathrm{T}}$ response and allows the comparison between different algorithms and correction steps.

The correction of the unclustered energy tends to improve the resolution of the $\not\!\!E_{\mathrm{T}}$ and recoil distributions. However, noise and energy deposits from pile up are

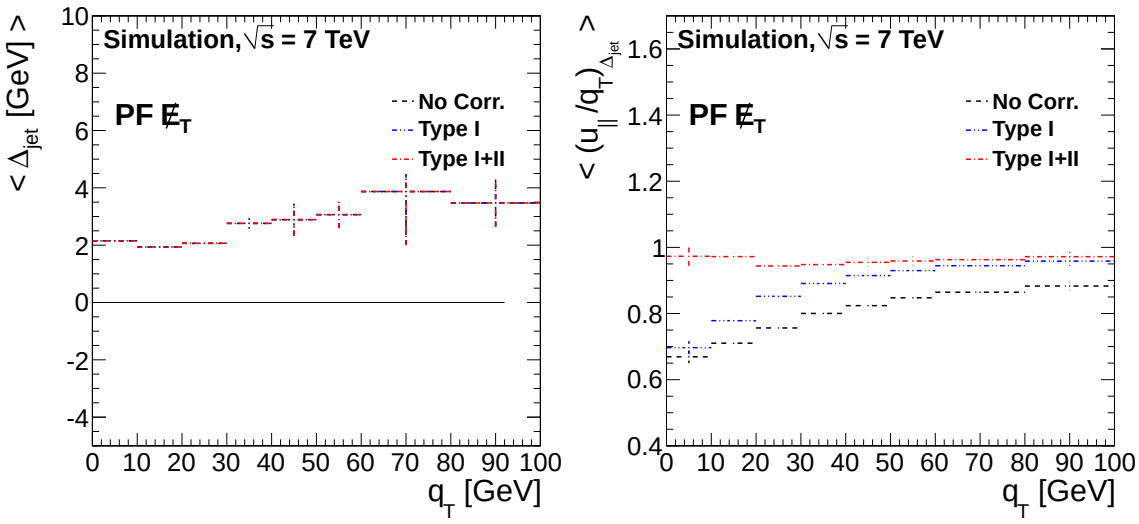

(a) (b)

Figure 4.13: PF $\not\!\!E_T$ (inclusive jets, simulation only): (a) $< \Delta_{jet} >$ and (b) $(\frac{u_{\parallel}}{q_T})_{\Delta_{jet}}$ in dependence of q_T.

scaled up too, and this unavoidable effect is working against the improvement of resolution. For PF $\not\!\!E_T$, where the overall amount of unclustered energy is relatively small, the effects due to noise and pile up become more important and the type-II correction, depending on the cleanliness of the event, slightly worsens the resolution. This is especially true for events with pile up and the perpendicular component of the recoil with respect to the Z boson direction, as it contains only a small amount of unclustered energy. The resolution of type-I and type-II corrected $\not\!\!E_T$ is shown for the parallel and the perpendicular components in events with and without pile up in Fig. 4.14 for Calo $\not\!\!E_T$ and in Fig. 4.15 for PF $\not\!\!E_T$. For ease of comparison all distributions are normalised to the uncorrected $\not\!\!E_T$.

All in all the type-II correction improves significantly the scale of the $\not\!\!E_T$ in $Z \to ee$ events for both $\not\!\!E_T$ algorithms, while the effect on the resolution is more subtle and depends strongly on the $\not\!\!E_T$ algorithm and event selection.

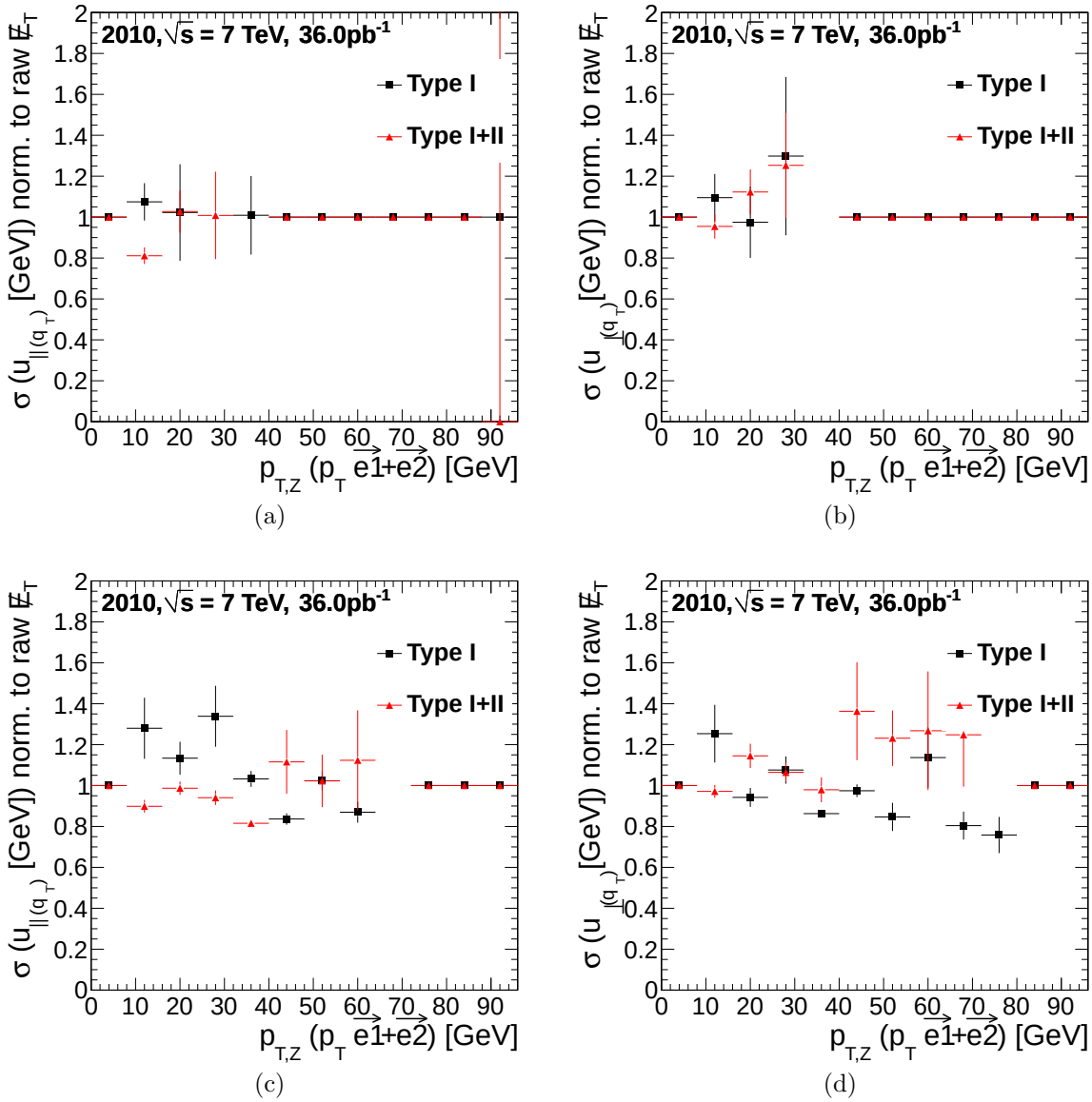

Figure 4.14: Calo $\not\!\!E_{\mathrm{T}}$ (inclusive jets, data only): Scale corrected resolution for (a), (c) parallel and (b), (d) perpendicular component of the recoil in dependence of q_{T} for events with (upper row) 1 and (lower row) > 1 reconstructed primary vertices.

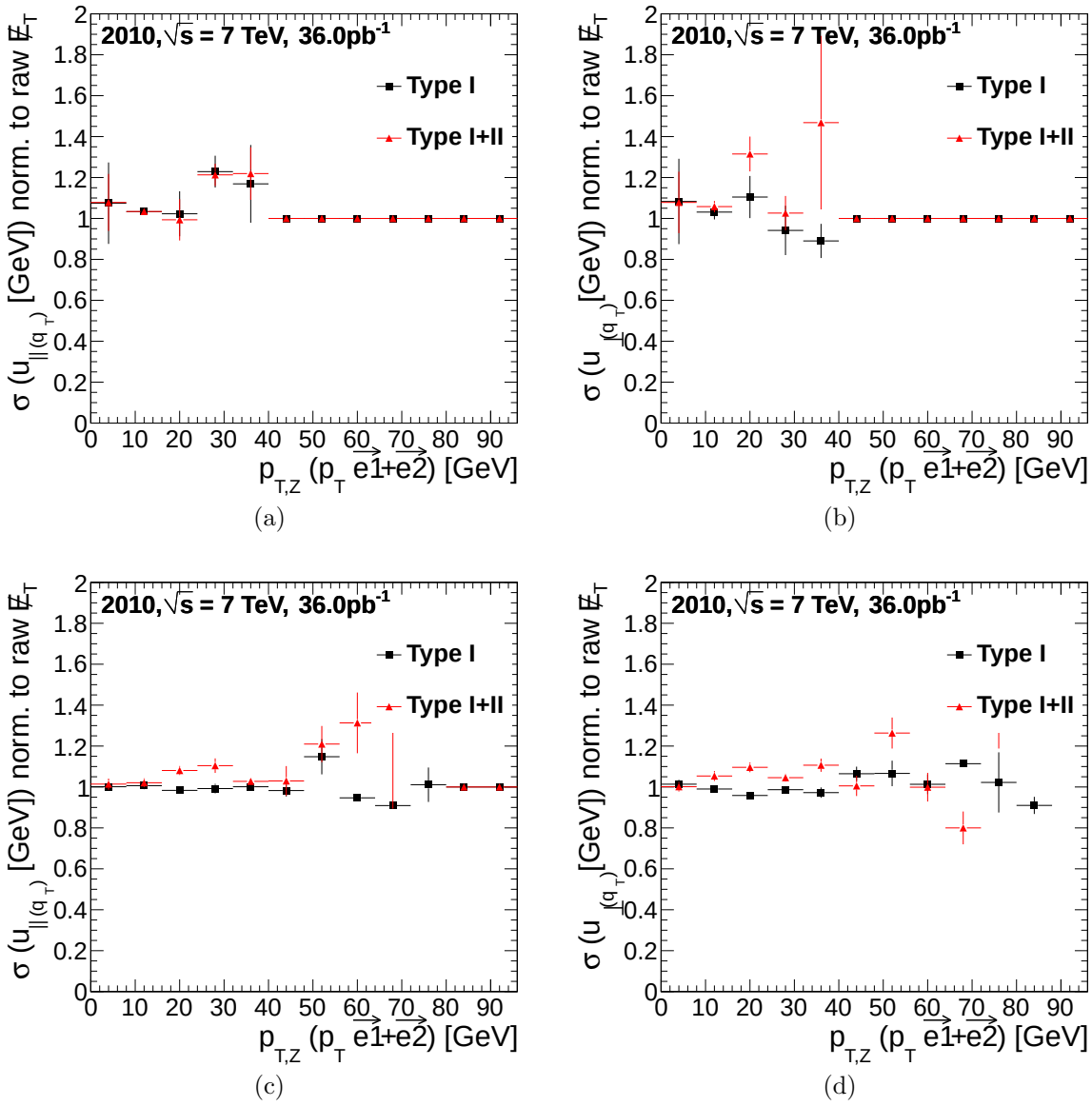

Figure 4.15: PF $\not\!\!E_{\mathrm{T}}$ (inclusive jets, data only): Scale corrected resolution for (a), (c) parallel and (b), (d) perpendicular component of the recoil in dependence of q_{T} for events with (upper row) 1 and (lower row) > 1 reconstructed primary vertices.

4.3.2 Minimum Bias and Dijet Events

A less biased way to study the $\not\!\!E_{\mathrm{T}}$ performance is to look at events with no jet selection criteria applied, so called minimum bias events. The corresponding $\not\!\!E_{\mathrm{T}}$ distributions for uncorrected, type-I and type-II corrected $\not\!\!E_{\mathrm{T}}$ are shown in Fig. 4.16. The distortion introduced by the type-I correction at the jet threshold and smoothened by the type-II correction is very clearly visible in these events.

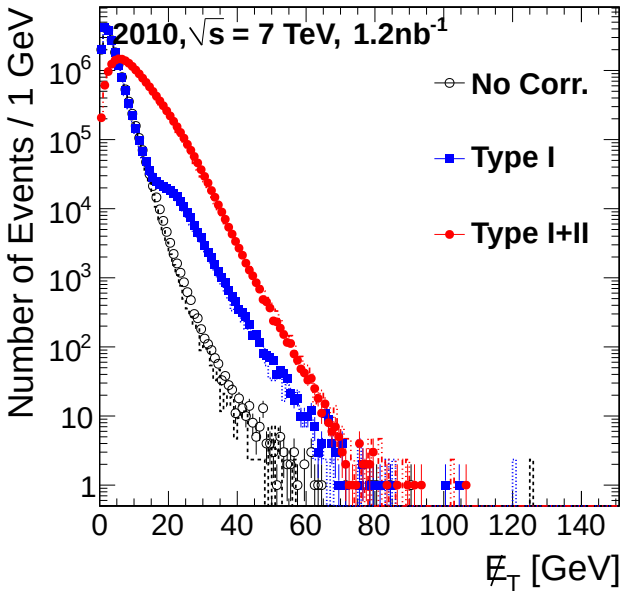

Figure 4.16: Calo $\not\!\!E_{\mathrm{T}}$: $\not\!\!E_{\mathrm{T}}$ uncorrected, type-I and type-II corrected $\not\!\!E_{\mathrm{T}}$ in minimum-bias events compared with Monte Carlo simulation (dashed lines).

However, jet samples probe the $\not\!\!E_{\mathrm{T}}$ scale in events similar to a typical event topology for searches for physics beyond the Standard Model. In dijet events the bisector axis can be utilised to decompose the $\not\!\!E_{\mathrm{T}}$ into two components, similar to the q_{T} axis used before in the $Z \to ee$ event topology. This axis divides the azimuthal opening angle between the two leading jets in two, as illustrated in Fig. 4.17. As the parallel projection of the $\not\!\!E_{\mathrm{T}}$ to the bisector axis is dominated by unclustered energy it is well suited to validate the performance of the correction.

The dijet events are selected requiring at least two jets with corrected $p_{\mathrm{T}} \geq 40$ GeV, where the two leading jets are required to be back-to-back in

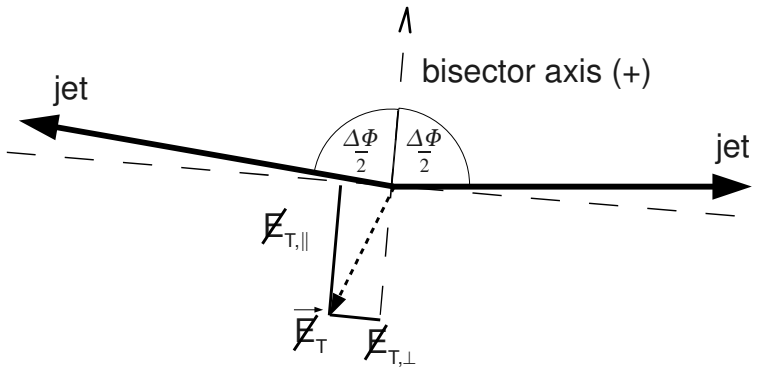

Figure 4.17: Kinematic definitions for dijet events.

the transverse plane ($|\Delta\phi(j1, j2) - \pi| < 1.0$) and within $|\eta| < 3.0$. If any jet candidate above the p_T threshold of 40 GeV is failing the basic JetID requirement, the event is not considered at all. Again two $\not\!\!E_T$ algorithms (Calo and PF $\not\!\!E_T$) have been studied. The data has been recorded during 2010 requiring two jets with an average $p_T \geq 15$ GeV on trigger level. The accumulated amount of data used in these studies corresponds to $0.02\,\text{pb}^{-1}$.

The mean of the parallel projection of $\not\!\!E_T$ on the bisector axis in dependence of the average jet p_T is shown in Fig. 4.18 for Calo $\not\!\!E_T$ and PF $\not\!\!E_T$. The parallel component shows a negative offset for uncorrected MET which is enlarged by the application of type-I correction as it calibrates the jets correctly in the direction opposite to the dijet opening angle. The type-II correction, however, calibrates the rest of the calorimeter energies removing the offset nearly completely. The small remaining offset of the parallel component after the type-II correction is expected as the bisector axis is defined to point towards the smaller opening angle between the jets introducing a bias to negative values.

Independent from the average jet p_T a clear improvement of the $\not\!\!E_T$ scale after the application of type-II corrections is visible for both $\not\!\!E_T$ algorithms. For Calo $\not\!\!E_T$, where the effect of the correction is largest, the bias on the $\not\!\!E_T$ scale is reduced by a factor $\sim$3 to values below $\sim$2 GeV.

As discussed in Sec. 4.3.1 it is difficult to compare the performance of the different algorithms with respect to the resolution. As a first step similar to the

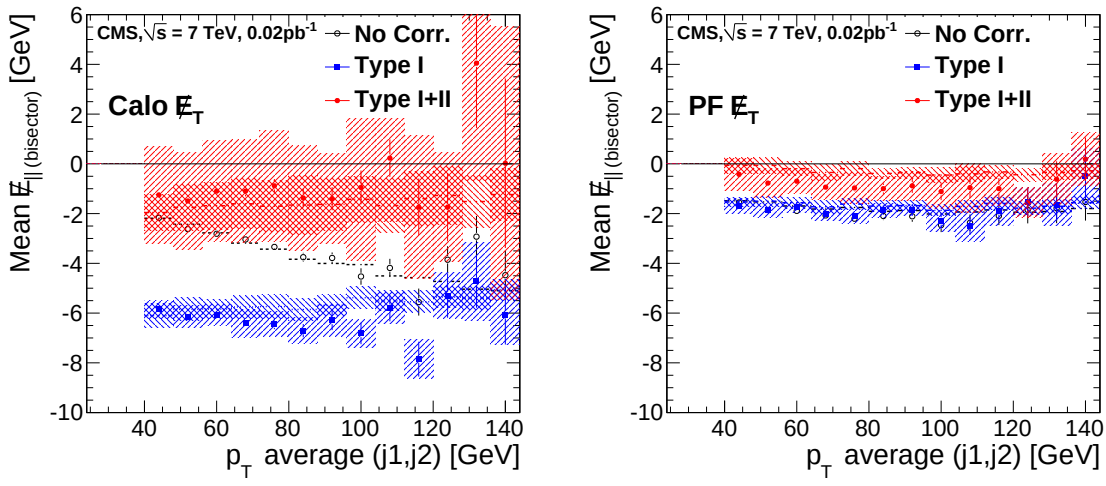

(a) (b)

Figure 4.18: Mean values of $\not\!\!E_{T\parallel,\text{(bisector)}}$ as a function of average p_T of the leading two jets in events compared with Monte Carlo simulation (dashed lines) for uncorrected, type-I corrected, and type-II corrected (left) Calo $\not\!\!E_T$ and (right) PF $\not\!\!E_T$ (published in [59]). The blue band on the distribution with type-I corrections represents the uncertainty due to uncertainties on the jet energy scale. The red band on the distribution with type-II corrections represents uncertainties due to the jet energy scale and statistical uncertainties due to the size of the $Z \to ee$ sample from which the correction for unclustered energies was derived.

procedure applied previously on $Z \to ee$ events the $\not\!\!E_T$ needs to be corrected for the response differences between the algorithms using the scale derived from, e.g. $Z \to ee$. In addition, if the response is studied in dependence of ΣE_T, the upscaling of this quantity needs to be addressed as well. This has been studied in more detail in minimum bias events [67] showing a clear improvement of the resolution for type-I corrected Calo $\not\!\!E_T$ after the application of type-II corrections in multi-jet events as shown in Fig. 4.19. However, the algorithms including the measurement of the track (TC $\not\!\!E_T$, PF $\not\!\!E_T$) show clear improvements in the resolution with respect to Calo $\not\!\!E_T$. As the effect of the type-I and type-II corrections to PF $\not\!\!E_T$ are small only the uncorrected PF $\not\!\!E_T$ is shown here. Overall PF $\not\!\!E_T$ yields the smallest resolution [59].

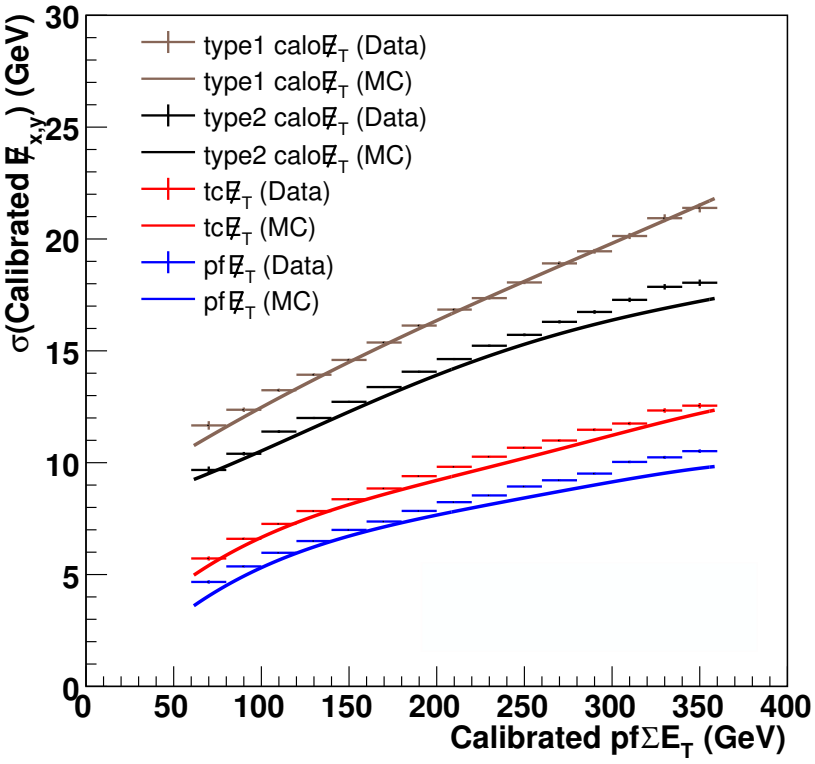

Figure 4.19: Calibrated $\not\!\!E_{\mathrm{T}x,y}$ resolution versus calibrated PF ΣE_{T} for Calo $\not\!\!E_{\mathrm{T}}$, TC $\not\!\!E_{\mathrm{T}}$, and PF $\not\!\!E_{\mathrm{T}}$ in data and simulation taken from [67]. Both, type-I and type-II corrected Calo $\not\!\!E_{\mathrm{T}}$ are shown, while TC and PF $\not\!\!E_{\mathrm{T}}$ are not corrected.

4.4 Large $\not\!\!E_{\mathrm{T}}$ due to Misreconstruction

$\not\!\!E_{\mathrm{T}}$, as a vectorial sum of all transverse momenta measured in the detector, is very sensitive to any possible instrumental mismeasurement. This can be caused by several sources like anomalous signals in the calorimeters, non-collision particles hitting the detector, or collision particles hitting non-instrumented or non-functioning regions of the detector. Such a mismeasurement can easily lead to additional contributions in the tail of the $\not\!\!E_{\mathrm{T}}$ distribution.

Especially for analyses requiring high energetic jets and $\not\!\!E_{\mathrm{T}}$, the understanding of the various sources of high $\not\!\!E_{\mathrm{T}}$ is crucial and, therefore, besides the measurement of scale and resolution, a key ingredient for the measurement of the missing transverse energy. For most of these sources a strategy to identify these problematic events has been developed, allowing a removal of these events for physics analyses. Algorithms correcting the misreconstruction are provided or are being developed for some of the known sources, which is particularly interesting for searches with very low expected event rates.

The available solutions for a basic event cleaning of anomalous signals in the calorimeter have been discussed briefly in Sec. 3.3. Two of the possible causes for additional tails in the $\not\!\!E_{\mathrm{T}}$ distribution are discussed in the following: punch-through of high energetic jets and contributions due to non-functioning detector regions.

4.4.1 Punch-through of High Energetic Jets

As described in Sec. 3.2.3 the Hadron Calorimeter (HCAL) is located almost completely inside the solenoid. In the barrel region this leads to a relatively small thickness ($\gtrsim 6\ \lambda$) of the calorimeter and very high energetic, late showering jets might punch-through the HCAL depositing parts of their energy outside the inner calorimetry. Even including the relatively thin HO ($\sim 1.5\ \lambda$), located outside the solenoid in the barrel region, the thickness in the barrel is only $\gtrsim 10\ \lambda$ so that very high energetic jets might still deposit parts of their energy further outside, e.g. in the muon system. The mismeasurement of jets due to punch-through introduces non-Gaussian tails to the jet momentum resolution, which also leads to additional events in the tail of the $\not\!\!E_{\mathrm{T}}$ distribution. To understand and

quantify the importance of punch-through in events with high $\not\!\!E_{\mathrm{T}}$ MC simulated dijet events have been studied. Here the jets are reconstructed with too small energies due to two main causes:

- **punch-through** : Jets mismeasured due to leakage out of the calorimetry
- **heavy flavour jets**: Jets with large fraction of their energy in b or c quarks decaying partly into e, μ or τ and neutrinos

If the muon system is included, the minimal thickness of the detector rises to $\sim 20\ \lambda$, therefore it is a powerful tool to identify and possibly correct punch-through of high energetic jets. For this purpose, the number of hits in the muon system within the jet cone is used. As the quarks in the heavy flavour jets decay partially into muons, they should leave measurable signs in the muon system as well as the punch-through jets. Still both effects can be distinguished comparing the total number of hits in the muon system and the distribution of hits in the four muon stations. Muons from b or c quark decays have less hits than punch-through jets and the hits are expected in all four muon stations, while less energetic punch-through jets deposit their energy in the first layers of the muon system only.

A method to derive the best suited variables for the identification of punch-through has been developed. As the distributions of these variables might differ between data and simulation, the generator level information is not needed in this method, but is used for validation purposes only. The main idea is to first select a dijet event sample and clean it from heavy flavour jets, using b-tagging algorithms [68; 69]. In a second step the response R of the jets is measured using the average value of the two leading jets ($p_{\mathrm{T,dijet}}$) in the event instead of the generator jet p_{T}:

$$R = \frac{p_{\mathrm{T,jet}} - p_{\mathrm{T,dijet}}}{p_{\mathrm{T,dijet}}}. \tag{4.6}$$

with

$$p_{\mathrm{T,dijet}} = \frac{p_{\mathrm{T,jet1}} + p_{\mathrm{T,jet2}}}{2} \tag{4.7}$$

A Gauss function is fitted to the jet response distribution of the selected events and its mean is used to separate the jets into two samples: one with low response

jets (L), one with high response jets (H). As possible variables the number of hits in the muon drift tubes or muon resistive plate chambers are considered. Besides the total number of hits also the number in each station has been studied as well as the energy deposited in the hadron outer calorimeter. For each variable and variable combination the normalised distribution of low and high response jets is compared and simple cuts on the variables are optimised such that the highest possible $\frac{L-H}{\sqrt{L+H}}$ ratio is achieved.

In simulation the best performance for the identification of punch-through is achieved by requiring

- > 8 hits in the resistive plate chambers in the jet cone and
- ≥ 1 hit in the second or third station of the resistive plate chambers in the jet cone.

To ease the use of the muon hits associated to a jet, the calculation of these variables has been included in the standard reconstruction of the jets and is available on analysis level via the JetID object.

Overall the number of jets affected by punch-through is very small, e.g $\sim 2\%$ of jets with p_{T} $\geq$500 GeV, but an event selection requiring a very high p_{T} of the jets and high $\not\!\!E_{\mathrm{T}}$ can raise this number up to $\sim$70%. The percentage of jets affected by punch-through and the percentage of jets tagged as heavy flavour jets on generator level are shown in dependence of generated jet p_{T} in Fig. 4.20 for simulated QCD dijet events with $\not\!\!E_{\mathrm{T}} \geq 200$ GeV.

The resulting effects from punch-through and heavy flavour jets for the tail of the $\not\!\!E_{\mathrm{T}}$ distribution ($\not\!\!E_{\mathrm{T}} \geq 200$ GeV) in simulated QCD dijet events are shown in Fig. 4.21. Only events with at least one jet with generated $p_{\mathrm{T}} \geq 150$ GeV are considered. In addition at least 2 jets with a reconstructed $p_{\mathrm{T}} \geq 200$ GeV are required. The number of events affected by punch-through in this scenario is $\sim$20%, while the number of events with a b-tagged heavy flavour jet is $\sim$35%[1]. As for the jet resolution, the effect on the $\not\!\!E_{\mathrm{T}}$ tail is highly dependent on the details of the event selection. But, for analyses requiring high energetic jets and

[1]On generator level the number of low response heavy flavour jets with neutrino content was found to be in the order of $\sim$62%

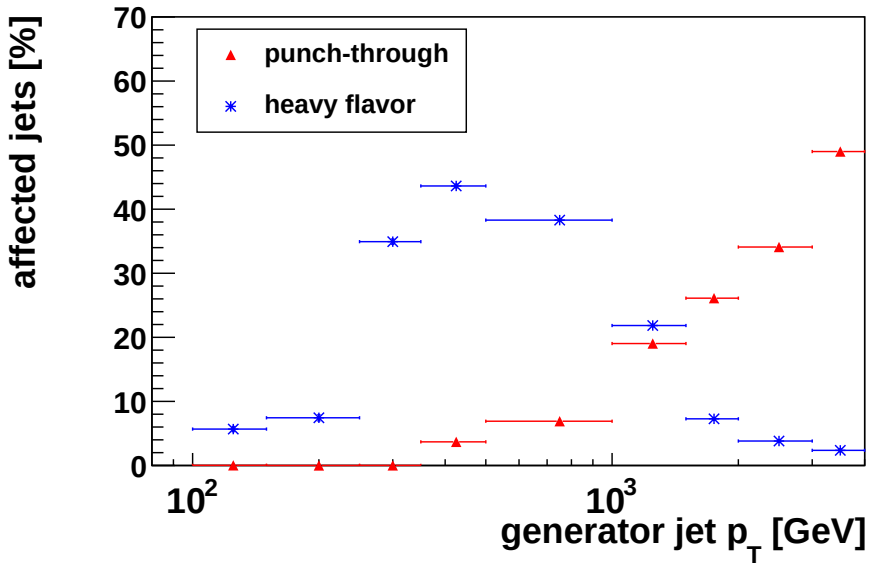

Figure 4.20: Percentage of jets tagged as punch-through or heavy flavour jet (generator level) in dependence of generator jet p_T for events with $\not\!\!E_T \geq 200$ GeV.

$\not\!\!E_T$, the rejection of events affected by punch-through can significantly reduce the number of expected tail events. In principle the correlation between the leakage outside the calorimetry and the muon system variables can also be used to not only identify, but correct for punch-through. First studies using the HMatrix Method [70] have shown promising results and could be investigated further if needed for a specific analysis.

4.4.2 Contributions from non-functioning Detector Regions

If hit by a particle, non-functioning detector regions induce artificial $\not\!\!E_T$ to the event. The $\not\!\!E_T$ is due to the energy of the particle not measured in the malfunctioning detector.

As described in Sec. 3.2.2, about 1% of the ECAL crystals are masked for the reconstruction of higher level objects such as $\not\!\!E_T$ and jets. Although the overall percentage of affected crystals is small, the masked channels still have a significant

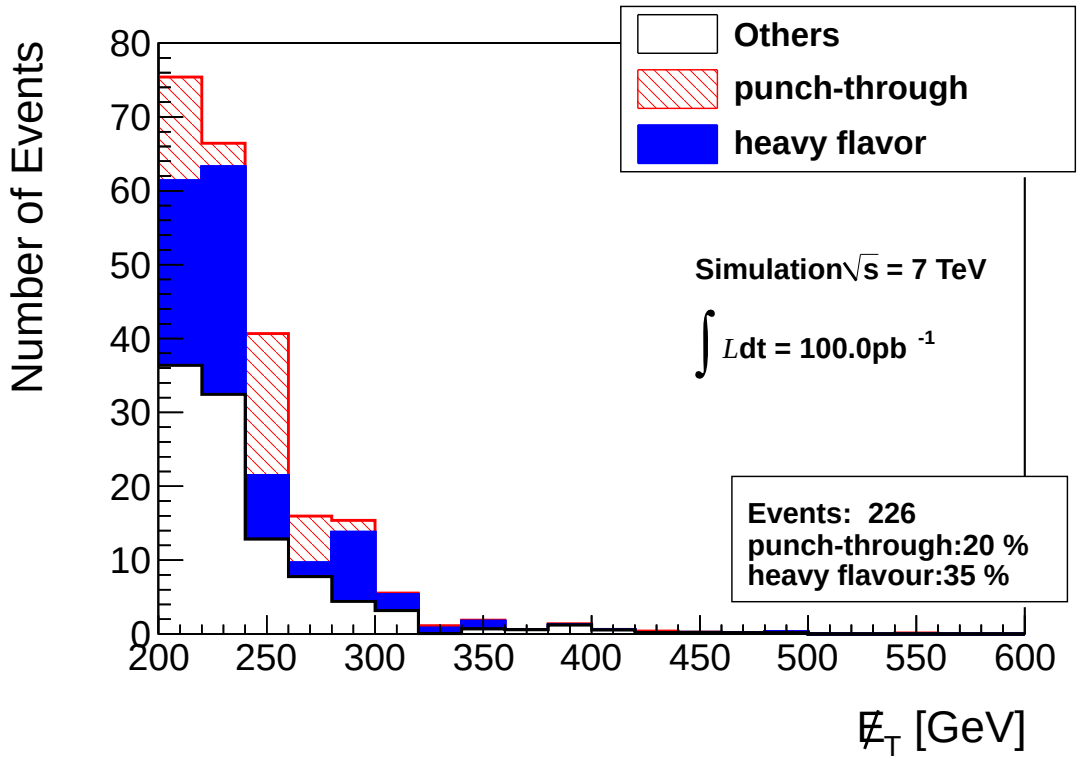

Figure 4.21: $\not\!\!E_T$ distribution ($\not\!\!E_T \geq 200$ GeV) in Monte Carlo simulation of QCD dijet events (jet $p_T \geq 200$ GeV). Events affected by punch-through are shown in red, events with low response heavy-flavour jets in blue.

effect on the tails of the $\not\!\!E_T$ distribution. Especially in events with many jets the probability that one of the particles hits a masked crystal is non negligible. If, in addition, the crystals are adjacent in η-ϕ, the effect is enhanced as the amount of non measured energy increases. This is the case for masked very front end (VFE) and front end (FE) cards, where 5x1 and respectively 5x5 crystals are affected. Overall ∼70% of the masked cells belong to such a cluster.

The effect on the $\not\!\!E_T$ distribution due to the masked FE cards has been studied by masking the corresponding crystals in simulation as well. The effect becomes visible if the resulting $\not\!\!E_T$ distributions with and without masked cells in the simulation are compared. In Fig.4.21 the masked cells are not masked in the simulation, while they are in Fig.4.22. Without the masked cells ∼78% of the events in the high $\not\!\!E_T$ tail can be explained by either heavy flavour jets or punch-

through. After the inclusion this percentage is reduced to ∼49% due to the additional events in the tail. By comparing the total number of events, the additional tail due to masked FE cards is measured to be ∼60% in this specific dijet selection. As for punch-through the percentage of affected events is highly dependent on the details of the event selection. Therefore analyses sensitive to events with large $\not\!\!E_{\mathrm{T}}$ need to identify and possibly reject or recover these events.

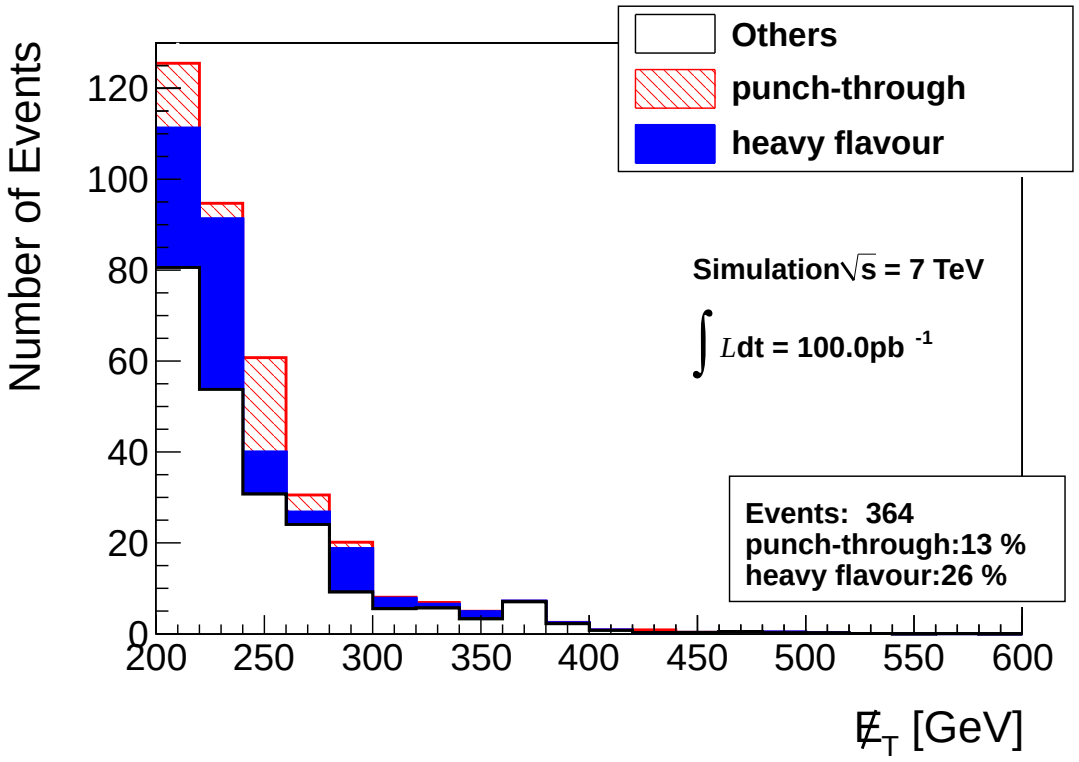

Figure 4.22: Monte Carlo simulation of QCD dijet events ($\not\!\!E_{\mathrm{T}} \geq 200$ GeV,jet $p_{\mathrm{T}} \geq 200$ GeV). Other than in Fig. 4.21 ECAL cells masked in the event reconstruction on data level are also masked in the reconstruction of the simulated events. Events affected by punch-through are shown in red, events with low response heavy-flavour jets in blue.

Around 70% of the masked FE/VFE cards have a measurement from the separate readout of the L1 trigger available. The trigger readout saturates at high energies, but for events with smaller energies the trigger information can be used to recover the event. Even if the energy is above the saturation threshold the

information can be used to identify and reject affected events [59; 71]. The trigger saturation threshold was raised from 64 GeV to 128 GeV in 2011 to enlarge the recovery potential of the events affected by masked cells. For the remaining 30% of masked channels no measurement of the deposited energy is available. Here the energy deposited in neighbouring crystals around the masked cells can be utilised to identify an energy deposit and thus reject the event [59; 71].

In summary, two important causes of artificial high $\not\!\!E_{\mathrm{T}}$ have been discussed: punch-through of high energetic jets and contributions due to non-functioning detector regions. For both methods a basic strategy to identify possibly affected events has been presented: in case of punch-through the number of hits in the muon system behind a jet can be utilised, while in case of non-functioning detector regions in the CMS ECAL either the trigger primitive information or the energy deposited around a masked detector region can be used. The events with $\not\!\!E_{\mathrm{T}}$ above 300 GeV passing the signal selection of the SUSY search presented in the next chapter have been checked for possible signs of either of the discussed effects. In both, signal and selected control samples, no obvious indication of fake energies was found.

For the low $\not\!\!E_{\mathrm{T}}$ region the derived type-II correction shows a clear improvement of the $\not\!\!E_{\mathrm{T}}$ scale in all studied event topologies. The adjustment of the unclustered energy leads, in principle, to an improvement of the resolution, while the unavoidable upscaling of noise by the correction contradicts this effect. For Calo $\not\!\!E_{\mathrm{T}}$, where the effect of the corrections is large, the resolution shows a clear improvement after the correction, especially in minimum bias events. For the particle-flow algorithm the overall effect from the type-II corrections is small and the type-II correction might slightly worsen the resulting resolution in some settings. Thus the correction should only be applied after careful balancing the advantages and disadvantages for the specific usecase.

The derived type-II scale has been applied as default correction to Calo $\not\!\!E_{\mathrm{T}}$ for several CMS analyses studying the scale and resolution of $\not\!\!E_{\mathrm{T}}$ published here [59] together with the results from the validation in dijet events presented in Sec. 4.3.2.

5

Search for Supersymmetry in Events with Photons and $\not\!\!E_{\mathrm{T}}$

In this chapter a search for supersymmetry in events with at least one isolated photon, jets and $\not\!\!E_{\mathrm{T}}$ on $4.32\,\mathrm{fb}^{-1}$ of the 2011 data is presented. As discussed in Sec. 2.2.2 the production of photons is expected in some SUSY models with gauge-mediated symmetry breaking. CMS has performed two searches for GMSB final states with photons with the $35\,\mathrm{pb}^{-1}$ dataset accumulated in 2010. One is analysing events with diphotons [72], the other events with a single photon and a lepton [73].

The more inclusive single-photon analysis presented here adds an important channel to the CMS GMSB SUSY searches. Like the diphoton analysis it includes final states with two photons, but in addition it includes events where one photon is not detected because of the limited geometrical or kinematical acceptance of the detector. Furthermore it is sensitive to final states with a single photon, where only one neutralino NLSP decays into a photon, while the other decays into a W or Z boson depending on the composition of the NLSP as discussed in Sec. 2.2.2.1. The $1.1\,\mathrm{fb}^{-1}$ results [74; 75] have already been presented at the Lepton-Photon [76] and SUSY [77] conferences, here the analysis is extended to the full integrated luminosity of the year 2011 [78].

This analysis requires one photon, $\not\!\!E_{\mathrm{T}}$ and jets in the final state. Dominant standard model background processes are direct photon-jet production and QCD multi-jet production where one jet fakes a photon. QCD events have only small

intrinsic $\not{E}_{\mathrm{T}}$, but the resolution of the jet energy measurement together with the large cross section leads to a significant contribution in the tail of the $\not{E}_{\mathrm{T}}$ distribution. Other backgrounds arise from electroweak electron production, i.e. $W \to e\nu$, where an electron fakes a photon. Additional contributions are expected from initial or final state radiated photons.

Compared to the diphoton final state, the background to the single photon channel is larger. Therefore single photon trigger thresholds are too large for the efficient selection of many SUSY benchmark points, so that for this analysis a cross-trigger based on a single photon and hadronic transverse energy (HT) is utilised.

The main backgrounds are modelled using data driven techniques. The photon-jet and multi-jet background (γ/QCD) is modelled using an exclusive data control sample, where one jet for each event is required to fulfil a loose 'fake' photon ID (γ_{Jet}). The electroweak backgrounds ($e \to \gamma$) are modelled using an exclusive electron data control sample.

After a detailed description of the used dataset and the applied selection criteria in Sec. 5.1, the estimation of Standard Model backgrounds is discussed in Sec. 5.2. The results of the measurement in the 2011 dataset are compared to the combined Standard Model estimates in different signal regions as shown in Sec. 5.3. Finally, the interpretation of the obtained result in different GGM parameter space regions is presented in Sec. 5.4.

5.1 Event Selection

5.1.1 Trigger

The analysis is using a data sample with an integrated luminosity of $4.32\,\mathrm{fb}^{-1}$. The dataset is accumulated using a set of triggers which require a single photon with $p_{\mathrm{T}} \geq 70$ GeV and a minimum hadronic transverse energy HT[1]. The HT threshold for the Trigger is raised for the later runs to a maximum of 400 GeV and is calculated from all calorimeter jets passing the JetID requirement with $p_{\mathrm{T}} > 40$ GeV and $|\eta| \leq 3.0$.

[1] $HT \geq 200 - 400\,\mathrm{GeV}$

Up to run-number 165970 the JetID requirement on HLT level contained a cut on the number of calorimeter towers carrying 90% of the jet energy ($n90 \geq 2$). This was replaced by a cut on the number of calorimeter hits carrying 90% of the jet energy ($n90Hits \geq 2$) which adjusts the online cuts to match the recommended JetID requirements. The jets reconstructed from the photon energy deposits tend to pass the JetID cuts with the cut on $n90Hits$, but some of them fail the cut on $n90$. Therefore in the first $\sim 300\,\mathrm{pb}^{-1}$ of the dataset the efficiency of the HT requirement of the trigger drops as these jets are not included in the calculation of HT. The drop of efficiency in events with one photon in the barrel region ($|\eta| \leq 1.4$) has been studied using a single photon dataset as denominator. The corresponding trigger efficiencies of the HT requirement can be found in App. A.5. To avoid effects from this inefficiency the affected data ($\sim 300\,\mathrm{pb}^{-1}$) is not used in this analysis.

For the run range used in this analysis the highest HT threshold on trigger level is 400 GeV, where the HT requirement of the trigger becomes fully efficient for an offline HT selection requiring $HT \geq 450\,\mathrm{GeV}$ as shown in Fig. 5.1. The efficiency of the photon requirement of the trigger was found to be $\sim$ 100% efficient for photons with $p_\mathrm{T} \geq 80$ GeV as shown in Fig. 5.1(b). In the figure only photons passing the photon identification criteria described in Sec. 3.4.2 are shown. As the isolation requirements applied on trigger level are looser than the offline selection, also events with high p_T photon-like objects not passing the offline selection are triggered. Additional low p_T photons in these events passing the γ offline selection lead to the enhanced efficiency below the trigger threshold. Technical details of the selected runs and the used datasets can be found in App. A.4.

5.1.2 Simulated Datasets

Simulated events of Standard Model processes are mostly used to validate the data driven background estimation methods, although for some small background contributions the simulated events are used directly.

For comparison with Standard Model expectations GGM Signal MC samples with a wino- or bino-like NSLP have been produced for the CMS SUSY analyses

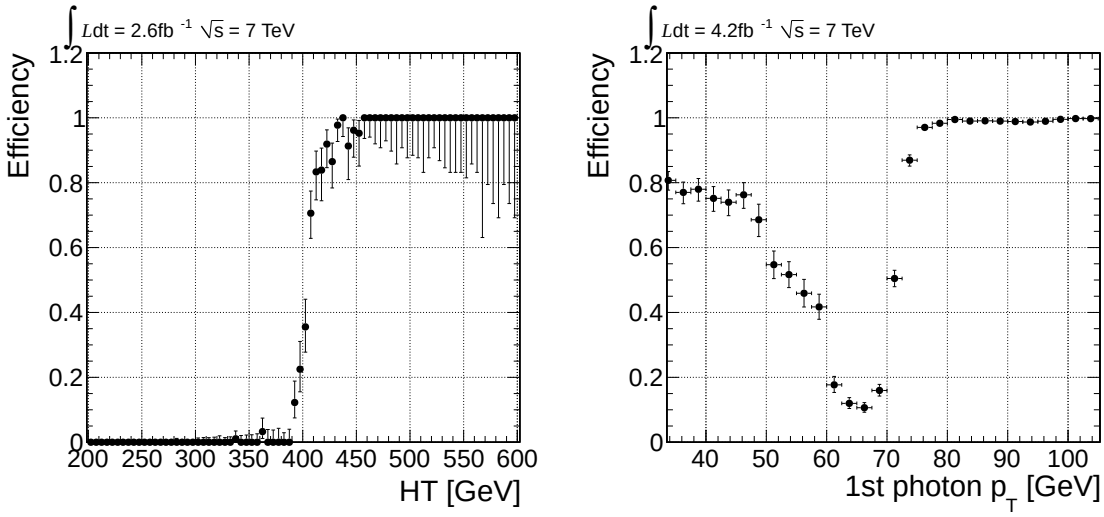

(a) (b)

Figure 5.1: Trigger Efficiency (a) of the HT requirement and (b) of the photon requirement of the used Photon-HT cross trigger [79].

with photons. Here, as discussed in Sec 2.2.2.1, simplified GGM spectra are assumed. The squark and gluino masses vary between 160 and 2000 GeV in these samples, while the NLSP mass is in the range between 150 and 1050 GeV. Two sample GGM parameter points are used for reference in the following sections:

GGM A: $m_{\tilde{q}} = 2500$ GeV, $m_{\tilde{g}} = 800$ GeV, $m_{\tilde{\chi}_1^0(\mathrm{bino})} = 650$ GeV
Cross section (NLO): 0.059 pb
Number of generated events: 10 000

GGM B: $m_{\tilde{q}} = 1280$ GeV, $m_{\tilde{g}} = 1200$ GeV, $m_{\tilde{\chi}_1^0(\mathrm{bino})} = 375$ GeV
Cross section (NLO): 0.007 pb
Number of generated events: 10 000

For both reference points a bino-like neutralino is assumed. A more detailed, technical description of all simulated Standard Model and GGM signal samples can be found in App. A.4.

All used MC samples have been generated with a pile up distribution matching roughly the pile up conditions for the 2011 data taking. In order to account for

the changing pile up conditions during the year, the number of generated primary vertices in the simulation is reweighted to match the average distribution obtained in the used data set, i.e. 9.8 primary vertices on average for the 2011 data.

5.1.3 Event Selection

To meet the trigger requirements and select the events of interest the following cuts are applied:

- $\geq$1 photon with $p_{\mathrm{T}} \geq 80$ GeV and $|\eta| \leq 1.4$
- $\geq$2 jets with $p_{\mathrm{T}} \geq 30$ GeV and $|\eta| \leq 2.6$
- $HT \geq$450 GeV.

A tighter cut on these or other variables could improve the signal to background ratio, and, thus the exclusion reach for some parameter points. However, the kinematics of the GGM events depend on the parameter region and the mixture of the neutralino. Thus, in general, the selection cuts are choosen to be as inclusive as possible to avoid dependencies on the details of the GGM model. Only for the jet multiplicity cut a less inclusive selection requiring $\geq$3 jets has been studied besides the selection with $\geq$2 jets. The results of both selections will be presented in parallel in the following sections.

For the final selection the photon is selected using the identification criteria as described in Sec. 3.4.2. For the selection of the control samples needed for the data driven background estimation the cuts are applied to the corresponding fakeable objects (γ_{Jet},γ_e) instead[1].

The particle flow algorithm is used for the reconstruction of jets and the jets are required to be within $\eta < 2.6$ and have $p_{\mathrm{T}} > 30$ GeV. However, for the calculation of HT, calorimeter jets with $p_{\mathrm{T}} > 40$ GeV and $|\eta| \leq 3.0$ are used to make the HT calculation similar to the calculation on trigger level[2].

Usually the photon-like objects (γ, γ_{Jet} or γ_e) and isolated leptons (muons, electrons)[3] are treated also as jets and thus might appear in the jet count. To

[1] See Sec. 3.4.2 (Sec. 3.4.3) for the definition of jet-photon (electron-photon) fakeable objects.

[2] In the offline calculation of HT the jets are additionally corrected for pile up effects ($L1FastJet$).

[3] see Sec. 3.4.3 and 3.4.4 for details on the identification criteria

avoid this, the jet collection is cleaned from these objects by neglecting all jets with a small distance in η and ϕ between the jet and the leading photon-like object or isolated lepton ($\Delta\mathrm{R} \leq 0.3$). For consistency the calorimeter jets used for the HT calculation are cleaned in the same way [1]. After this cross cleaning of object collections, jets do not overlap with isolated muons or electrons nor with the leading photon object and the HT corresponds to the transverse energy of all these jets plus the photon-like object.

While the photons usually have a very small amount of their energy deposited in the hadron calorimeter, the situation is different for some of the jets which are reconstructed as a photon (γ_{Jet}). Here, due to the looser isolation criteria of the γ_{Jet} compared to the γ, the hadronic energy fraction is mostly non-negligible. To avoid a bias between the photon and the γ_{Jet} control sample the four-momentum of the photon-like object is replaced by the momentum of the matching pile up corrected jet. The matching jet is required to have a relative energy $E_{T,rel} = \frac{E_{T,jet}}{E_{T,\gamma/\gamma_{\mathrm{Jet}}/\gamma_e}} > 0.95$ and to be within $\Delta\mathrm{R} \leq 0.3$ around the photon[2].

In a first step the whole $\not{E}_{\mathrm{T}}$ spectrum is used to study the expected Standard Model backgrounds, while the final signal region of the analysis is reduced to events with high $\not{E}_{\mathrm{T}}$ ($\not{E}_{\mathrm{T}} > 100$ GeV). For both purposes the raw, not corrected PF $\not{E}_{\mathrm{T}}$ is used. The $\not{E}_{\mathrm{T}}$ type-I corrections are not optimised to handle jets with a very large fraction of their energy deposited in the electromagnetic calorimeter, i.e. jets reconstructed from electron or photon energy deposits. Consequently the currently available correction tends to introduce a bias between γ and γ_{Jet} sample, and, thus, is not applied in the following.

[1] The jet matching the leading photon-like object is also removed. However, the p_{T} of the reconstructed photon object is added to the HT instead.

[2] If no jet fulfilling these criteria is found, the photon object is used.

5.2 Estimation of SM Backgrounds

To estimate the amount of Standard Model events expected in a signal region with high $\not\!\!E_{\mathrm{T}}$ the expected contribution from each of the Standard Model backgrounds is evaluated. As described above, the main backgrounds from QCD and electroweak processes are modelled using data events, while for the remaining backgrounds plain simulation is used.

In the following section the background estimation method for the γ/QCD background is described. First simulated events are used to illustrate the method and show that it works on simulation (Sec. 5.2.1.1), the background estimation from data is then shown in Sec. 5.2.1.3. The obtained results from data and simulation are summarised in Table 5.1. Similarly the $e \to \gamma$ background will be discussed in Sec. 5.2.2. Finally, further contribution from initial and final state radiation (ISR/FSR) are discussed in Sec. 5.2.3.

5.2.1 Photon/QCD Background

The γ/QCD background is a composition of direct photon-jet production and of QCD multi-jet production where one jet fakes a photon. Compared to the resolution for hadronic energy deposits, the resolution of photons is very good due to the excellent resolution of the CMS ECAL. Consequently, in the γ/QCD events, the $\not\!\!E_{\mathrm{T}}$ is predominantly due to the jet resolution including non-Gaussian tails.

Due to the high fraction of energy deposited in the ECAL, also the resolution of jets faking a photon is better than for average jets. Therefore, the response of γ_{Jet} is assumed to be similar to photons, which is utilised to estimate the background contributions from γ/QCD events from a γ_{Jet} data control sample.

The control sample is selected by applying the same signal selection cuts as defined in Sec. 5.1.3, except that instead for a photon a photon-like object (γ_{Jet}) with loose identification criteria as defined in Sec. 3.4.2 is required. The γ_{Jet} definition is orthogonal to the γ identification criteria in the signal selection, so that the data control sample and the signal sample have no overlap. Possible signal contamination has been studied and will be discussed later. The p_{T} distribution

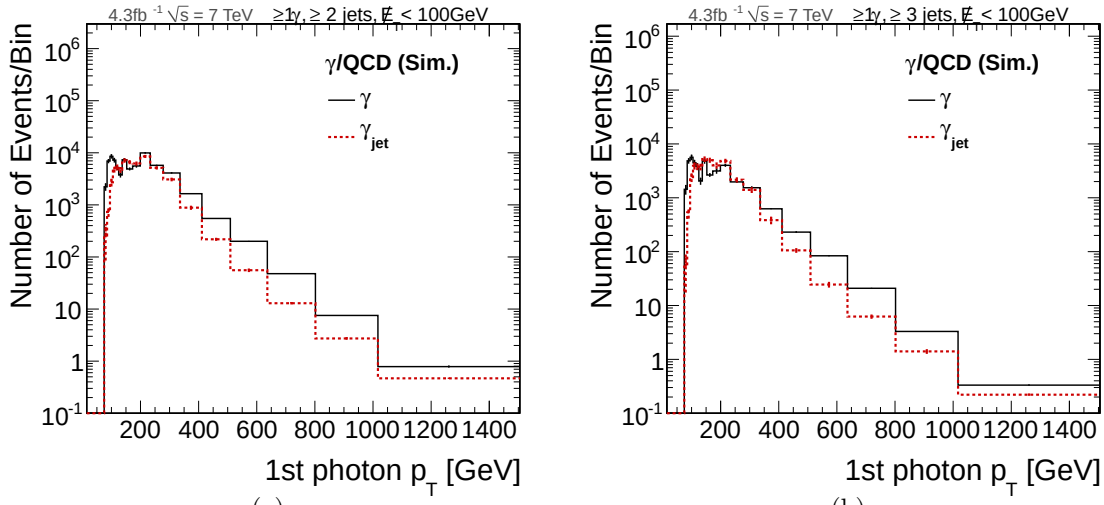

(a) (b)

Figure 5.2: Simulation of γ/QCD events: p_T distribution of leading photon-like object for signal (γ) and control (γ_{Jet}) sample in events with (a) $\geq$2 jets and (b) $\geq$3 jets for events with $\not{E}_{\mathrm{T}} < 100$ GeV.

of photons and γ_{Jet}objects in simulated γ/QCD events are shown in Fig. 5.2 for events with $\geq$2 and $\geq$3 jets.

To estimate the $\not{E}_{\mathrm{T}}$ distribution in the tight photon sample, the events in the control sample are reweighted so that the photon[1] p_{T} distribution agrees. Therefore the inverse weight w^{-1} is defined as the ratio of the number of γ_{Jet} objects to the number of tight photons in each photon p_{T} bin:

$$w^{-1}(p_T^{\gamma}) = \frac{\#\gamma_{\mathrm{Jet}}}{\#\gamma}. \tag{5.1}$$

The distribution of the inverse weight as defined in Eq. (5.1) is determined in a signal depleted region with $\not{E}_{\mathrm{T}} < 100$ GeV. The resulting histogram, or more precisely the inverse value in each photon p_{T} bin of the histogram, is then used to weight the $\not{E}_{\mathrm{T}}$ distribution of the γ_{Jet} sample leading to an estimate for the γ/QCD

[1]In the following 'photon' is usually used to denote all photon-like objects (γ,γ_{Jet},γ_e). A photon passing the photon identification described above is referred to as 'tight' photon.

background. The uncertainty in each bin of the inverted weight distribution is propagated to the control sample as a systematic uncertainty for the reweighting.

The resulting shape and normalisation of the distribution of inverse weights shows a slight dependence of the number of jets in the event. Thus events with exactly two jets are corrected with the weight distribution obtained in these events only, while events with higher jet multiplicities are corrected with the average weight distribution observed in event with three or more jets. To account for the remaining shape differences (see App. A.6.1 for details) an additional systematic uncertainty of 10% is applied to these events. The effect of an additional correction due to the different normalisations of the weight distribution was found to be negligible (see App. A.8.2) and thus is not applied in the following.

The systematic uncertainty due to the extrapolation of the weight in a signal depleted region to the whole control sample is expected to be small, as the whole photon p_{T} distribution, up to the highest values, is dominated by events with low $\not{E}_{\mathrm{T}}$ as shown exemplary for data[1] in Fig. 5.3. To further evaluate this assumption the inverse weight distributions obtained in the control region, i.e. in a region with $\not{E}_{\mathrm{T}} < 100$ GeV and in the whole sample have been compared in simulated events as shown in Fig. 5.4. The largest relative difference between both distributions is in the order of 5% for all photon momenta and is assigned as an additional systematic uncertainty to the γ/QCD background prediction.

Similarly the effect from other standard model processes or possible SUSY signal on the inverse weight has been studied on simulated events. For this purpose the resulting weights in dependence of the γ p_{T} from γ/QCD simulation have been compared to the corresponding values obtained on a sample with all possible contributions from standard model processes, or, respectively, on a sample containing GGM SUSY Signal. In both cases the relative difference is found to be smaller than 1% and can safely be neglected[2].

In the following section the method is shown to work for simulation, before it is applied on data events in Sec. 5.2.1.3.

[1] MC simulation yields similar results.
[2] See App.A.6.3 for the corresponding ratio plots.

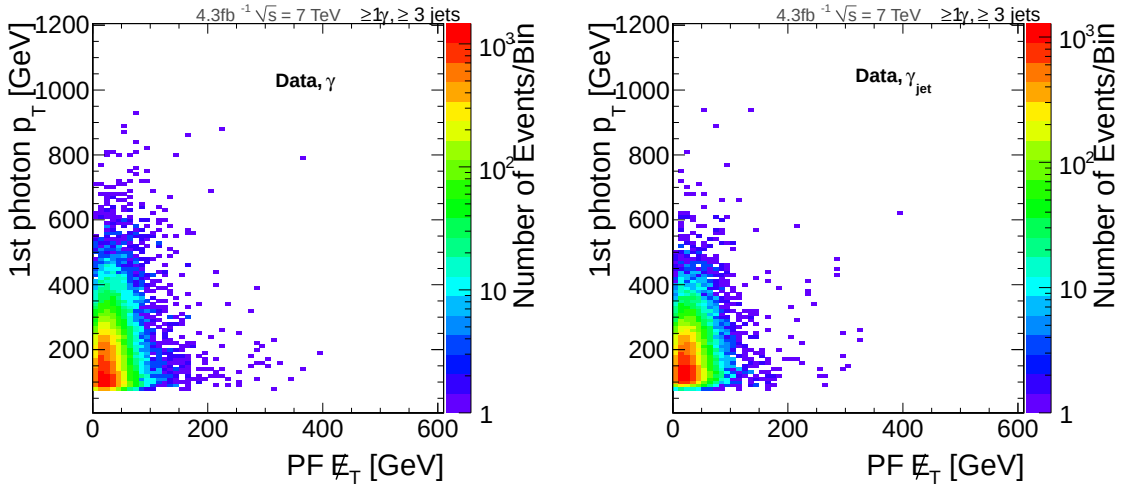

(a) (b)

Figure 5.3: Data (4.32 fb^{-1}): Correlation between $\not{E}_{\mathrm{T}}$ and the p_{T} of the leading photon-like object in the (a) γ and (b) γ_{Jet} sample in events with $\geq$3 jets.

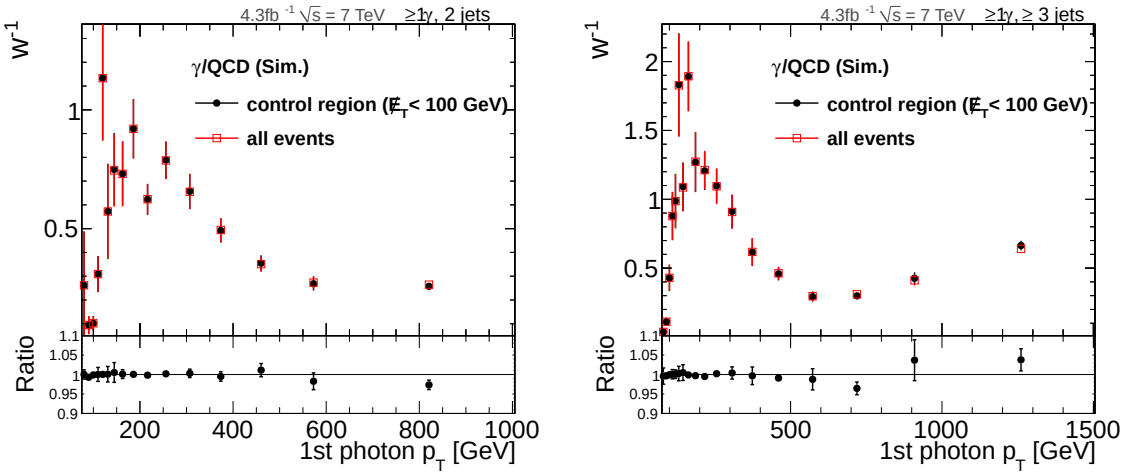

(a) (b)

Figure 5.4: Simulation of γ/QCD events: Comparison of the ratio of γ_{Jet} to γ events in dependence of the leading photon p_{T} for the whole sample and for events in the control region only (MET <100 GeV) for (a) 2 and (b) $\geq$3 jets.

5.2.1.1 Closure Test

The dependence of the inverse weight from the γ p_{T} in the γ/QCD Monte Carlo sample has already been shown in Fig. 5.4 for events with $\geq$2($\geq$3) jets. Both distributions show a similar dependence on the p_{T} of the photon-like object.

The prediction of the γ/QCD background is obtained by reweighting the simulated γ_{Jet} sample by the weights obtained in . The resulting prediction is shown in Fig. 5.5 and compared to direct MC simulation. The corresponding event yields for three different signal region definitions are summarised in Table 5.1. The method closes within the uncertainties. The corresponding reweighted photon p_{T} distributions are shown in App. A.6.2.

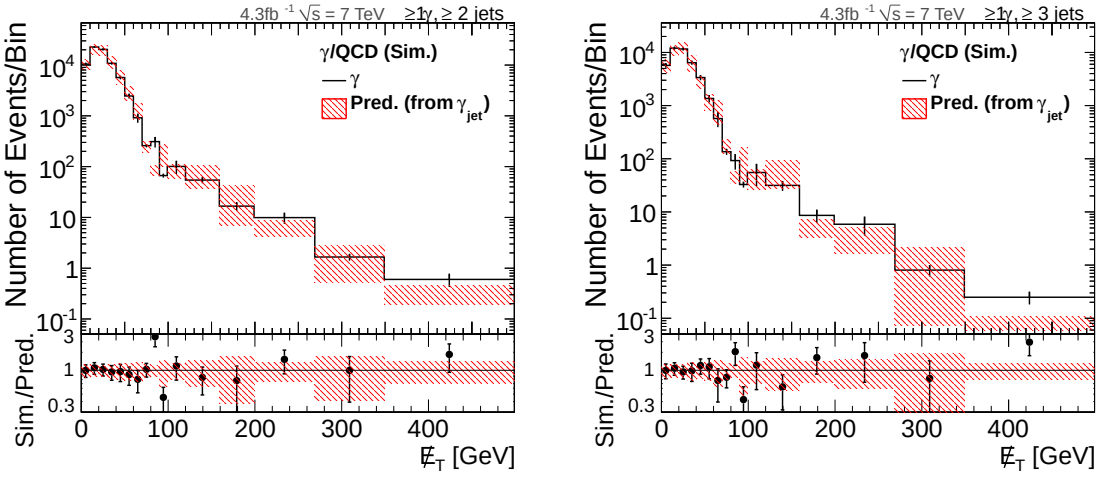

(a) (b)

Figure 5.5: Simulation of γ/QCD events: $\not\!\!E_{\mathrm{T}}$ background prediction derived by reweighting the γ_{Jet} control sample as described above. The systematic uncertainty due to statistical errors of the weights and the kinematical differences between control region and the whole spectrum is shown in combination with the statistical error of the control sample as hatched band for events with (a) $\geq$2 and (b) $\geq$3 jets.

5.2.1.2 Contributions from other processes

The contribution of other Standard Model processes and possible GGM signal to the obtained weights has been discussed above and was found to be negligible. However Standard Model processes can contribute to the resulting γ/QCD background prediction, if the events contain a jet passing the γ_{Jet} identification criteria[1]. Of course some jets in the W and $t\bar{t}$ sample are also passing the γ identification and thus slightly enhance the amount of expected Standard Model background events. However, the probability of a jet to pass the γ_{Jet} or γ identification is expected to be similar as in γ/QCD events. Thus, within the systematic uncertainties, the additional contributions are well described by the small additional γ_{Jet} control sample selected from W and $t\bar{t}$ events. The resulting contribution from simulated W and $t\bar{t}$ events is shown in Fig. 5.6(a), where it is compared to direct simulation of the total SM background including γ/QCD events. Overall the contributions from W and $t\bar{t}$ events are small compared to the γ/QCD events.

Also possible SUSY GGM signal events, can contribute to the resulting background prediction in the high $\not{E}_{\mathrm{T}}$ signal region as shown in Fig. 5.6(b) for a typical signal benchmark scenario ($m_{\tilde{q}} = 2500$ GeV, $m_{\tilde{g}} = 800$ GeV, $m_{\tilde{\chi}_1^0(\mathrm{bino})} = 650$ GeV). The signal contamination in the γ_{Jet} control sample is governed by the probability for a real photon from a signal event to pass the γ_{Jet} identification criteria. The exact value depends on the photon momentum and is generally between 15% and 20%. To account for this effect signal contamination is treated in the statistical interpretation of the result.

[1] In principle, also events with an electron or a real photon (ISR/FSR) passing the γ_{Jet} identification can contribute. However, the contribution from electrons and photons was found to be very small compared to the contribution from jets. Possible overlap with the estimated ISR/FSR background (Sec. 5.2.3) and $e \to \gamma$ (Sec. 5.2.2) background is included within the systematic uncertainties.

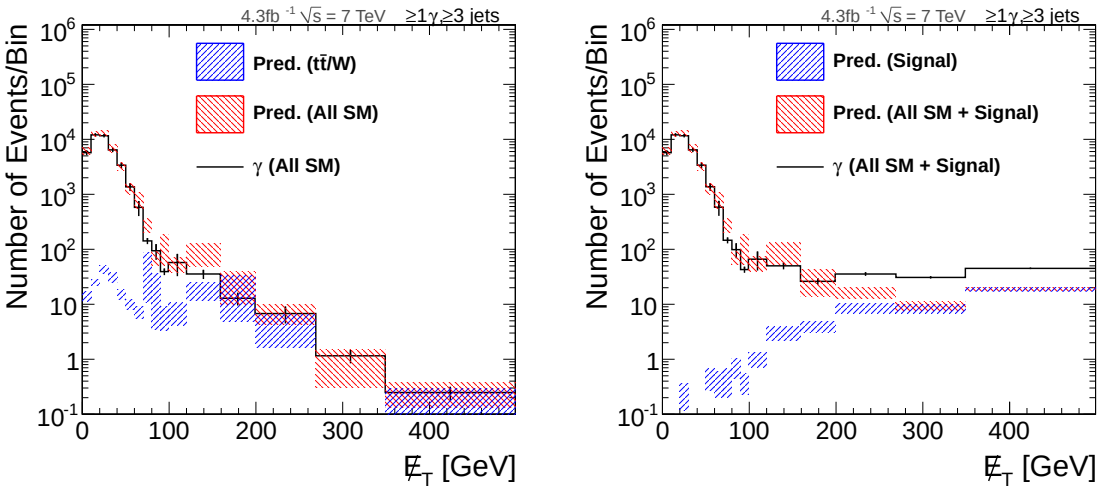

(a) (b)

Figure 5.6: γ/QCD background estimation with (a) contribution from electroweak processes and (b) contribution from electroweak processes and GMSB events ($m_{\tilde{q}} = 2500$ GeV, $m_{\tilde{g}} = 800$ GeV, $m_{\tilde{\chi}_1^0(\text{bino})} = 650$ GeV) in events with $\geq$3 jets. The total γ/QCD background prediction is visualised with the red error band. The contribution from (a) electroweak and (b) GGM events is shown with the blue hatched uncertainty band.

5.2.1.3 Prediction for Data

Now, after the method has been shown to close on simulation, in this section the data driven prediction is discussed. Figure 5.7 shows the p_{T} distribution of the leading photon-like object in the signal selection in data and in the unweighted data control sample used to model the γ/QCD background. For both jet selections only events with $\not{E}_{\mathrm{T}} < 100$ GeV are shown.

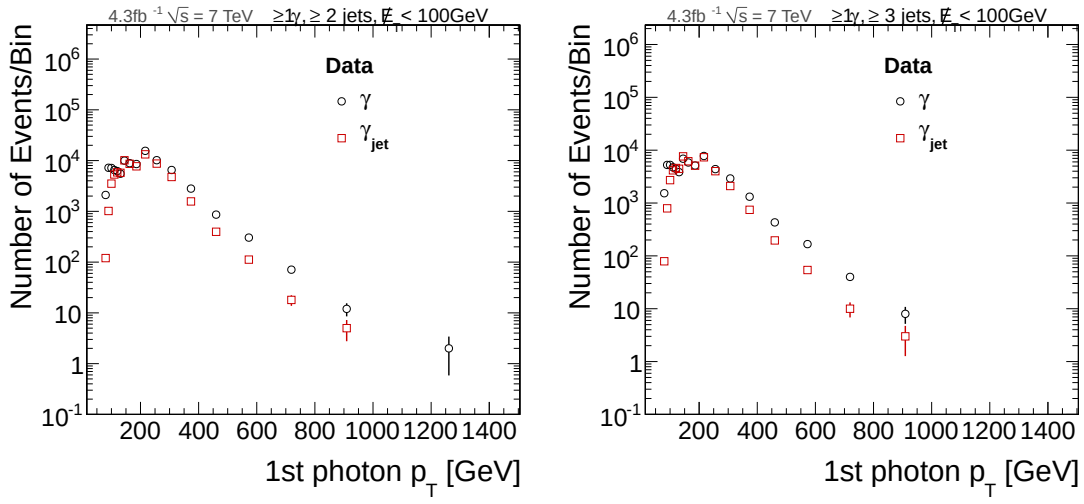

Figure 5.7: Data ($4.32\,\mathrm{fb}^{-1}$): p_T distribution of the leading photon-like object in the γ and γ_{Jet} sample in events with $\not{E}_{\mathrm{T}} < 100$ GeV and (a) $\geq$2 or (b) $\geq$3 jets.

The inverse weights measured in γ and γ_{Jet} events in the $\not{E}_{\mathrm{T}} < 100$ GeV selection are shown in Fig. 5.8. As described above the statistical error in each bin of the histogram is taken as main systematic uncertainty on the weight. In addition the 5% uncertainty due to kinematic differences between the signal depleted control region ($\not{E}_{\mathrm{T}} < 100\,\mathrm{GeV}$) and the whole dataset is considered.

The obtained prediction is listed for three different signal region definitions in Table 5.1, while the predicted $\not{E}_{\mathrm{T}}$ distribution is shown in Fig. 5.9. For comparison the results from simulation (presented in Sec. 5.2.1.1) are shown in the same table. The event yields from simulation disagree clearly with the values obtained from data, while the estimate from simulation agrees nicely with the number of simulated signal events (as shown also in Fig. 5.5). The discrepancy between

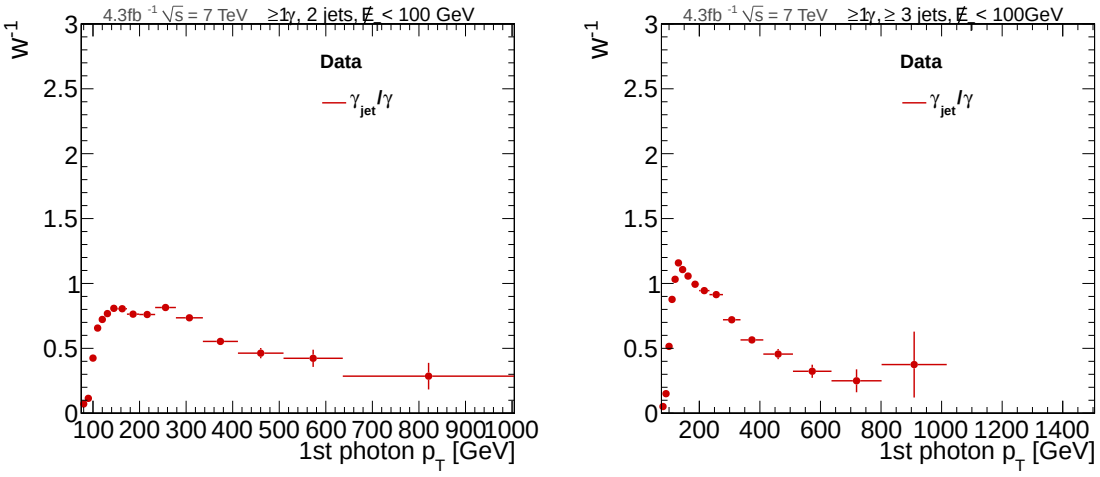

(a) (b)

Figure 5.8: Data ($4.32\,\mathrm{fb}^{-1}$): Ratio of γ_{Jet} to γ events in dependence of the leading photon p_{T} in events with $\not\!\!E_{\mathrm{T}} < 100$ GeV and (a) 2 or (b) $\geq$3 jets.

data and simulation is due to imperfect modeling of the very high $\not\!\!E_{\mathrm{T}}$ tail in the simulation, which is, especially in events with multiple jets, expected for the used simulation (PYTHIA [65], no NLO corrections). The observed differences between data and simulation enhance the importance of a data driven prediction of the γ/QCD background.

Table 5.1: Expected event yields of the γ/QCD background estimation method for three different signal regions ($\not{E}_{\mathrm{T}} > 100/200/350$ GeV). The event yields correspond to a luminosity of 4.32 fb^{-1}.

γ/QCD	$MET \geq 100$ GeV			$MET \geq 200$ GeV			$MET \geq 350$ GeV		
$\geq$1 photon, $\geq$2 jets		(stat)	(sys)		(stat)	(sys)		(stat)	(sys)
Estimate from data	608	$\pm$47	$^{+54}_{-54}$	91	$\pm$16	$^{+9.9}_{-9.9}$	6.8	$\pm$4.1	$^{+0.8}_{-0.8}$
Estimate from simulation	190	$\pm$40	$^{+42}_{-42}$	8.5	$\pm$1.9	$^{+2.3}_{-2.3}$	0.4	$\pm$0.1	$^{+0.1}_{-0.1}$
Direct simulation	184	$\pm$31		12	$\pm$2.5		0.7	$\pm$0.2	
$\geq$1 photon, $\geq$3 jets		(stat)	(sys)		(stat)	(sys)		(stat)	(sys)
Estimate from data	361	$\pm$40	$^{+33}_{-33}$	44	$\pm$10	$^{+4.0}_{-4.0}$	3.1	$\pm$3.1	$^{+0.5}_{-0.5}$
Estimate from simulation	115	$\pm$34	$^{+26}_{-26}$	4.5	$\pm$1.7	$^{+1.5}_{-1.5}$	0.1	$\pm$0.03	$^{+0.02}_{-0.02}$
Direct simulation	102	$\pm$26		6.9	$\pm$2.3		0.3	$\pm$0.1	

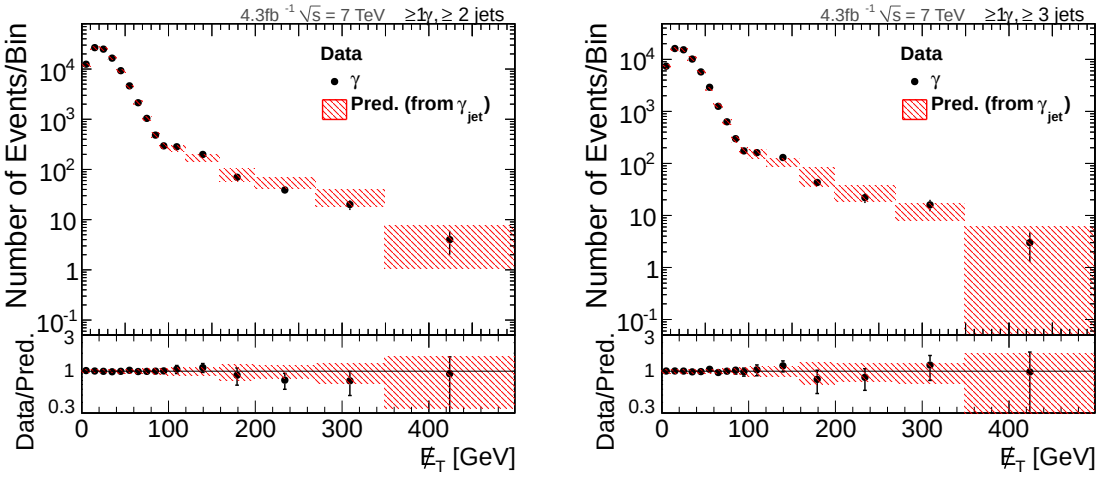

(a) (b)

Figure 5.9: Data (4.32 fb^{-1}): Comparison between events passing the tight photon selection and the data γ/QCD background prediction derived by reweighting the γ_{Jet} control sample for events with (a) $\geq$2 and (b) $\geq$3 jets. Note, that the shown data contains also additional backgrounds and possible signal.

5.2.2 $e \to \gamma$ Background

Another, however already minor, background contribution to this single photon analysis is coming from electrons faking the tight photon identification. These electrons originate mainly from semileptonic $t\bar{t}$ and W events, where, in addition to the electrons and jets, missing transverse energy is produced due to neutrinos. Other contributions originate from electroweak initial state or final state radiation (ISR and FSR). The strategy followed to model this background contribution is similar to the diphoton analysis [57]: the signal selection is applied, but instead of a photon an electron (γ_e) as defined in Sec. 3.4.2 is required, in order to select the control sample. The probability for an electron to fake a photon has been measured on $Z \to ee$ events in data and simulation [57]. In general, the probability is found to decrease in dependence of the transverse momentum of the electron. However, for electron p_{T} values above ∼80 GeV, as required here, this dependency can be neglected and the probability was found to be [57]:

$$p(e \to \gamma) = 0.006 \pm 0.0025,$$

where the uncertainty is mainly due to statistics.

The $Z \to ee$ control sample, on which the photon fake-rate $p(e \to \gamma)$ is determined, is affected by ISR and FSR in a similar way as the $t\bar{t}$ and W background with at least one electron in the final state. Therefore, the two background contributions from photon-fakes ($e \to \gamma$) and from ISR/FSR photons can be modelled simultaneously by the electron control sample weighted according to the measurement of $p(e \to \gamma)$. ISR and FSR photons originating from $t\bar{t}$ or W events with no electron in the final state are not covered by this background estimation because of the requirement of at least one electron in the photon-fake rate measurement. This additional background contribution is taken directly from simulation as discussed in more detail in Sec. 5.2.3.

5.2.2.1 Closure Test

In Fig. 5.10 the electron control sample, weighted with $p(e \to \gamma)$, is shown and compared to the direct simulation. The corresponding event yields in three different signal regions are shown in Table 5.2. For the simulation only events with

at least one generator electron passing the signal selection with one reconstructed tight photon are considered. The method closes well within the uncertainties.

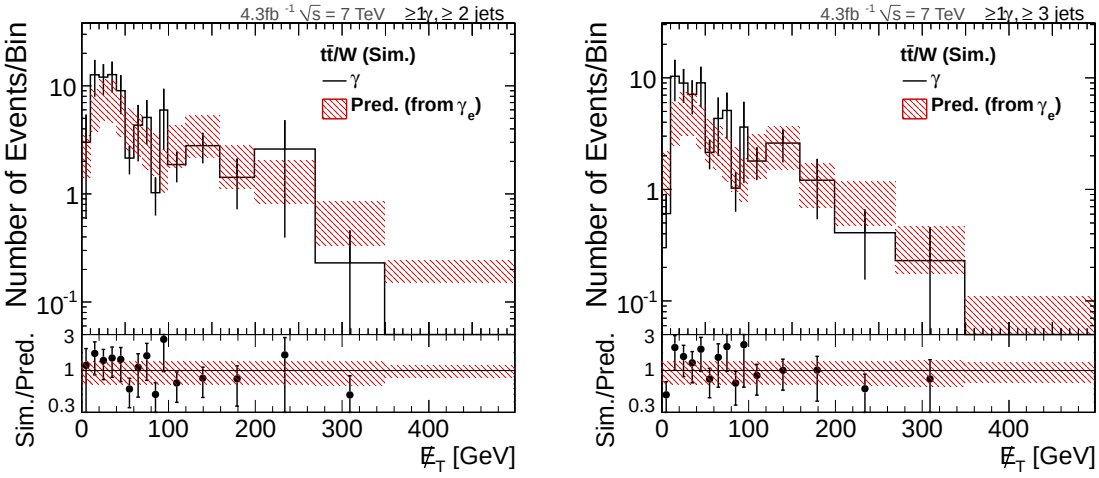

(a) (b)

Figure 5.10: Simulated $t\bar{t}$ and W background: $\not{E}_{\mathrm{T}}$ distribution of the selected events in the electron control sample after reweighting (hatched). The prediction is compared to the direct simulation in events with (a) ≥2 jets and (b) ≥3 jets.

5.2.2.2 Prediction for Data

The method to estimate the electroweak background has been shown to work on simulation and is now applied on the data sample. The obtained estimation is listed in Table 5.2. The $\not{E}_{\mathrm{T}}$ distribution of the electron control sample before and after the reweighting are shown in App. A.7. The $e \to \gamma$ background is significantly smaller compared to the γ/QCD background estimated in the previous section.

Table 5.2: Expected event yields of the $e \to \gamma$ estimation method for three different signal regions ($\not{E}_{\mathrm{T}} > 100/200/350$ GeV). The event yields correspond to 4.32 fb^{-1}.

EWK	$MET \geq 100$ GeV			$MET \geq 200$ GeV			$MET \geq 350$ GeV		
$\geq$1 photon, $\geq$2 jets		(stat)	(sys)		(stat)	(sys)		(stat)	(sys)
Estimate from data	17	$\pm$0.3	$^{+7.2}_{-7.2}$	3.5	$\pm$0.2	$^{+1.5}_{-1.5}$	0.4	$\pm$0.1	$^{+0.2}_{-0.2}$
Estimate from simulation	11	$\pm$0.3	$^{+4.6}_{-4.6}$	2.2	$\pm$0.2	$^{+0.9}_{-0.9}$	0.2	$\pm$0.1	$^{+0.1}_{-0.1}$
Direct simulation	8.9	$\pm$2.6		2.8	$\pm$2.2		≤ 0.01	$\pm \leq 0.01$	
$\geq$1 photon, $\geq$3 jets		(stat)	(sys)		(stat)	(sys)		(stat)	(sys)
Estimate from data	12	$\pm$0.3	$^{+4.9}_{-4.9}$	2.2	$\pm$0.1	$^{+0.9}_{-0.9}$	0.3	$\pm$0.04	$^{+0.1}_{-0.1}$
Estimate from simulation	7.2	$\pm$0.2	$^{+3.0}_{-3.0}$	1.2	$\pm$0.1	$^{+0.5}_{-0.5}$	0.1	$\pm$0.03	$^{+0.04}_{-0.04}$
Direct simulation	6.2	$\pm$1.3		0.6	$\pm$0.3		≤ 0.01	$\pm \leq 0.01$	

5.2.3 Further Backgrounds

Besides the discussed backgrounds appearing due to jets or electrons being misidentified as photons, additional backgrounds can occur due to initial state and final state radiation (ISR/FSR) of photons. ISR and FSR in events with electrons in the final state are already covered by the data driven electroweak background prediction as discussed in the previous section. As the remaining contributions are small and difficult to derive from data, these backgrounds are taken directly from the simulation with a systematic uncertainty of 100%.

For $t\bar{t}$ events the contribution due to ISR/FSR is determined by taking all events from the MC simulated sample, which pass the selection and have a generator photon matched to the selected tight photon. For events with W and Z bosons a dedicated sample is used as defined in App. A.4. For both contributions events with generator electrons are rejected. The used MC samples are both generated with MadGraph [80] on parton level, while the development of the fully hadronised event, including initial and final state parton showers, is done with pythia [65]. The resulting contributions after the final selection are summarised in Table 5.3. The dominant contribution is coming from $t\bar{t}$ or W/Z events with one or more neutrinos in the final state, while events where the W/Z bosons decay hadronically usually do not pass the $\not{E}_{\mathrm{T}}$ requirement.

Table 5.3: Expected event yields due to ISR/FSR for three different signal regions ($\not{E}_{\mathrm{T}} > 100/200/350$ GeV).

ISR/FSR (Sim.)	$MET \geq 100$ GeV			$MET \geq 200$ GeV			$MET \geq 350$ GeV		
$\geq$1 photon, $\geq$2 jets		(stat)	(sys)		(stat)	(sys)		(stat)	(sys)
W/Z	28	$\pm$3.2	$^{+28}_{-28}$	10	$\pm$2.0	$^{+10}_{-10}$	1.6	$\pm$0.8	$^{+1.6}_{-1.6}$
$t\bar{t}$	3.8	$\pm$0.9	$^{+3.8}_{-3.8}$	0.8	$\pm$0.4	$^{+0.8}_{-0.8}$	≤ 0.01	$\pm \leq 0.01$	$^{+\leq 0.01}_{-\leq 0.01}$
$\geq$1 photon, $\geq$3 jets		(stat)	(sys)		(stat)	(sys)		(stat)	(sys)
W/Z +Jet	14	$\pm$2.3	$^{+14}_{-14}$	6.3	$\pm$1.5	$^{+6.3}_{-6.3}$	0.7	$\pm$0.5	$^{+0.7}_{-0.7}$
$t\bar{t}$	3.4	$\pm$0.8	$^{+3.4}_{-3.4}$	0.6	$\pm$0.3	$^{+0.6}_{-0.6}$	≤ 0.01	$\pm \leq 0.01$	$^{+\leq 0.01}_{-\leq 0.01}$

5.3 Results

The combined background prediction, the observed data and two exemplary GGM benchmark signal samples are shown in Fig. 5.11 before the final selection on $\not\!\!E_{\mathrm{T}}$. The data is in good agreement with the standard model expectation for the whole $\not\!\!E_{\mathrm{T}}$ range. The included systematic uncertainties for each of the backgrounds are summarised in Table 5.6.

To define the final signal region different cuts on the $\not\!\!E_{\mathrm{T}}$ variable have been studied with respect to the expected event yields and the expected sensitivity of this analysis. The expected and observed event yields for three signal regions ($\not\!\!E_{\mathrm{T}} > 100/200/350$ GeV) are summarised in Table 5.4(5.5) for events with $\geq$2 ($\geq$3) jets. The resulting event yields in dependence of possible cuts on $\not\!\!E_{\mathrm{T}}$ are compared to the expectation for the two example GGM benchmark points in Fig. 5.12.

For the same exemplary signal points the $S/\sqrt{S+\sigma_B^2}$ and $S/\sqrt{S+B}$ values have been compared for different $\not\!\!E_{\mathrm{T}}$ cuts. Here, S is the expected number of selected signal events, B the number of estimated background events and σ_B the uncertainty on the background estimation. The resulting distributions are shown in Fig. 5.13.

The events in the signal region ($\not\!\!E_{\mathrm{T}} \geq 300$ GeV) have been scanned in order to identify possible contributions from one of the known sources of high artificial $\not\!\!E_{\mathrm{T}}$ as outlined in Sec. 4.4. In addition the three available $\not\!\!E_{\mathrm{T}}$ algorithms have been compared to identify possible problems in the event reconstruction. In both, signal and selected control samples, no obvious indication of fake energies was found. In a few events possible signs for punch-through were found, also a couple of events seem to be slightly affected by non-functioning regions in the ECAL. However, only very small fraction of events is affected and the events are distributed over all control samples. Therefore possible effects on the high $\not\!\!E_{\mathrm{T}}$ tail are expected to be negligible and the events are not removed from the final selection. More details about these events are summarised in App. A.8.4.

The calculation of exclusion limits and the interpretation in the GGM parameter space for a bino- and a wino-like NLSP scenario are discussed in the following section.

Table 5.4: Resulting event yields for the ≥1 photon and ≥2 jet selection for three different signal regions ($\not{E}_{\mathrm{T}} >$ 100/200/350 GeV).

$4.32\,\mathrm{fb}^{-1}$	$MET \geq 100$ GeV			$MET \geq 200$ GeV			$MET \geq 350$ GeV		
≥1 photon, ≥2 jets		(stat)	(sys)		(stat)	(sys)		(stat)	(sys)
QCD (from data)	608	±47	$^{+54}_{-54}$	91	±16	$^{+9.9}_{-9.9}$	6.8	±4.1	$^{+0.8}_{-0.8}$
$e \to \gamma$ (from data)	17	±0.3	$^{+7.2}_{-7.2}$	3.5	±0.2	$^{+1.5}_{-1.5}$	0.4	±0.1	$^{+0.2}_{-0.2}$
$FSR/ISR(W,Z)$	28	±3.2	$^{+28}_{-28}$	10	±2.0	$^{+10}_{-10}$	1.6	±0.8	$^{+1.6}_{-1.6}$
$FSR/ISR(t\bar{t})$	3.8	±0.9	$^{+3.8}_{-3.8}$	0.8	±0.4	$^{+0.8}_{-0.8}$	≤ 0.01	$\pm \leq 0.01$	$^{+\leq 0.01}_{-\leq 0.01}$
total SM estimation	656	±47	$^{+93}_{-93}$	106	±17	$^{+23}_{-23}$	8.7	±4.2	$^{+2.5}_{-2.5}$
Data	615			63			4		

Table 5.5: Resulting event yields for the ≥1 photon and ≥3 jet selection for three different signal regions ($\not{E}_{\mathrm{T}} >$ 100/200/350 GeV).

$4.32\,\mathrm{fb}^{-1}$	$MET \geq 100$ GeV			$MET \geq 200$ GeV			$MET \geq 350$ GeV		
≥1 photon, ≥3 jets		(stat)	(sys)		(stat)	(sys)		(stat)	(sys)
QCD (from data)	361	±40	$^{+33}_{-33}$	44	±10	$^{+4.0}_{-4.0}$	3.1	±3.1	$^{+0.5}_{-0.5}$
$e \to \gamma$ (from data)	12	±0.3	$^{+4.9}_{-4.9}$	2.2	±0.1	$^{+0.9}_{-0.9}$	0.3	±0.04	$^{+0.1}_{-0.1}$
$FSR/ISR(W,Z)$	14	±2.3	$^{+14}_{-14}$	6.3	±1.5	$^{+6.3}_{-6.3}$	0.7	±0.5	$^{+0.7}_{-0.7}$
$FSR/ISR(t\bar{t})$	3.4	±0.8	$^{+3.4}_{-3.4}$	0.6	±0.3	$^{+0.6}_{-0.6}$	≤ 0.01	$\pm \leq 0.01$	$^{+\leq 0.01}_{-\leq 0.01}$
total SM estimation	390	±40	$^{+55}_{-55}$	53	±11	$^{+12}_{-12}$	4.0	±3.1	$^{+1.3}_{-1.3}$
Data	375			41			3		

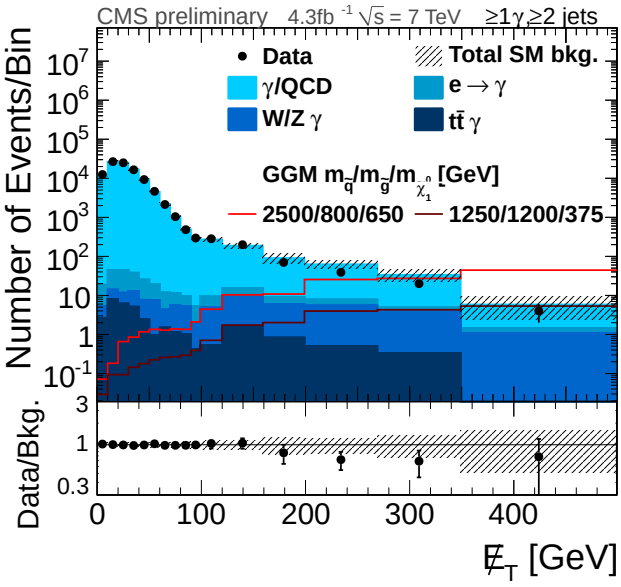

(a)

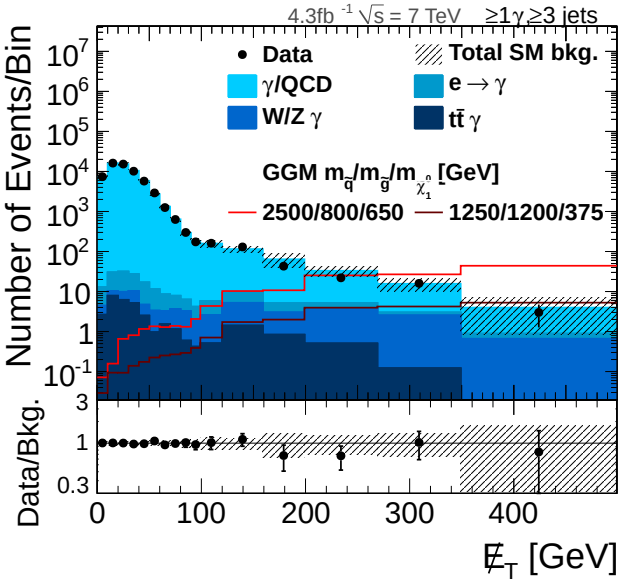

(b)

Figure 5.11: Total standard model background prediction, as discussed above, compared to the selected number of events in 4.32 $\mathrm{fb}^{-1}$and two exemplary GGM signal benchmark points ($m_{\tilde{q}}$[GeV]/ $m_{\tilde{g}}$[GeV]/ $m_{\tilde{\chi}_1^0}$[GeV]) before the final cut on $\not\!\!E_{\mathrm{T}}$ for the (a) $\geq$2 and (b) $\geq$3 jet selection. The hatched band represents the combined uncertainty on the total Standard Model background.

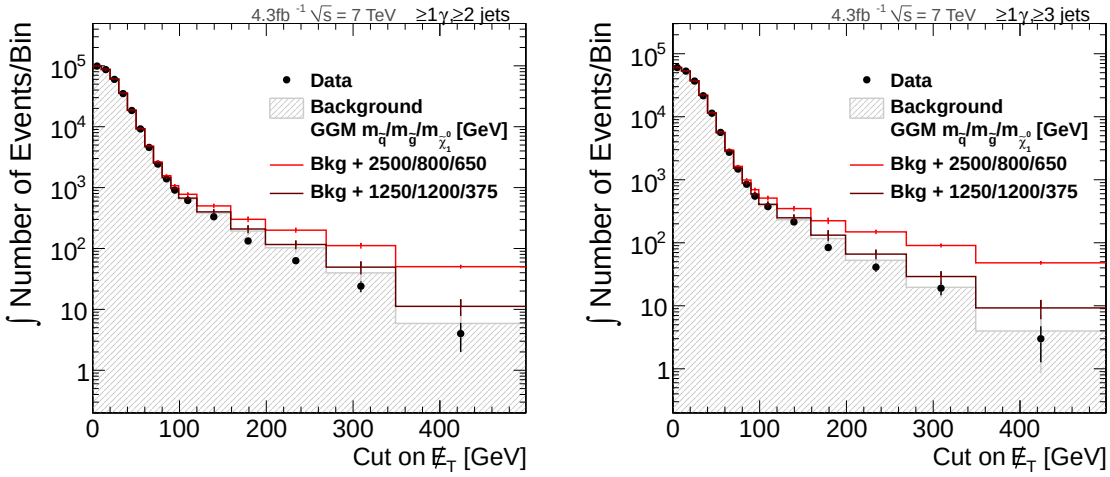

(a) (b)

Figure 5.12: Event yield integral in dependence of possible cuts on $\not{E}_{\mathrm{T}}$ in events with (a) ≥2 and (b) ≥3 jets.

Table 5.6: Summary of considered systematic uncertainties on total standard model background.

Background	source of syst. errors	uncertainty on total background
≥1 photon, ≥2 jets		
γ/QCD	Statistical weight uncertainty	±5.9%
	Extrapol. from $\not{E}_{\mathrm{T}}$<100 GeV to whole spectrum	±2.9%
EWK ($e \to \gamma_e$)	fake rate uncertainty	±1.4%
FSR/ISR		
$W \to \mu/\tau\nu$,$Z \to \nu\nu$	NLO uncertainties, etc.	±9.9%
$t\bar{t} \to \mu/\tau\nu + X$	NLO uncertainties, etc.	±0.8%
≥1 photon, ≥3 jets		
γ/QCD	Statistical weight uncertainty	±9.0%
	Extrapol. from $\not{E}_{\mathrm{T}}$<100 GeV to whole spectrum	±4.5%
EWK ($e \to \gamma_e$)	fake rate uncertainty	±1.7%
FSR/ISR		
$W \to \mu/\tau\nu$,$Z \to \nu\nu$	NLO uncertainties, etc.	±11.9%
$t\bar{t} \to \mu/\tau\nu + X$	NLO uncertainties, etc.	±1.2%

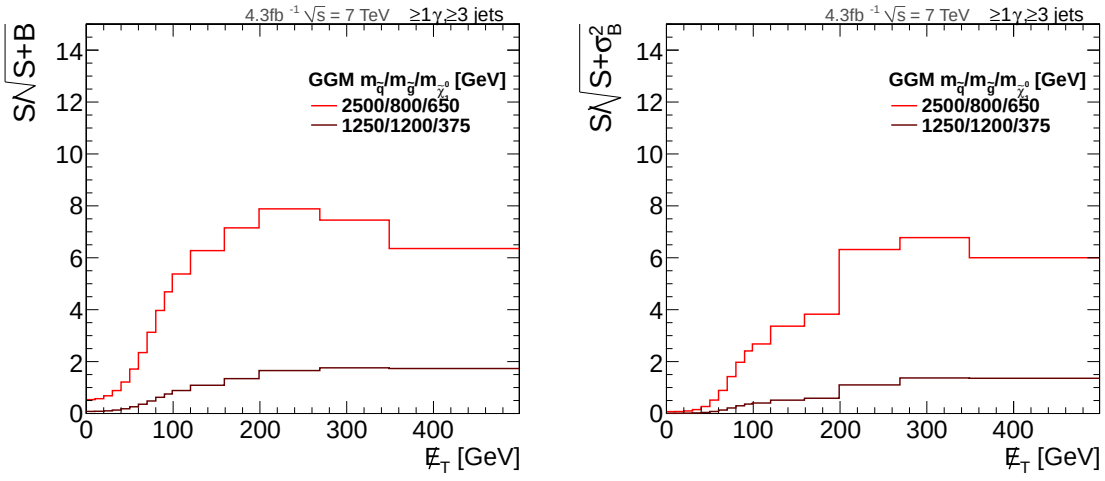

(a) (b)

Figure 5.13: (a) $S/\sqrt{S+B}$ and (b) $S/\sqrt{S+\sigma_B^2}$ values for two exemplary GMSB signal points ($m_{\tilde{q}}$[GeV]/ $m_{\tilde{g}}$[GeV]/ $m_{\tilde{\chi}_1^0}$[GeV]). S is the expected number of selected signal events, B the number of estimated background events and σ_B the uncertainty on the background estimation. The expected background contribution from signal is not considered.

5.4 Interpretation

In order to maintain a good signal efficiency the final signal region for the calculation of exclusion limits is defined with a relatively loose selection criteria requiring $\not{E}_{\mathrm{T}} \geq$100 GeV. To still achieve a good sensitivity, the limits are calculated in 6 distinct bins with the following $\not{E}_{\mathrm{T}}$ ranges [GeV]:[100,120), [120,160), [160,200), [200,270), [270,350) and [350,∞).

The exclusion limits are CLs limits calculated with a fully frequentist approach ('LHC style'), the software is based on the RooStats toolkit [81]. An end-user interface provided by the CMS Higgs group [82] is used.

As discussed above[1] the exclusion limits have been calculated for two different neutralino eigenstates: one assuming a bino-like neutralino, the other a wino-like neutralino. The interpretation is done in the squark-gluino mass plane for both neutralino models. In addition the bino-like neutralino scenario is interpreted in the gluino-neutralino mass plane.

The number of GGM events expected to pass the signal selection (S_{GGM}) is obtained in each of the six signal bins, as well as the expected contribution from GGM simulated events to the data driven Standard Model background estimation methods (B_{GGM}). To avoid effects from GGM signal contamination in the limit calculation the acceptance times efficiency (A$\times\epsilon$) for each of the GGM parameter points is adjusted by the background event yield from GGM signal:

$$\mathrm{A} \times \epsilon = \frac{S_{\mathrm{GGM}} - B_{\mathrm{GGM}}}{N_{\mathrm{GGM}}}, \tag{5.2}$$

where N_{GGM} is the total number of GGM events expected at this parameter point[2]. The signal contamination, i.e. the ratio of expected Standard Model background events estimated from GGM signal (B_{GGM}) compared to the number of expected signal events (S_{GGM}), is shown in the studied GGM parameter planes in App. A.9.1.

[1] See Sec. 2.2.2.1 for the details of the assumed GGM parameter space

[2] Thus the acceptance times efficiency includes the branching ratio into photons.

5.4.1 Systematic Uncertainties

To account for possible differences between data and simulation the obtained acceptance is scaled by $\frac{\epsilon_e^{data}}{\epsilon_e^{MC}}$, the ratio of photon efficiencies in data and MC simulation[1], for each signal sample point.

In addition, besides the statistical error of the simulation, the following systematic uncertainties on the signal acceptance are considered within the limit setting framework as nuisance parameters:

- Jet energy scale: 2%
- $\frac{\epsilon_e^{data}}{\epsilon_e^{MC}}$: 4%
- Luminosity: 4.5%
- PDF uncertainty on the acceptance (depending on the GGM parameter point):∼0.03-20%[2]

These uncertainties are propagated within the limit setting framework and displayed as experimental error band around the expected limit in the following.

To estimate the impact from theoretical uncertainties on the cross section at each point the renormalisation scale and the PDF uncertainty on the cross section are combined. The NLO cross section is then scaled up (down) by this uncertainty to obtain the corresponding $\pm 1\sigma$ theoretical error band.

5.4.2 Sample Limit Calculation

As an example, the limit calculation is discussed in more detail for a GGM point which turns out to be excluded by the measurement. For this example the squark mass is chosen to be 720 GeV, the gluino mass 800 GeV, and the neutralino $\tilde{\chi}_1^0$ mass to be 375 GeV. The neutralino is assumed to be a bino mass eigenstate. After all selection criteria are applied, the total acceptance times efficiency in events with $\not{E}_{\mathrm{T}} \geq 100$ GeV is found to be $75 \pm 19\%$ for the ≥ 2 jet selection.

[1] See Sec. 3.4.2

[2] See App. A.1.2 for the distribution of the uncertainties in the squark-gluino (gluino-neutralino) mass plane.

The NLO cross section is $0.51^{+0.07}_{-0.08}$ ± 0.06 pb. The first uncertainty corresponds to the renormalisation scale uncertainty, the second to the PDF uncertainty on the cross section. This implies, for a luminosity of $4.32 \pm 0.19\,\mathrm{fb}^{-1}$, an expected number of signal events after all cuts of 1641 ± 316. The expected background contribution is 309 events, which is subtracted from the expected signal events for the limit calculation. The corresponding numbers for each of the six exclusive bins used for the limit calculation are summarised in Tab. 5.7 together with the obtained 95% cross-section limit for each bin.

Table 5.7: Observed and expected event yields, acceptance × efficiency (A × ϵ) and obtained limits for each exclusive signal bin for a sample GGM point ($m_{\tilde{\chi}_1^0}$ = 375 GeV (bino-like), $m_{\tilde{g}} = 800\,\mathrm{GeV}$, $m_{\tilde{q}} = 720\,\mathrm{GeV}$) and the ≥2 jet selection. S_{Data} is the number of events in data passing the signal selection, B_{SM} is the expected contribution from Standard Model backgrounds. As introduced above, S_{GGM} is the number of simulated GGM events passing the signal selection and B_{GGM} the expected contribution from GGM events to the data driven estimation of Standard Model backgrounds. The observed and expected 95%CL limits on the total signal-cross section and on the number of signal events passing the selection are given.

$\not{E}_{\mathrm{T}}$ [GeV]	100-120	120-160	160-200	200-270	270-350	≥350
A × ϵ [%]	3.4	8.4	9.2	17	16	12
Observed event yields						
S_{Data}	283	199	70	39	20	4
Expected event yields						
B_{SM}	272±38	187±29	91±25	63±15	34±11	5.8±3.7
S_{GGM}	76±7	184±14	201±15	381±26	356±25	268±19
B_{GGM}	15	31	40	61	60	55
95% CL Limit						
Observed [pb]	0.69	0.22	0.086	0.02	0.016	0.014
S_{GGM}	103	81	34	15	11	7
Expected [pb]	0.63	0.19	0.1	0.034	0.028	0.013
S_{GGM}	93	69	39	26	19	7

The combination of the individual bins leads to an upper limit at the 95% CL

for a GGM cross section of 0.008 pb for the assumption of a Gaussian background uncertainty distribution, the combined expected upper limit is 0.013 ± 0.004 pb.

The renormalisation scale uncertainties and the PDF uncertainty on the cross section lead to a $\pm 1\sigma$ range of the NLO cross section between 0.61 pb and 0.42 pb, which is above the observed cross-section limit. Therefore this particular point can be excluded.

5.4.3 Results

The exclusion limits have been calculated for both jet selection scenarios ($\geq$2/3 jets). For all considered GGM benchmark scenarios both selections show very similar results. Therefore in the following only the results of the more inclusive $\geq$2 jet selection are discussed, while the results from the $\geq$3 jet selection are shown and compared to the $\geq$2 jet selection in App. A.9.2. A combination of both selections is, in principle, possible. With the current selection the correlation between the selections is very large and no significant improvement is expected. However, splitting the events in several disjunct jet multiplicity bins could improve the results significantly.

The squark-gluino mass plane reaches for both masses from 400 GeV to 2000 GeV, while the neutralino mass is set to 375 GeV for both neutralino scenarios. The obtained acceptance times efficiency is shown for both neutralino modes in Fig. 5.14. For comparison also the acceptance times efficiency observed in the highest $\not{E}_{\mathrm{T}}$ bin is shown in Fig 5.14. As outlined in Sec. 2.2.2.1, for the wino-like neutralino much less photons than for the bino-like case are expected. Therefore, the lower acceptance for the wino-like neutralino is expected. The resulting limits are shown in Fig. 5.15.

The observed and expected limits[1] for four exclusive signal bins are shown in Fig. 5.16 for both types of neutralinos. As already expected from the signal to background ratio of the studied sample points (Fig. 5.13) the sensitivity of each bin increases with the $\not{E}_{\mathrm{T}}$ cut.

[1] To reduce the need of computing resources in the limit calculation the limits shown here for the individual $\not{E}_{\mathrm{T}}$ bins are the 'asymptotic' CLs limits [82]. The difference between asymptotic and fully frequentist CLs limits has been studied at exemplary GGM points and was found to be very small.

For a bino-like scenario the resulting upper limit cross section is in the order of $0.01\,\mathrm{pb}^{-1}$with a typical acceptance of $\sim$ 79%. For the wino-like scenario the acceptance drops to $\sim$ 8%, leading to an upper limit cross section of $\sim 0.08\,\mathrm{pb}^{-1}$. This corresponds in both cases to $\sim$ 32 signal events. Thus squark masses up to $\sim$ 1040 (780) GeV and gluino masses up to $\sim$ 960 (730) GeV for the bino- (wino-) like neutralino scenario and a neutralino mass of 375 GeV can be excluded at 95% CL.

For the bino-like neutralino the exclusion limit has been studied also in the gluino-neutralino mass plane. Here the gluino mass ranges from 160 GeV to 2000 GeV, while the neutralino mass is in the range between 150 GeV and 1050 GeV. The obtained acceptance times efficiency is shown in Fig. 5.17, again in two versions, including all events with $\not{E}_{\mathrm{T}} \geq 100$ GeV and for the highest $\not{E}_{\mathrm{T}}$ bin only.

The resulting cross-section limits are shown in Fig. 5.18. The expected and observed limits obtained in each of the four highest $\not{E}_{\mathrm{T}}$ bins separately are shown in Fig. 5.19. Again, in general, the sensitivity of each bin is increasing with higher $\not{E}_{\mathrm{T}}$. But for lower neutralino masses the lower $\not{E}_{\mathrm{T}}$ ranges also contribute significantly to the resulting combined limit.

The observed combined upper cross section limit is in the order of 0.02 to $0.01\,\mathrm{pb}^{-1}$depending on the neutralino mass. The typical acceptance ranges between $\sim$ 56% and $\sim$ 78%, which corresponds to $\sim$ 53 - 37 signal events. As a result bino-like neutralinos with masses up to $\sim$ 800 GeV can be excluded if the gluino mass is below $\sim$ 800 GeV. The bound on the gluino mass ranges from 800 to 960 GeV for neutralino masses below $\sim$ 800 GeV.

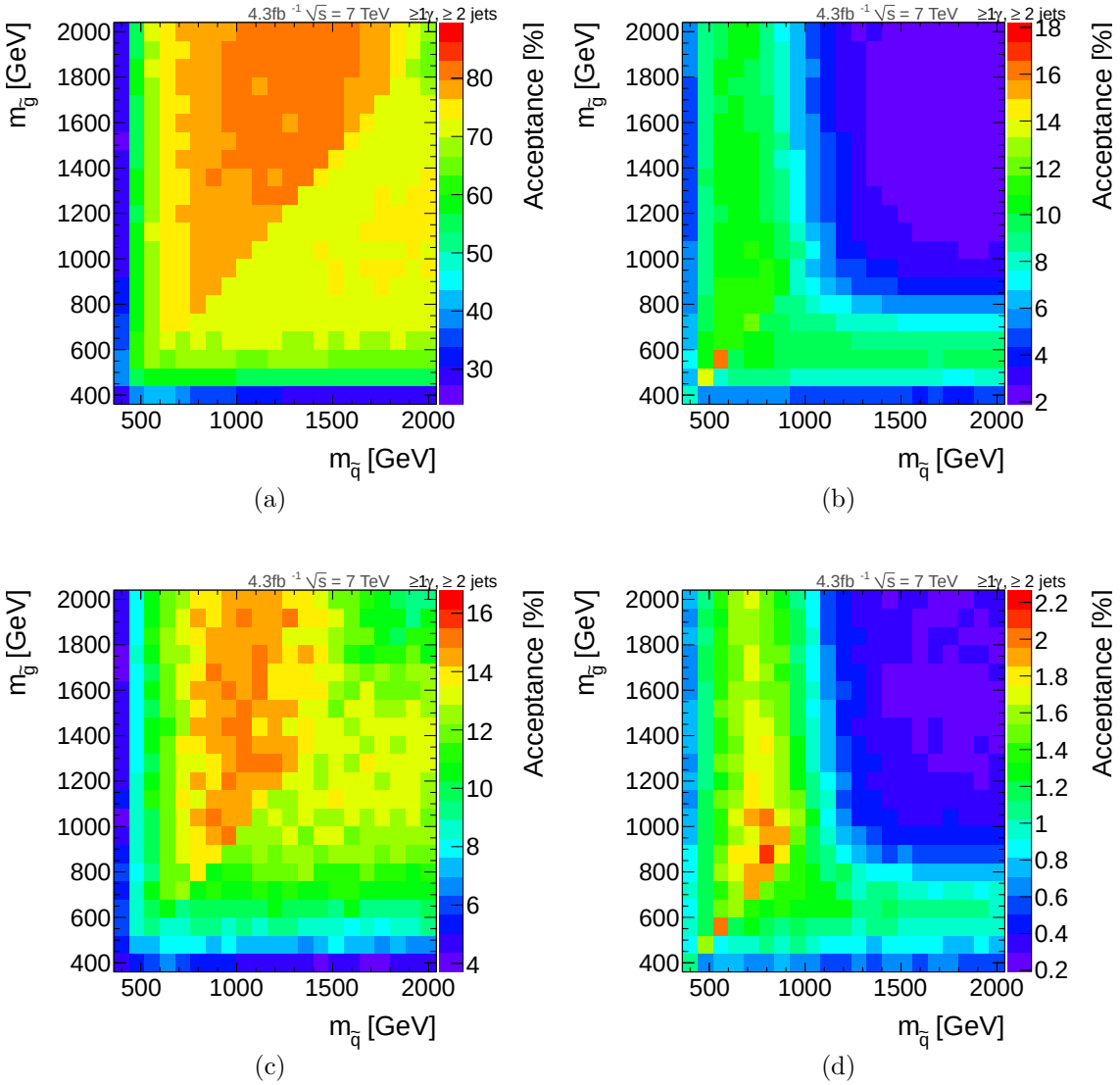

Figure 5.14: Acceptance times efficiency in percent for a (a) bino- and (b) wino-like neutralino for the ≥2 jet selection in the squark-gluino mass plane. For the same jet selection the acceptance times efficiency in the highest $\not{E}_{\mathrm{T}}$ bin is shown for a (c) bino- and (d) wino- like neutralino.

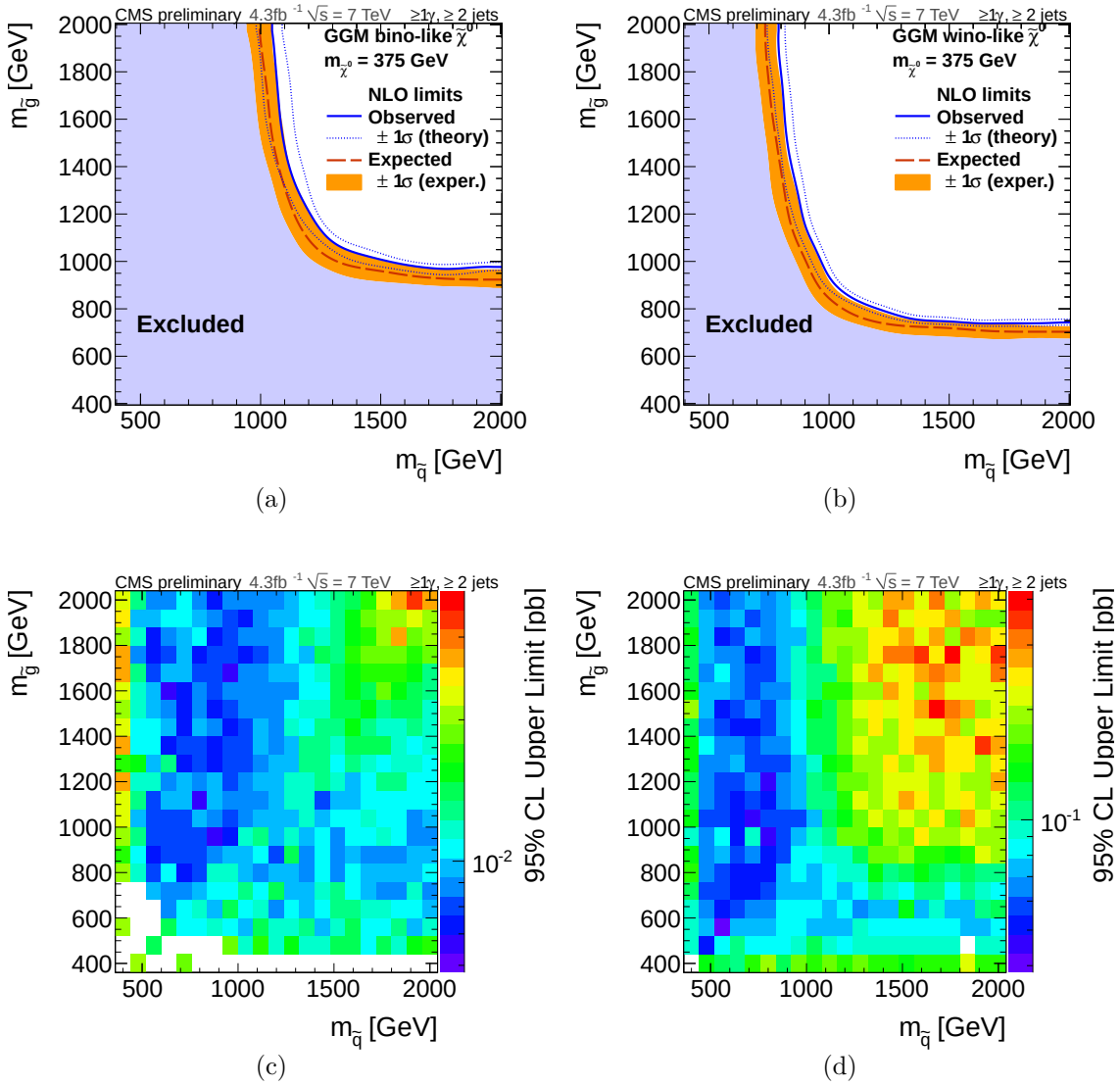

Figure 5.15: 95% CL exclusion limits in the squark-gluino mass plane for a (a) bino- and (b) wino- like neutralino and observed cross-section limits for a (c) bino- and (d) wino- like neutralino. The shaded uncertainty band around the exclusion contours corresponds to the experimental uncertainties on the acceptance. The impact of NLO renormalisation and PDF uncertainties on the signal cross section is visualised with the dotted lines.

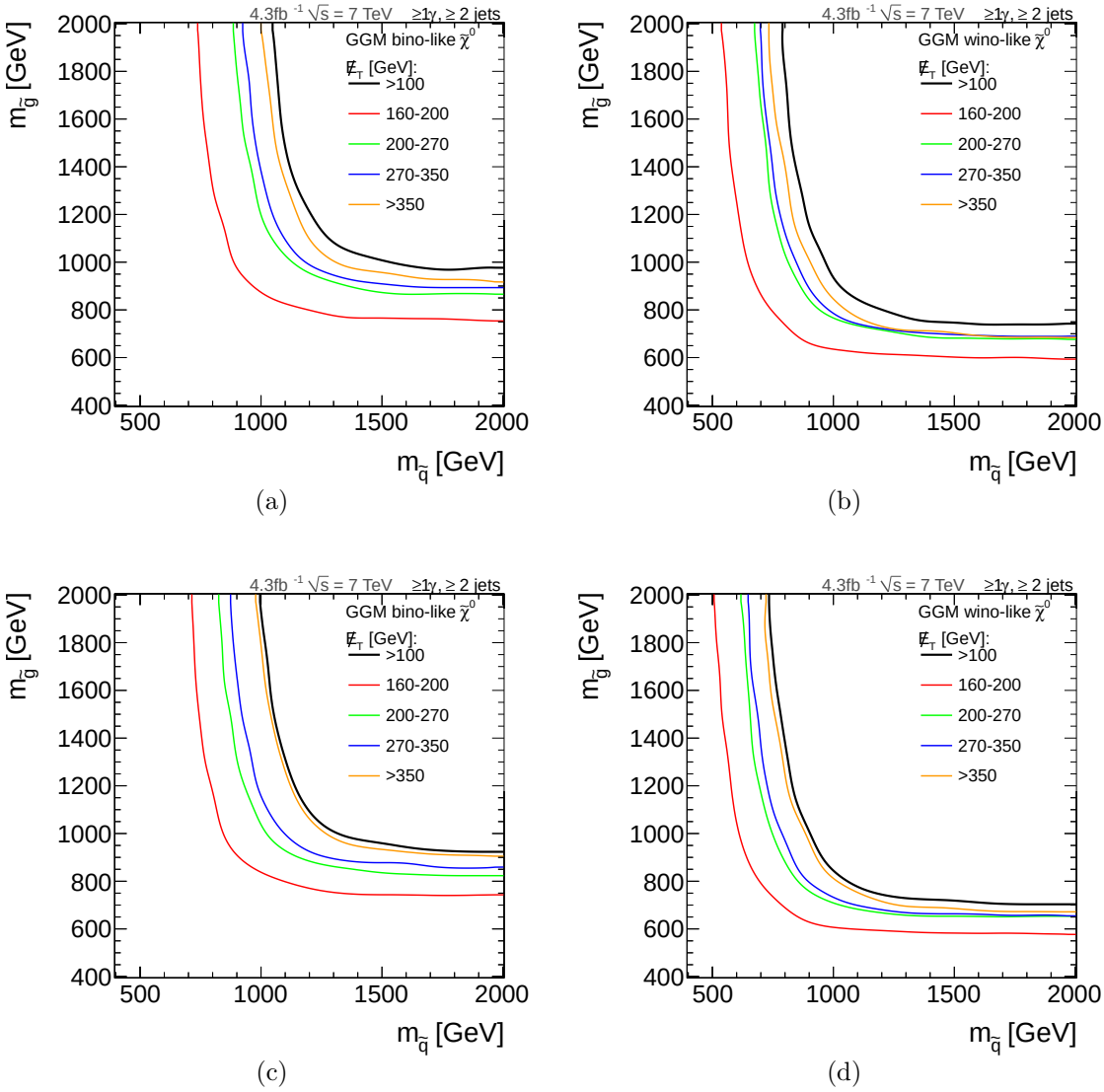

Figure 5.16: (a,b) Observed and (c,d) expected 95% CL exclusion limits in several distinct $\not{E}_{\mathrm{T}}$ bins for a (a,c) bino- and (b,d) wino- like neutralino in the squark-gluino mass plane.

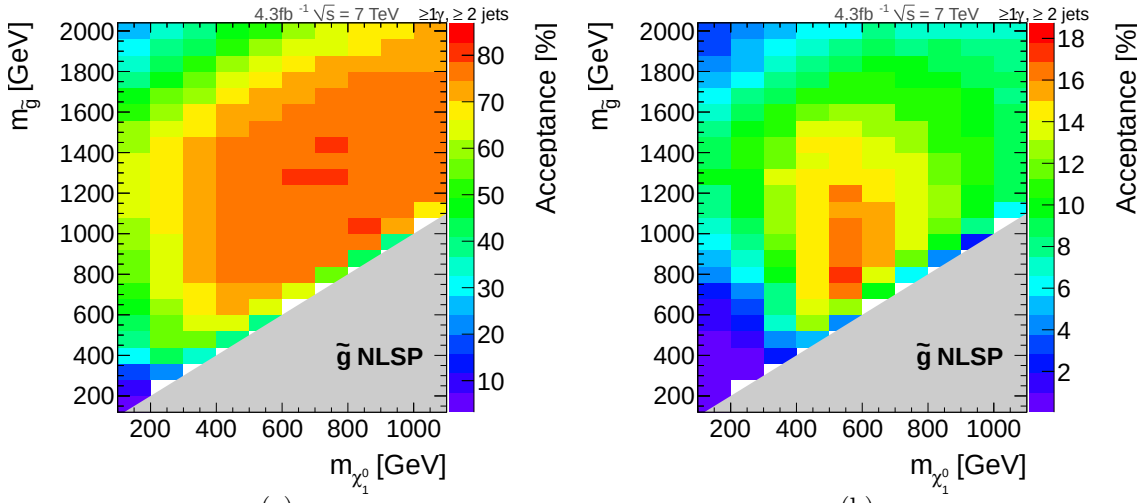

Figure 5.17: Acceptance times efficiency in percent for (a) all events in the signal region ($\not{E}_{\mathrm{T}} \geq 100$ GeV) and (b) in the highest $\not{E}_{\mathrm{T}}$ bin in the gluino-neutralino mass plane. The neutralino is bino-like and the ≥2 jet selection is applied.

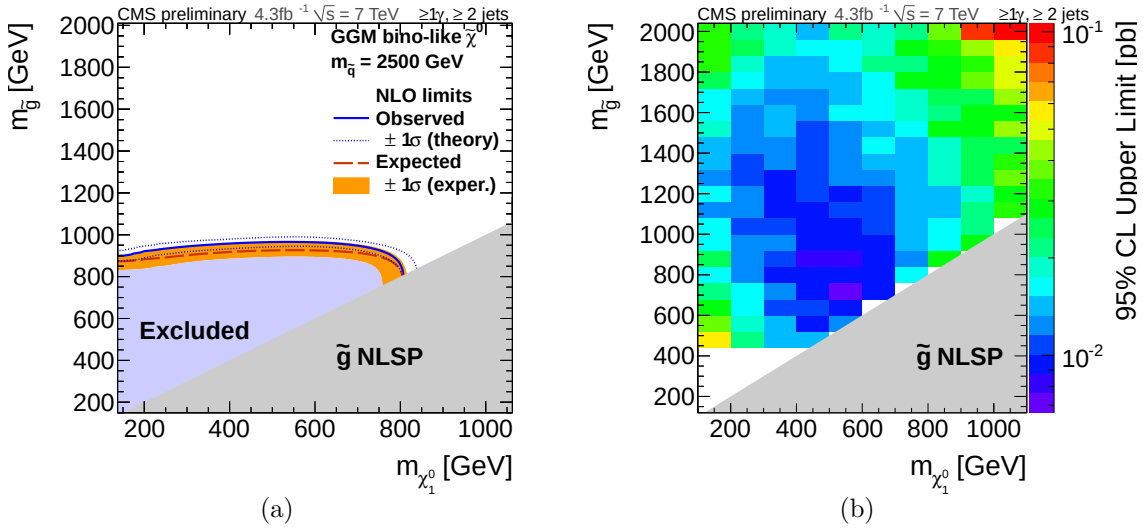

Figure 5.18: (a) 95% CL exclusion limits and (b) observed cross section limits for a bino-like neutralino in the gluino-neutralino mass plane. The shaded uncertainty band around the exclusion contours corresponds to the experimental uncertainties on the acceptance. The impact of NLO renormalisation and PDF uncertainties on the signal cross section is visualised with the dotted lines.

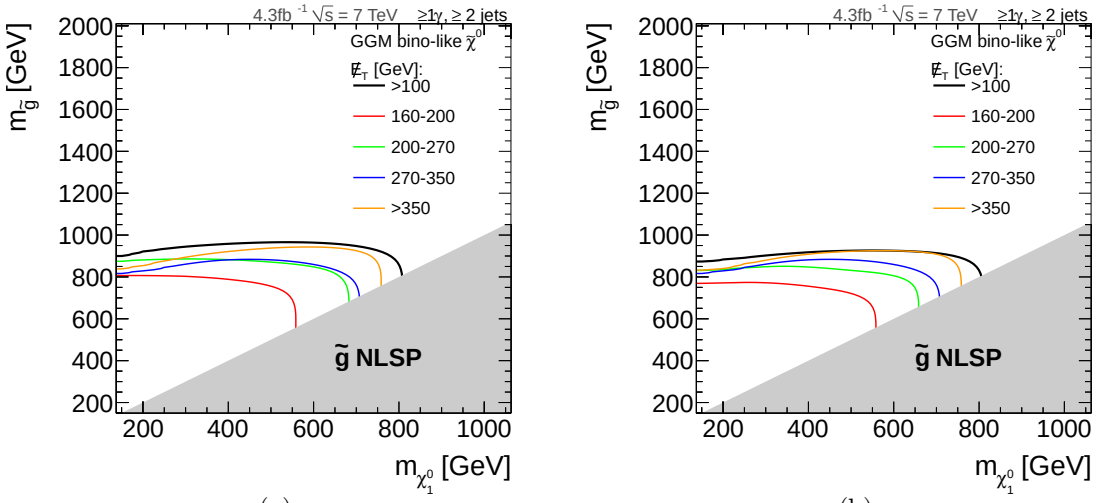

Figure 5.19: (a) Observed and (b) expected 95% CL exclusion limits in four exclusive $\not{E}_{\mathrm{T}}$ bins for a bino-like neutralino in the gluino-neutralino mass plane.

5. SEARCH FOR SUPERSYMMETRY IN EVENTS WITH PHOTONS AND $\not{E}_{\mathrm{T}}$

6

Conclusions

6.1 Summary

In this thesis a search for gauge mediated supersymmetry in $4.32\,\mathrm{fb}^{-1}$ of data recorded in 2011 with the CMS detector has been presented. The search was performed in final states with at least one photon, jets and missing transverse energy. The selected data is in good agreement with the Standard Model background expectation, exclusion limits at the 95% CL have been calculated and interpreted in the GGM parameter space.

As a key ingredient for the presented search for supersymmetry the missing transverse energy has been studied in detail. A data driven strategy to derive the correction scale for unclustered energy deposits, the type-II correction, has been presented. The resulting scale and resolution have been studied in different event topologies.

Measuring the Missing Transverse Energy

The type-II correction scale has been measured in $Z \to ee$ data using 36 pb^{-1} of the 2010 7 TeV dataset for Calo $\not\!\!E_{\mathrm{T}}$ and PF $\not\!\!E_{\mathrm{T}}$ utilising the transverse momentum balance between the Z boson and the hadronic recoil. Both results were found to be in good agreement with the MC expectations. The obtained data and MC driven type-II scales are summarized in Table 6.1.

	type-I jet p_T	MC	Data ($36\,pb^{-1}$)
PF $\not\!\!E_T$	≥ 10 GeV	1.5±0.1	1.4±0.2
Calo $\not\!\!E_T$	≥ 20 GeV	A=2.0±0.7 B=1.3±0.5 C=0.1±0.1	A=2.3±0.4 B=1.9±1 C=0.2±0.2

Table 6.1: Data and MC driven type-II scale for PF $\not\!\!E_T$ and Calo $\not\!\!E_T$ (statistical errors only). For Calo $\not\!\!E_T$ the correction was fitted with a function of the form $A + B \cdot e^{-C \cdot x/GeV}$, where x is the average vector sum of the unclustered energy deposits. For PF $\not\!\!E_T$ the correction is described by a single constant parameter A.

The obtained correction scales were applied on $Z \to ee$ events with and without jets, validating the resulting $\not\!\!E_T$ scale after the different levels of corrections. In addition the performance was studied in dijet events. For both $\not\!\!E_T$ algorithms the type-II correction improves the scale of the $\not\!\!E_T$ in $Z \to ee$ as well as in dijet events, especially in the low $\not\!\!E_T$ region. For Calo $\not\!\!E_T$, where the effect of the correction is largest, the scale was adjusted within 1-2 GeV after the application of the corrections. This reduced the bias measured without correction by a factor of ∼3. Clear improvements were also visible for PF $\not\!\!E_T$, but here the needed corrections are much smaller. In dijet events the scale was measured to be adjusted within 2 GeV already before the application of the correction, which underlines the high capability of the particle-flow algorithm to reconstruct particles down to small transverse momenta. Good agreement between data and MC simulation was observed for both event samples. The resolution was studied in $Z \to ee$ events, showing that the adjustment of the unclustered energy leads to an improvement of the resolution, while the unavoidable upscaling of noise by the correction contradicts this effect and in some settings might slightly worsen the resulting resolution.

Two important causes of artificial high $\not\!\!E_T$ were discussed: punch-through of high energetic jets and contributions due to non-functioning detector regions. For both methods a basic strategy to identify possibly affected events has been presented: in case of punch-through the number of hits in the muon system behind a jet are utilised, while in case of non-functioning detector regions in the CMS

ECAL either the trigger primitive information or the energy deposited around a masked detector region can be used. The events with $\not\!\!E_{\mathrm{T}}$ above 300 GeV passing the signal selection of the SUSY search have been checked for possible signs of either of the discussed effects. In both, signal and selected control samples, no obvious indication of fake energy was found.

Search for Supersymmetry

For the final selection 615 events with at least one high energetic photon ($p_{\mathrm{T}} \geq$80 GeV), at least two jets ($p_{\mathrm{T}} \geq$30 GeV) and $\not\!\!E_{\mathrm{T}} \geq$ 100 GeV have been selected in 4.32 fb^{-1} of data. The expected main background from Standard Model processes (γ/QCD) and the already minor electroweak background($e \to \gamma$) have been estimated with two data driven methods. The much smaller Standard Model background expected due to initial or final state radiated photons has been estimated using MC simulation. The combined background expectation for all Standard Model backgrounds in the signal region was found to be $656 \pm 47^{+93}_{-93}$ events. No significant excess over the Standard Model expectation was observed. The results have been interpreted in different GGM scenarios with a bino- or wino-like neutralino. For this purpose the signal region has been divided into six distinct $\not\!\!E_{\mathrm{T}}$ bins, which have been combined for the calculation of exclusion limits. The observed upper limit on the cross section is in the order of 0.01(0.08) pb^{-1} for the studied GGM model with a bino- (wino-) like neutralino. Thus, squark masses up to $\sim$ 1040 (780) GeV and gluino masses up to $\sim$ 960 (730) GeV for the bino- (wino-) like neutralino scenario and a neutralino mass of 375 GeV can be excluded at 95% CL. For models with a bino-like neutralino the bound on the gluino mass ranges from 800 to 960 GeV for all neutralino masses below $\sim$ 800 GeV. For gluino masses below $\sim$ 800 GeV bino-like neutralinos with masses up to $\sim$ 800 GeV can be excluded. The resulting 95% CL limits are summarised in Table 6.2.

Previous limits from searches at the Tevatron [33; 34] have already clearly been superseeded by the 1 fb^{-1} result. The only direct search for a wino-like neutralino at the LHC, prior to this analysis, is the CMS single photon and lepton analysis [73], which was published with the first LHC data (35 pb^{-1}). The

results yield a clearly smaller maximum limit on squark and gluino masses, in the order of 450 GeV for neutralino masses above 250 GeV, than the results presented here. The results presented in this thesis set the most stringent limits on squark, gluino and neutralino masses for GGM models with a wino-like neutralino.

For a bino-like neutralino the latest result from the ATLAS collaboration [83] ($1.07\,\mathrm{fb}^{-1}$) sets a limit of 805 GeV on the gluino-mass, while this analysis reaches up to 960 GeV. However, the diphoton analyses from CMS and ATLAS are expected to reach a similar (or slightly higher) sensitivity than presented here, once they are updated to the full available dataset. Currently[1], the results presented in this thesis set the most stringent limits also on squark, gluino and neutralino masses for GGM models with a bino-like neutralino.

Table 6.2: Summary of obtained exclusion limits for the three GGM benchmark scenarios with a bino- and wino-like neutralino.

	Bino-like $\tilde{\chi}_1^0$		Wino-like $\tilde{\chi}_1^0$	Constraint
fixed mass	$m_{\tilde{\chi}_1^0}$	$m_{\tilde{q}}$	$m_{\tilde{\chi}_1^0}$	
Scan range $m_{\tilde{g}}$ [GeV]	400-2000	400-2000	400-2000	
Scan range $m_{\tilde{q}}$ [GeV]	400-2000	2500	400-2000	
Scan range $m_{\tilde{\chi}_1^0}$ [GeV]	375	150-1050	375	
$A \times \epsilon$ [%]	~ 79	$\sim 56-78$	~ 8	
95% CL Upper Limit				
Observed [pb]	~ 0.01	$\sim 0.02-0.01$	~ 0.08	
$m_{\tilde{g}}$ [GeV]	960	-	730	$m_{\tilde{\chi}_1^0} = 375$ GeV
$m_{\tilde{q}}$ [GeV]	1040	-	780	$m_{\tilde{\chi}_1^0} = 375$ GeV
$m_{\tilde{g}}$ [GeV]	-	800-960	-	$m_{\tilde{\chi}_1^0} \leq 800$ GeV
$m_{\tilde{\chi}_1^0}$ [GeV]	-	800	-	$M_{\tilde{g}} \leq 800$ GeV

[1] Recently, during the review process of this thesis, first results from the CMS diphoton analysis have been made public [84] setting an upper limit on the gluino mass in the order of 1000 GeV. As expected this slightly extends the reach of this analysis in case of a bino-like neutralino.

6.2 Outlook

Measuring the Missing Transverse Energy

Due to the increasing instantaneous luminosity during 2010 and especially 2011 the pile up conditions of the recorded data have changed rapidly. Pile up activity leads to additional energy deposits in the detector. To avoid an upscaling of these energy deposits by the type-II $\not\!\!E_{\mathrm{T}}$ corrections, the type-II scale and the calculation of the unclustered energy in each event have to be adapted for the varying conditions. This is especially important as the type-II correction presented here has been derived with the dataset recorded in 2010 only, where pile up was negligible. This will be the main future task regarding the $\not\!\!E_{\mathrm{T}}$ corrections. Furthermore, the use of a larger dataset is expected to reduce the large statistical uncertainties on the type-II scale which currently are dominated by the small size of the used $Z \rightarrow ee$ sample. Since the CMS HCAL is highly non-compensating, the scale factor for the unclustered energy should be studied by taking into account its electromagnetic and hadronic components separately, which could further improve the accuracy of the determination of the scale.

For the upcoming data taking in 2012 and beyond, higher beam energies and luminosity will lead to more energetic objects in general. Thus, punch-through of high energetic jets is expected to become more relevant and affected events will start to contribute significantly to the high $\not\!\!E_{\mathrm{T}}$ tails. Therefore, possible punch-through identification strategies, like the method presented here, should be investigated in more detail in data.

Search for Supersymmetry

Varying pile up conditions will be the main challenging technical task in the near future, not only for the $\not\!\!E_{\mathrm{T}}$ measurement, but also for the other objects utilised in the presented analysis. The photon isolation cones, for example, are sensitive to pile up and need to be adapted correspondingly to avoid possible losses in signal efficiency.

The largest uncertainty on the combined background estimation is currently due to the large uncertainty assumed on the ISR/FSR background taken from

MC simulation (100%). Further studies, e.g. the comparison between different MC generators, might allow a less conservative estimation of these errors.

To optimise the analysis and cover more of the GGM signal parameter space, the signal selection could be refined to search, in addition to the current selection, for b-jets in the final state. This should suppress the remaining Standard Model backgrounds, while enhancing the contribution from possible GGM signal with a more higgsino-like neutralino. Additional b-jets are also expected in GGM models, where the third-generation squarks are lighter than the other squarks and not degenerate as assumed in the models studied here. For higher squark and gluino masses, direct electroweak production of the neutralinos and charginos becomes more important. This leads to shorter signal cascades and less jets in the event. Thus, the signal acceptance for the analysis presented here is expected to decrease. Less stringent jet selection and possible further lepton requirements should be used to optimize GGM searches in this high mass region.

The presented results provide stringent tests of GGM models with bino- and wino-like neutralinos. Specifically for models with a wino-like neutralino the previous limits published to date are significantly improved. The result using an integrated luminosity of $1.1\,\text{fb}^{-1}$ [74; 75] has already been presented at the Lepton-Photon [76] and SUSY [77] conferences and has been reinterpreted by [9]. The results presented here include an update using an integrated luminosity of $4.32\,\text{fb}^{-1}$. These results have recently been made public in [84].

Appendix A

Appendix

A.1 GGM Final States with Photons

A.1.1 NLO cross section Uncertainties

The renormalisation scale uncertainties on the NLO cross sections of the studied GGM parameter points are shown in Fig. A.1. The corresponding PDF uncertainties on the cross section are shown in Fig. A.2.

A.1.2 PDF Uncertainty on Acceptance

The PDF uncertainties on the acceptance included in the limit calculation in Chapter 5 are shown in Fig. A.3.

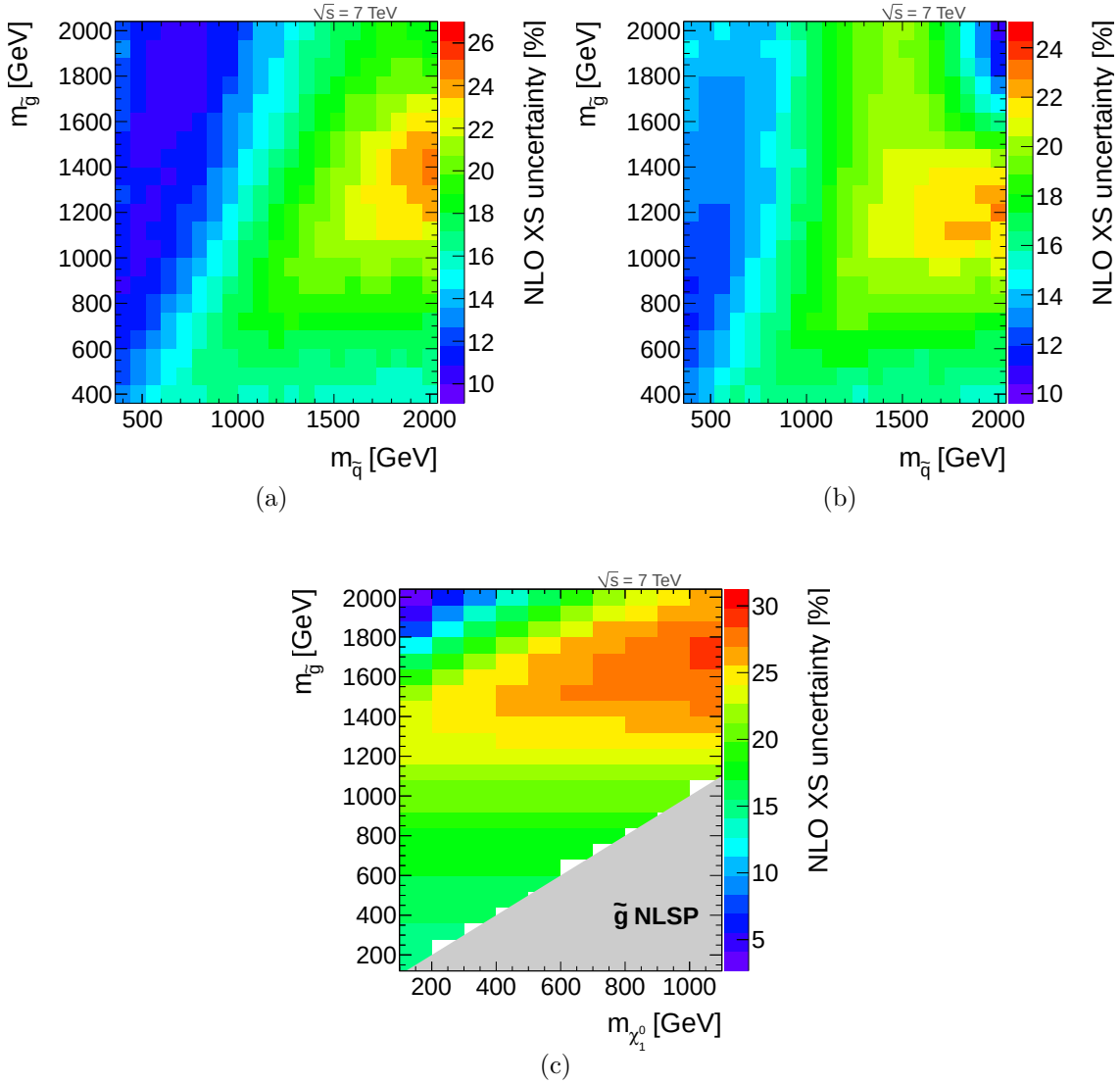

Figure A.1: Renormalisation scale uncertainties on the NLO cross sections in the squark-gluino mass plane of a (a) bino- and (b) wino-like neutralino with mass $M_{\tilde{\chi}_1^0} = 375$ GeV and (c) in the neutralino-gluino mass plane of a bino-like neutralino.

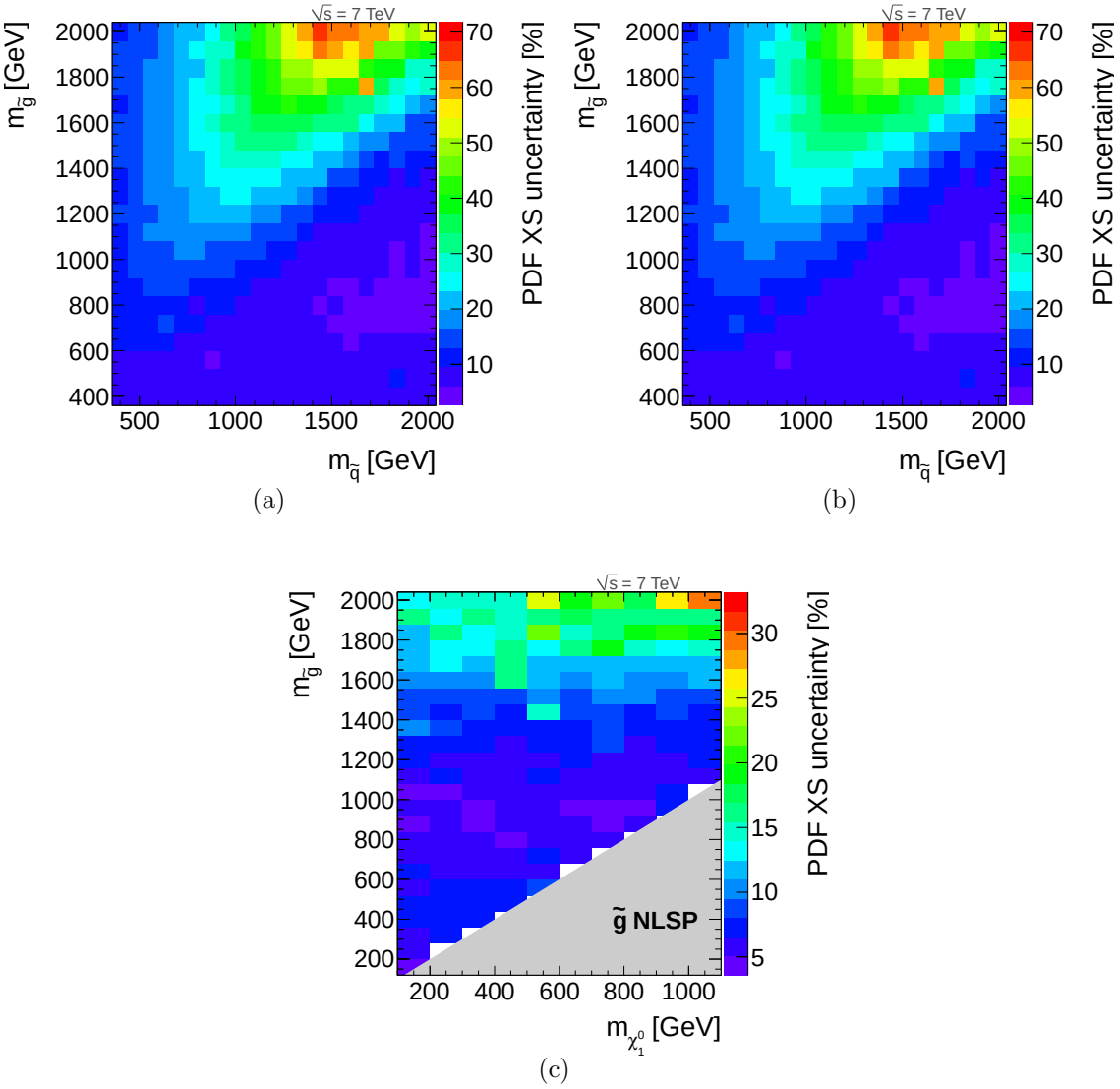

Figure A.2: PDF uncertainties on the NLO cross sections in the squark-gluino mass plane of a (a) bino- and (b) wino-like neutralino with mass $M_{\tilde{\chi}_1^0} = 375$ GeV and (c) in the neutralino-gluino mass plane of a bino-like neutralino.

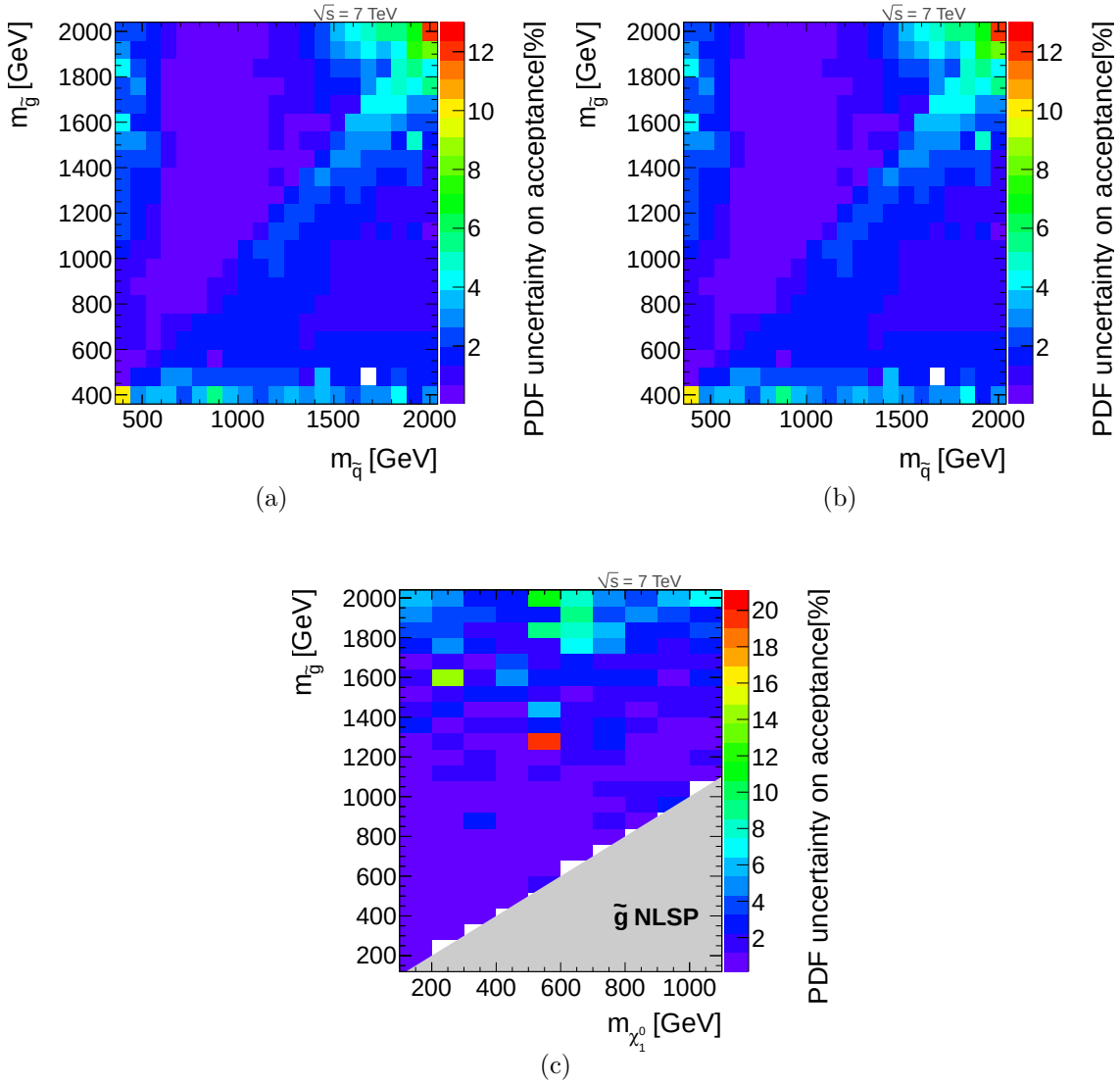

Figure A.3: PDF uncertainties on the acceptance in the squark-gluino mass plane of a (a) bino- and (b) wino-like neutralino with mass $M_{\tilde{\chi}_1^0} = 375$ GeV and (c) in the neutralino-gluino mass plane of a bino-like neutralino.

A.2 Measuring the Missing Transverse Energy: Used Datasamples and Trigger

A.2.1 $Z \to ee$ Events

Data (35.9 pb^{-1}):

Run 2010A:`/EG/Run2010A-Nov4ReReco_v1/RECO`

Run 2010B:`/Electron/Run2010B-Nov4ReReco_v1/RECO (runs:146240-149443)`

JSON:`Cert_136033-149442_7TeV_Nov4ReReco_Collisions10_JSON.txt(2010/11/29)`

Trigger requirement:

`HLT_Ele15_LW_L1R` or
`HLT_Ele15_SW_L1R` or
`HLT_Ele15_CaloEleId_L1R` or
`HLT_Ele17_CaloEleId_L1R` or
`HLT_Ele17_TightEleId_L1R` or
`HLT_Ele17_TighterEleIdIsol_L1R_v2` or
`HLT_Ele17_TighterEleIdIsol_L1R_v3` or

MC (No pile up):

`/DYToEE_M-20_TuneZ2_7TeV-pythia6/Fall10-START38_V12-v1/GEN-SIM-RECO`

MC (Including pile up):

`/DYToEE_M-20_CT10_TuneZ2_7TeV-powheg-pythia/`
`Fall10-E7TeV_ProbDist_2010Data_BX156_START38_V12-v1/GEN-SIM-RECO`

The MC is weighted to 35.9 pb^{-1}, in plots comparing Data and MC the number of events in MC is directly weighted to data.

A.2.2 Dijet Events

Data (0.02 pb^{-1}):

Run 2010A:`/JetMET/Run2010A-Nov4ReReco_v1/RECO`

Run 2010B:`/Jet/Run2010B-Nov4ReReco_v1/RECO (runs:146240-149443)`

JSON:/Cert_136033-149442_7TeV_Nov4ReReco_Collisions10_JSON.txt(2010/11/29)

Trigger requirement:

HLT_DijetAve15U (prescaled) or

HLT_DijetAve15U_v3 (prescaled)

MC:

/QCD_Pt_15to3000_TuneZ2_Flat_7TeV_pythia6

/Fall10-START38_V12-v1/GEN-SIM-RECO

The MC is weighted to 0.02 pb^{-1}, in plots comparing Data and MC the number of events in MC is directly weighted to data.

A.2.3 Minimum Bias Events

Data:

/MinimumBias/Commissioning10-GOODCOLL-Jun9thSkim/RECO

MC (No pile up):

/MinBias_7TeV-pythia8/Summer10-START36_V10_SP10-v1/GEN-SIM-RECODEBUG

A.3 Measuring the Missing Transverse Energy: Additional Material

A.3.1 U_T and R distribution in individual q_{T} bins

As described in Sec. 4.2 the average $U_{T,\parallel}$ and R in different q_{T} bins are utilised to derive the type-II correction scale. For this purpose the mean of the distribution in several q_{T} bins is obtained resulting in e.g. Fig. 4.4 for the Calo $\not\!\!E_{\text{T}}$ case. As an example the corresponding distributions from two q_{T} bins (13-14 GeV and 19-20 GeV) are shown in Fig. A.4. A Gauss fit around the mean of the histogram ($\pm 2\ \sigma$) is used to obtain the mean and its uncertainty.

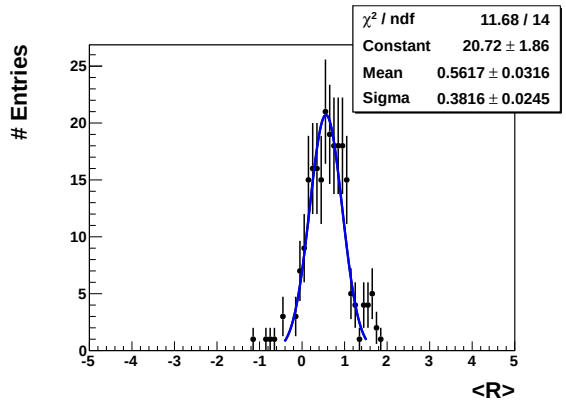

(a) 13 GeV$<q_{\mathrm{T}}<$14 GeV

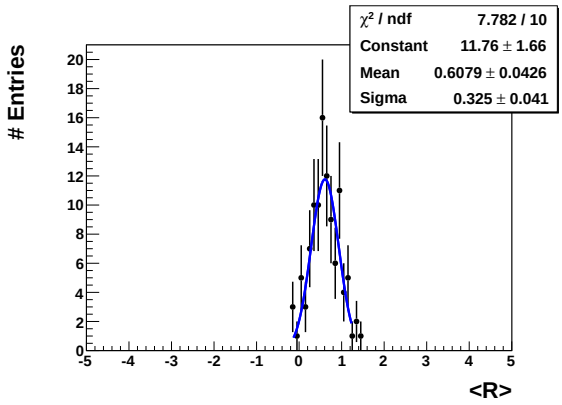

(b) 19 GeV$<q_{\mathrm{T}}<$20 GeV

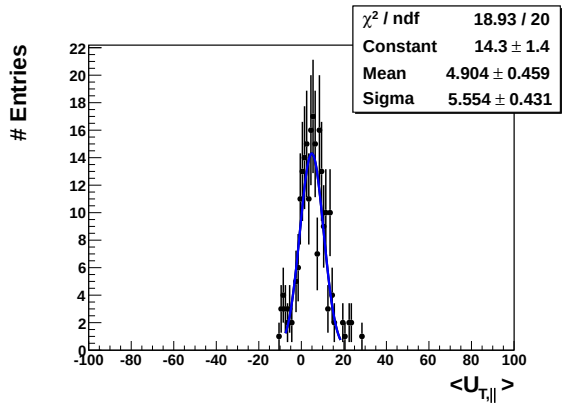

(c) 13 GeV$<q_{\mathrm{T}}<$14 GeV

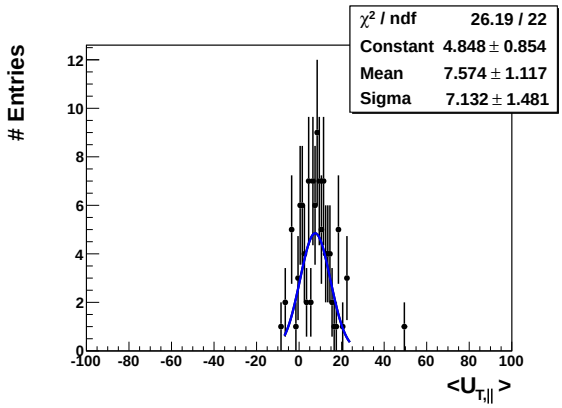

(d) 19 GeV$<q_{\mathrm{T}}<$20 GeV

Figure A.4: Calo $\not\!\!E_{\mathrm{T}}$ (Data): (a,b) R and (c,d) $U_{T,\parallel}$ distribution for a q_{T} range of (a,c) 13-14 GeV and (b,d) 19-20 GeV. A truncated Gauss, fitted around the mean ($\pm 2\ \sigma$), is shown as a blue line.

A.3.2 Calo $\not\!\!E_{\mathrm{T}}$ Performance in $Z \to ee$ Events

The observed influence of the JES to the resulting $\not\!\!E_{\mathrm{T}}$ scale in $Z \to ee$ events has been discussed in Sec. 4.3.1.2 for PF $\not\!\!E_{\mathrm{T}}$ only. For completeness the corresponding result for Calo $\not\!\!E_{\mathrm{T}}$ is shown in Fig. A.5.

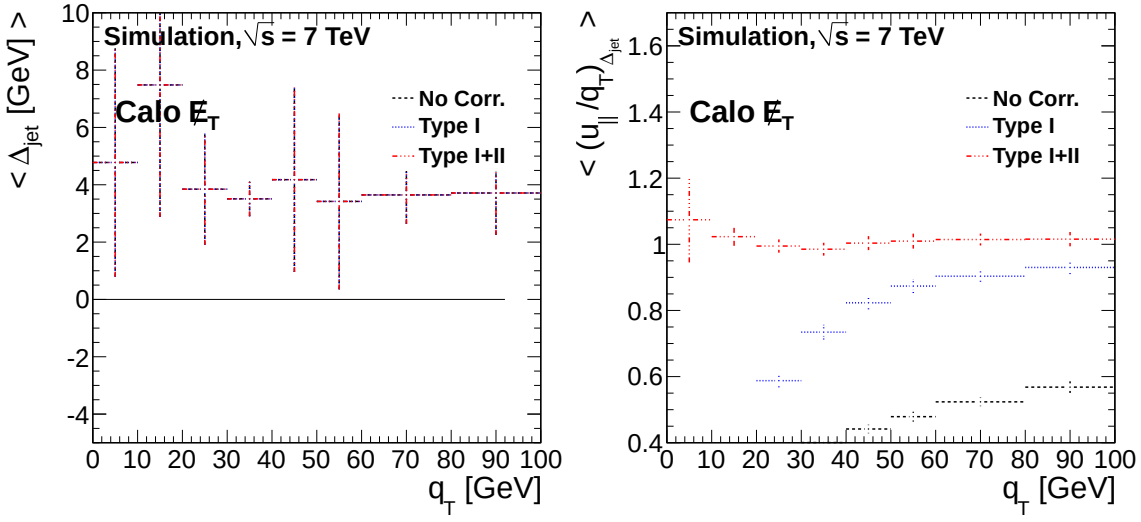

(a) (b)

Figure A.5: Calo $\not\!\!E_{\mathrm{T}}$ (inclusive jets, simulation only):(a) $< \Delta_{jet} >$ and (b) $(\frac{u_{\parallel}}{q_{\mathrm{T}}})_{\Delta_{jet}}$ in dependence of q_{T}.

A.4 Search for Supersymmetry: Used Datasamples and Trigger

A.4.1 Data

Photon+HT Dataset ($4.32\,\mathrm{fb}^{-1}$):

/PhotonHad/Run2011A-May10ReReco-v1/AOD

JSON:/Cert_160404-163869_7TeV_May10ReReco_Collisions11_JSON_v3.txt (2011/08/25)

/PhotonHad/Run2011A-05Aug2011-v1/AOD

JSON:/Cert_170249-172619_7TeV_ReReco5Aug_Collisions11_JSON_v3.txt (2011/10/19)

/PhotonHad/Run2011A-PromptReco-v4/AOD

/PhotonHad/Run2011A-PromptReco-v6/AOD

/PhotonHad/Run2011B-PromptReco-v1/AOD

JSON:/Cert_160404-180252_7TeV_PromptReco_Collisions11_JSON.txt (2011/11/04)

Trigger requirement:

HLT_Photon70_CaloIdL_HT200_v1-2 or
HLT_Photon70_CaloIdL_HT300_v1-6 or
HLT_Photon70_CaloIdL_HT350_v1-6 or
HLT_Photon70_CaloIdL_HT400_v3-1 or
HLT_Photon70_CaloIdXL_HT400_v3-1

Single Photon Dataset ($190\ \mathrm{pb}^{-1}$) for HT300 trigger studies:

PromptReco:/Photon/Run2011A-PromptReco-v1/AOD

PromptReco:/Photon/Run2011A-PromptReco-v2/AOD

JSON:/Cert_160404-166502_7TeV_PromptReco_Collisions11_JSON.txt (2011/06/10)

Trigger requirement:

HLT_Photon75_CaloIdVL_v1-5

A.4.2 MC Simulation: SM Backgrounds

QCD multi-jet:

/QCD_Pt-120to170_TuneZ2_7TeV_pythia6
/Fall11-PU_S6_START42_V14B-v1/AODSIM
Cross section: 115 000 pb
Number of generated events: $6{\cdot}10^6$

/QCD_Pt-170to300_TuneZ2_7TeV_pythia6
/Fall11-PU_S6_START42_V14B-v1/AODSIM
Cross section: 24 300 pb
Number of generated events: $6{\cdot}10^6$

/QCD_Pt-300to470_TuneZ2_7TeV_pythia6
/Fall11-PU_S6_START42_V14B-v1/AODSIM
Cross section: 1170 pb
Number of generated events: $6{\cdot}10^6$

/QCD_Pt-470to600_TuneZ2_7TeV_pythia6
/Fall11-PU_S6_START42_V14B-v1/AODSIM
Cross section: 70.2 pb
Number of generated events: $4{\cdot}10^6$

/QCD_Pt-600to800_TuneZ2_7TeV_pythia6
/Fall11-PU_S6_START42_V14B-v1/AODSIM
Cross section: 15.6 pb
Number of generated events: $4{\cdot}10^6$

/QCD_Pt-800to1000_TuneZ2_7TeV_pythia6
/Fall11-PU_S6_START42_V14B-v1/AODSIM
Cross section: 1.84 pb
Number of generated events: $4{\cdot}10^6$

/QCD_Pt-1000to1400_TuneZ2_7TeV_pythia6
/Fall11-PU_S6_START42_V14B-v1/AODSIM
Cross section: 0.332 pb
Number of generated events: $2{\cdot}10^6$

/QCD_Pt-1400to1800_TuneZ2_7TeV_pythia6
/Fall11-PU_S6_START42_V14B-v1/AODSIM
Cross section: 0.011 pb
Number of generated events: $2{\cdot}10^6$

/QCD_Pt-1800_TuneZ2_7TeV_pythia6
/Fall11-PU_S6_START42_V14B-v1/AODSIM
Cross section: 0.000358 pb
Number of generated events: $1{\cdot}10^6$

$\gamma - jet$**:**
/G_Pt_15to3000_TuneZ2_Flat_7TeV_pythia6
/Fall11-PU_S6_START42_V14B-v1/AODSIM
Cross section: $1.5{\cdot}10^7$ pb
Number of generated events: $10 \cdot 10^6$

W+Jets:
/WJetsToLNu_TuneZ2_7TeV-madgraph-tauola
/Fall11-PU_S6_START42_V14B-v1/AODSIM
Cross section: 27770 pb
Number of generated events: $81{\cdot}10^6$

$t\bar{t}$**+Jets:**
/TTJets_TuneZ2_7TeV-madgraph-tauola
/Fall11-PU_S6_START42_V14B-v1/AODSIM
Cross section: 94.76 pb
Number of generated events: $3.6{\cdot}10^6$

V+γ**+Jets:**
/GVJets_7TeV-madgraph
/Fall11-PU_S6_START42_V14B-v1/AODSIM
Cross section: 56.64 pb
Number of generated events: $1{\cdot}10^6$

A.4.3 MC Simulation: GGM Signal

The following MC samples have been generated for the GGM signal scans:

Bino-like neutralino (gluino-squark mass plane):
Number of generated events: 10 000/parameter point
Bin width: 80 GeV

Bino-like neutralino (gluino-neutralino mass plane):
Number of generated events: 10 000/parameter point
Bin width (gluino): 80 GeV
Bin width (neutralino): 100 GeV

Wino-like neutralino (gluino-squark mass plane):
Number of generated events: 60 000/parameter point
Bin width: 80 GeV

A.5 Search for Supersymmetry: Trigger Efficiencies

The effect of the $n90$ vs. $n90Hits$ cut on the trigger level has been discussed in Sec. 5.1.1. Here the effect on the trigger efficiency is studied using $\sim 1\,\mathrm{fb}^{-1}$ of the 2011 data. For the case where the HT is calculated with the JetID cut on $n90Hits$ the trigger efficiency is shown in figure A.6(a). For comparison the trigger efficiency of the HT requirement with the Jet-ID cut on $n90$ is shown in A.6(b). The drop in the efficiency due to the cut on $n90$ is clearly visible in the left plot. **Denominator**

- require Photon75_CaloIdVL fires
- require at least 1 photon passing the photon ID
- $p_{\mathrm{T}} \geq 80$ and $|\eta| \leq 1.4$ for the photon

Nominator

- require all denominator cuts
- require Photon70_CaloIdL_HT300 fires

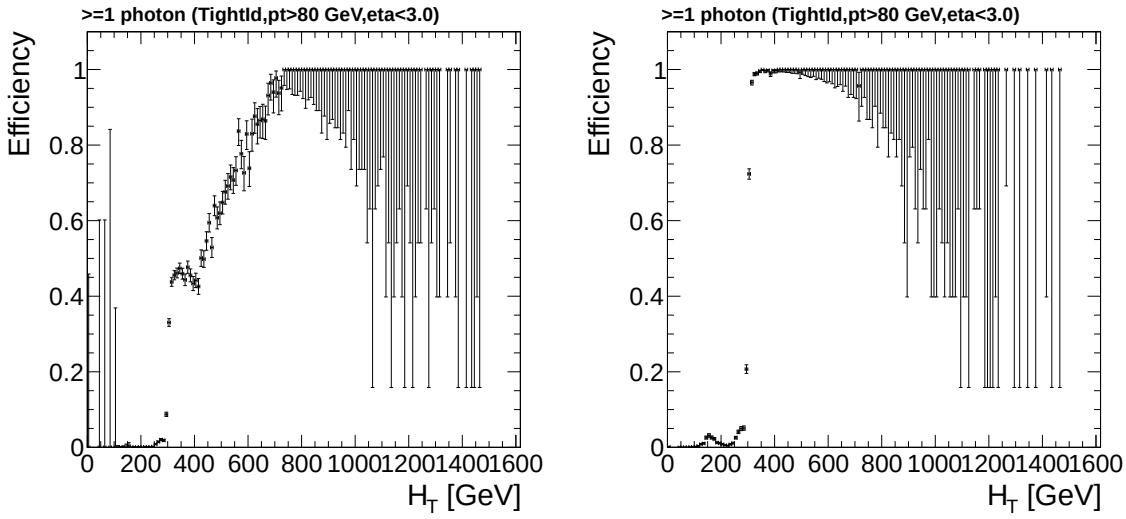

(a) (b)

Figure A.6: Trigger Efficiency of the HT requirement of the Photon70_CaloIdL_HT300 trigger. In the left figure the Jet-ID cut is applied on $n90Hits$, in the right figure the cut is applied on $n90$.

A.6 Search for Supersymmetry: QCD Background Estimation

In this section additional material regarding the QCD background estimation is provided.

A.6.1 Number of Jet Dependency

As described in Sec. 5.2.1 the distribution of inverse weights shows a dependency on the number of jets. However, the correction is only applied for two different

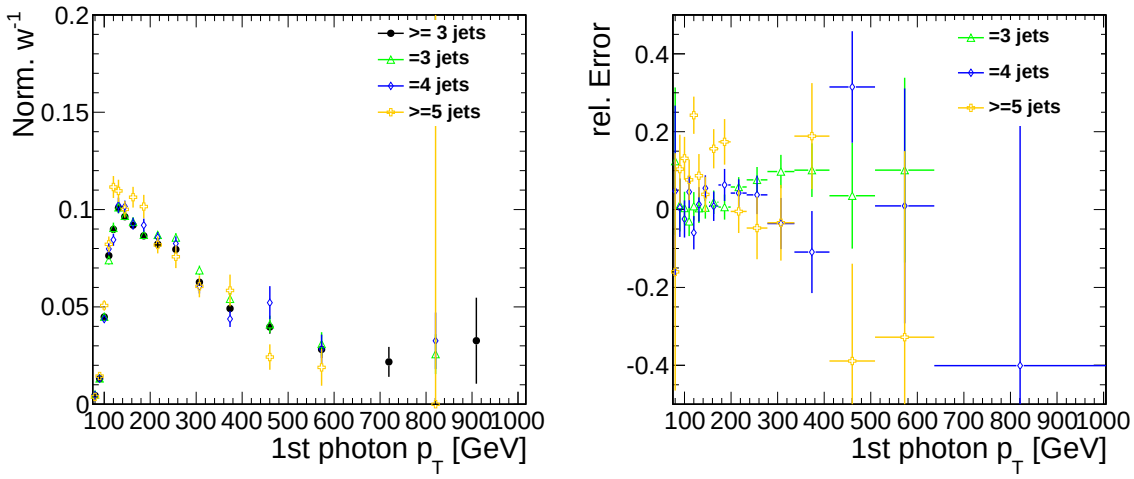

(a) (b)

Figure A.7: (a) Normalised ratio of jet-photon fakeable objects to photons for events with different jet multiplicities and (b) corresponding relative difference to the inclusive ≥ 3 jet distribution.

jet multiplicity bins (exactly two and three or more jets) as the statistical errors are large for events with high multiplicity. The normalised inverse weight distributions obtained in events with higher jet multiplicities are compared to the applied inclusive distribution in Fig. A.7 (a). The relative differences between each of the distributions and the inclusive distribution are shown in Fig. A.7 (b).

A.6.2 Reweighting Control Distributions

The $\not\!\!E_{\mathrm{T}}$ distributions of photon and γ_{Jet} sample before reweighting are shown in Fig. A.9

The γ_{Jet} p_{T} distributions after the reweighting are expected to model the photon p_{T} distribution nearly perfectly, as the weight is obtained in dependence of the photon p_{T}. Small differences are expected from events with $\not\!\!E_{\mathrm{T}} \geq 100$ GeV, which are not included for the determination of the weights. The resulting p_{T} distributions are shown in Fig. A.8 for data and simulation and both jet selections.

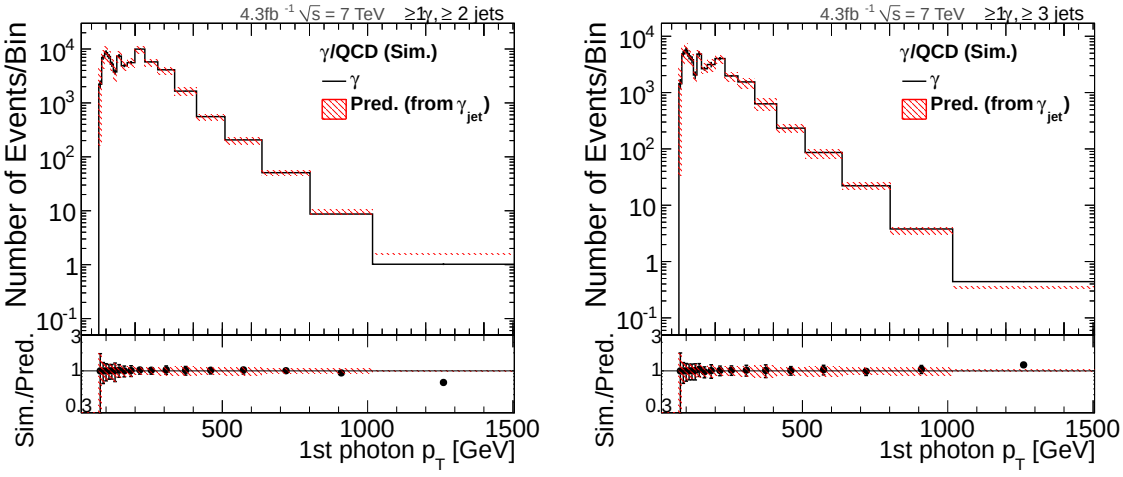

(a) (b)

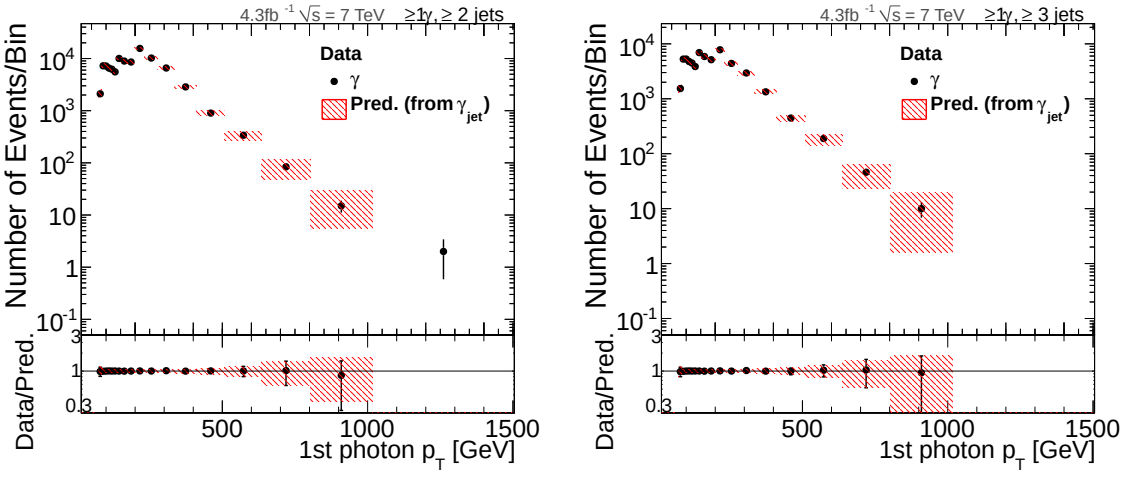

(c) (d)

Figure A.8: p_{T} distribution of γ and γ_{Jet} after reweighting in (upper row) γ/QCD simulation and (lower row) data. The systematic uncertainty due to statistical errors of the weights and the kinematical differences between control region and the whole spectrum is shown as hatched band for events with (left column) $\geq$2 and (right column) $\geq$3 jets.

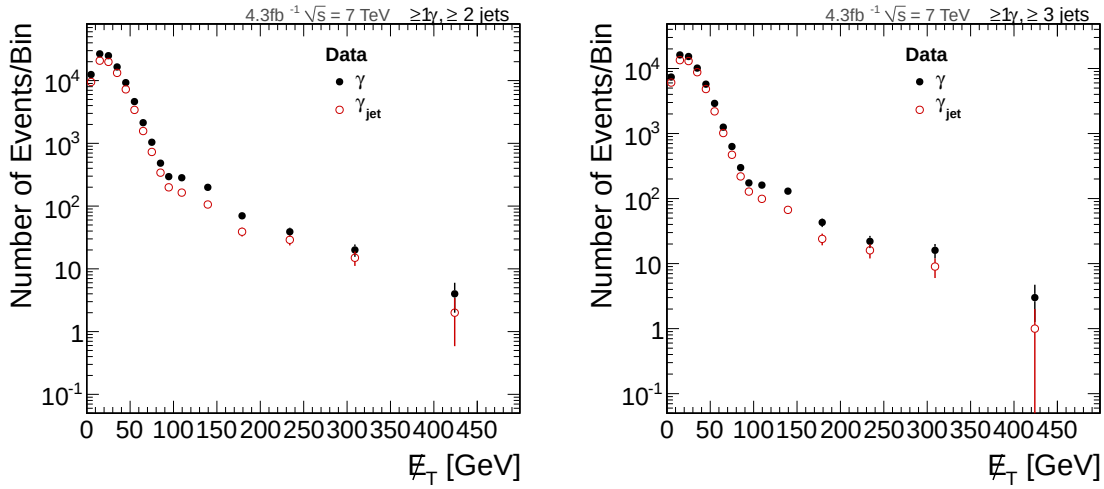

(a) (b)

Figure A.9: Data (4.32 fb^{-1}): $\not{E}_T$ distribution of γ and γ_{Jet} before reweighting for events with (a) ≥2 and (b) ≥3 jets.

A.6.3 Contamination from Standard Model and GGM Processes

As described in Sec. 5.2.1 the effect on the obtained weights from both, Standard Model and possible GGM signal processes, is expected to be small. The obtained weight distribution from simulation containing all Standard Model processes[1] is compared to the weights obtained from the γ/QCD simulation in Fig. A.10 showing a very small impact due to the Standard Model contamination of the control sample. The corresponding plots for a sample GGM point ($m_{\tilde{q}} = 2500$ GeV, $m_{\tilde{g}} = 800$ GeV, $m_{\tilde{\chi}_1^0(\text{bino})} = 650$ GeV) are shown in Fig. A.11 verifying also the negligible effect of signal contamination on the control sample used for the determination of the weights.

[1]The contributing samples are listed above (App. A.4).

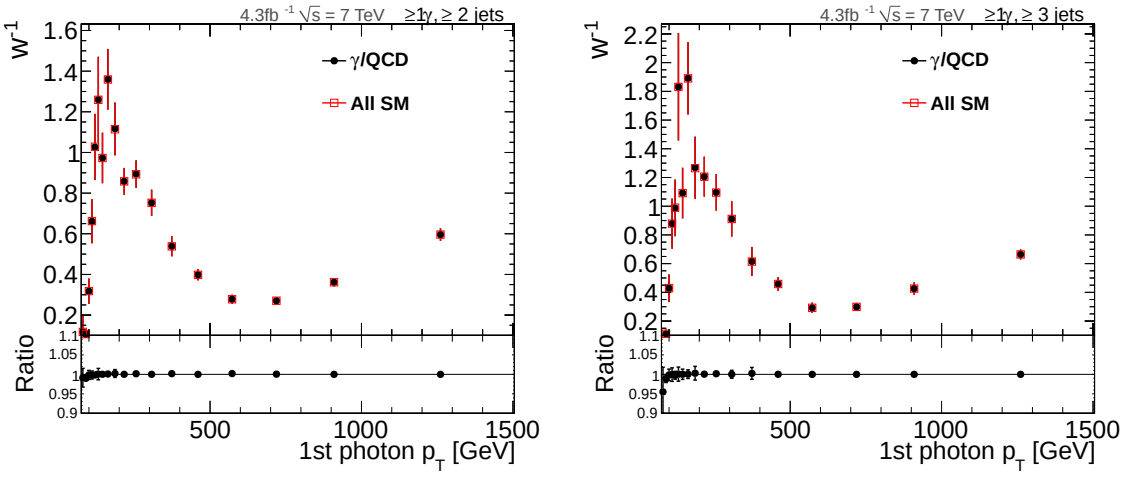

(a) (b)

Figure A.10: Inverse weight in dependence of γ p_{T} in γ/QCD and all Standard Model MC in events with (a) $\geq$2 and (b) $\geq$3 jets.

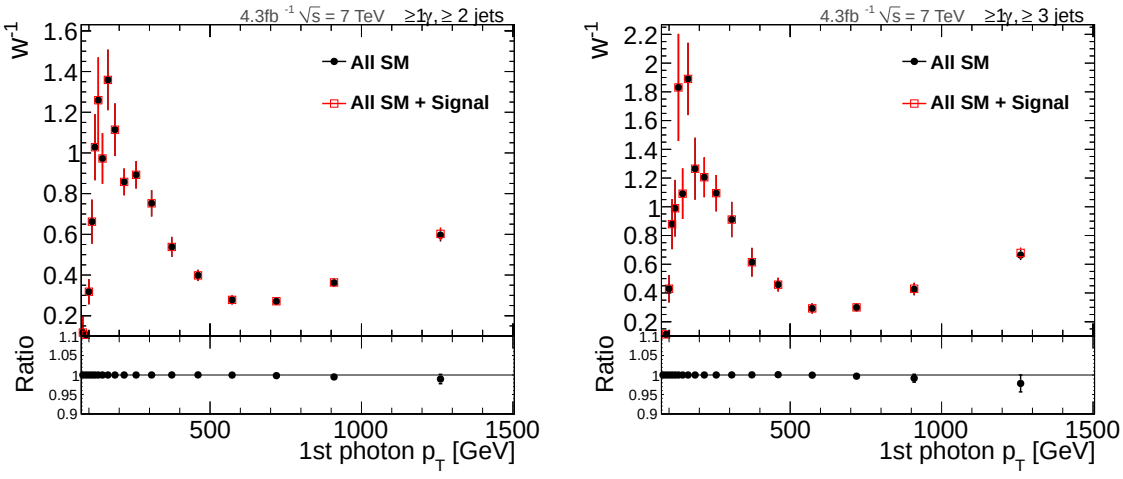

(a) (b)

Figure A.11: Inverse weight in dependence of γ p_{T} in simulated Standard Model events and simulated events containing GGM Signal MC in addition ($m_{\tilde{q}} = 2500$ GeV, $m_{\tilde{g}} = 800$ GeV, $m_{\tilde{\chi}_1^0(\mathrm{bino})} = 650$ GeV) with (a) $\geq$2 and (b) $\geq$3 jets.

A.7 Search for Supersymmetry: $e \to \gamma$ Background Estimation

The $\not\!\!E_{\mathrm{T}}$ distributions of the electron control sample before and after reweighting are shown in Fig. A.12 for both jet selections. The distributions are compared to the full data signal selection containing also γ/QCD background, which is significantly larger, and possible signal.

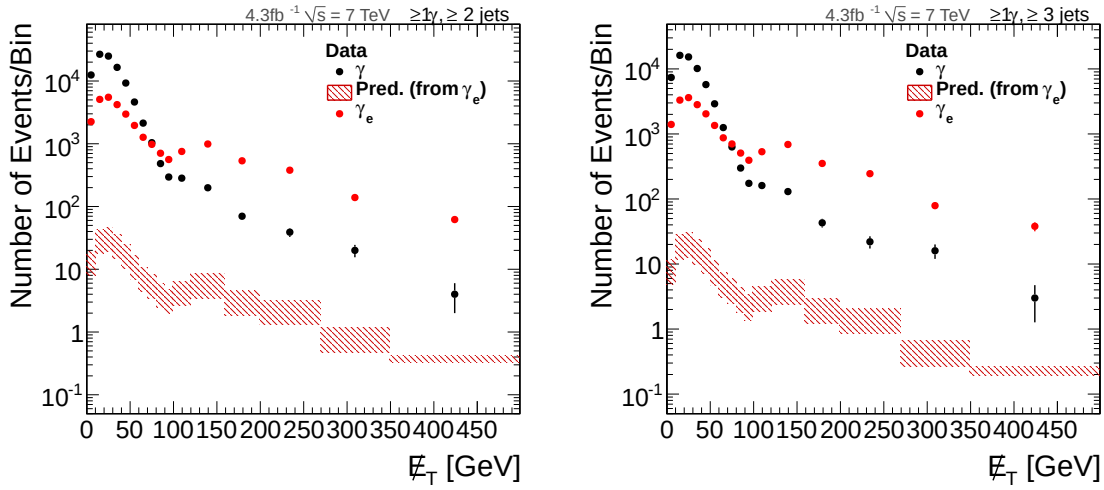

(a) (b)

Figure A.12: The electroweak background prediction (hatched) is compared to the data signal selection (black points) in events with (a) ≥2 and (b) ≥3 jets. For comparison the unweighted control sample with one electron is shown (red points). Note, that the data contains also γ/QCD background which is significantly larger compared to the $e \to \gamma$ background, and possible signal.

A.8 Search for Supersymmetry: Additional Material

In this section more details about the obtained results, described in Sec. 5.3 are given.

A.8.1 Additional Distributions

The combined data driven background prediction has been compared to the observed data in several variables, besides $\not\!\!E_{\mathrm{T}}$, to crosscheck the result for possible influence of other variables. This includes jet p_{T} distributions, η and ϕ distributions of the photon and jets, the number of primary vertices, angular distributions between the jets and the photon-like object, ΣE_{T}, the vector sum of the jets H_T, the number of jets, etc.

In general a good agreement between the data and the background prediction was found as shown exemplarily in Fig. A.13 and Fig. A.14 for the $\geq$3 jet selection[1]. Some variables, like ΣE_{T}, show for lower values a small bias between the data and the γ_{Jet} distribution. This small effect is due to the imperfect modeling of the γ_{Jet} resolution and energy scale by the matched jet used for the reweighting. This effect can be corrected with specialised energy corrections for the photon-like object which ,if propagated to the $\not\!\!E_{\mathrm{T}}$, should remove also the current bias in the corrected $\not\!\!E_{\mathrm{T}}$ distribution. The number of jet distribution is showing slight differences between the data and the combined background estimation, which is expected, as the probability to have a jet passing the γ_{Jet} criteria becomes higher with more jets in the events and the current correction is applied per event independently on the number of jets. The effect of an additional correction depending on the number of jets in the event has been studied and is discussed in the next section.

[1] The $\geq$2 jet selection yields very similar results

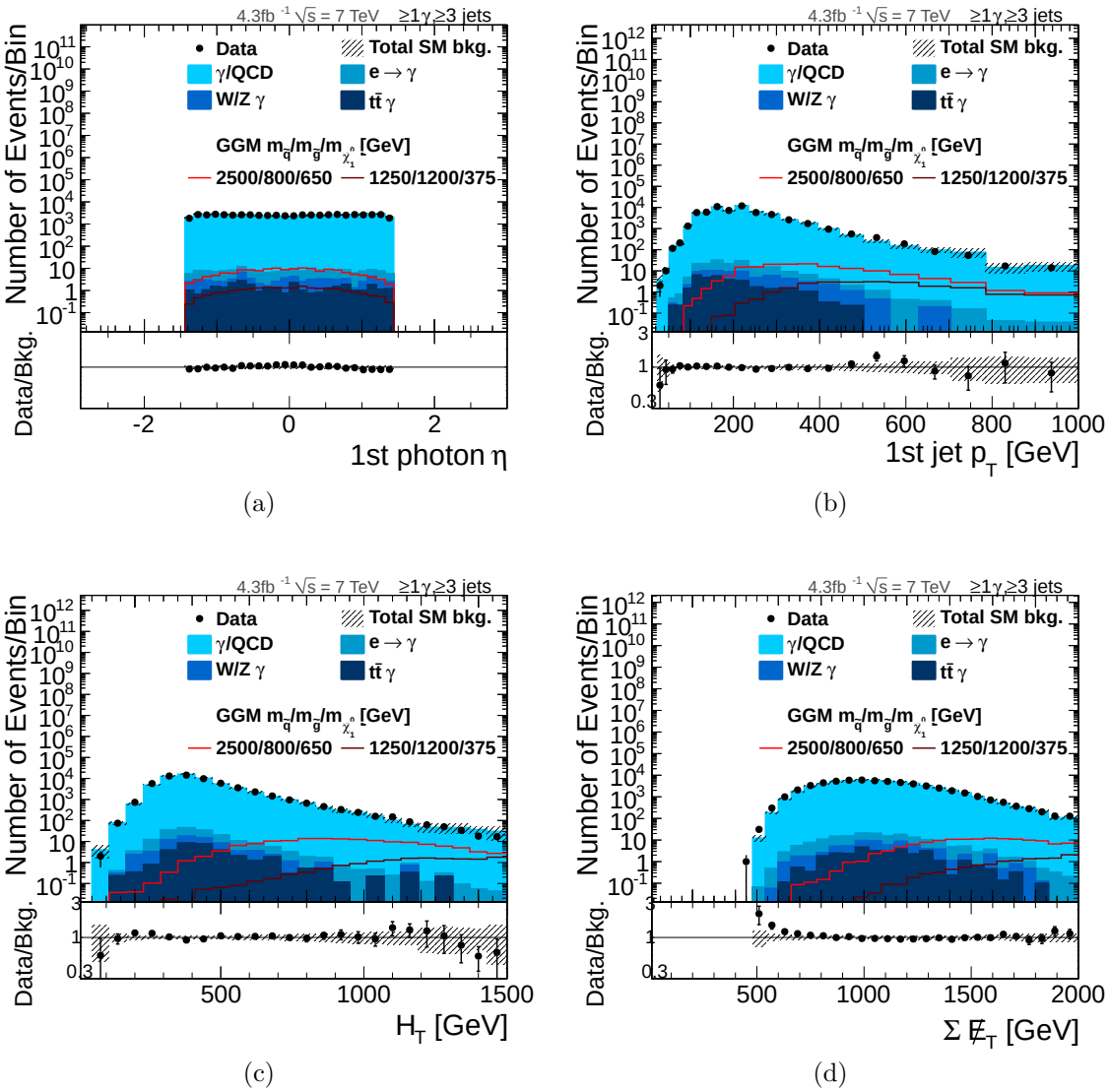

Figure A.13: Total standard model background prediction, as discussed above, compared to the selected number of events in 4.32 fb^{-1}and two exemplary GGM signal benchmark points ($m_{\tilde{q}}$[GeV]/ $m_{\tilde{g}}$[GeV]/ $m_{\tilde{\chi}_1^0}$[GeV]) before the final cut on $\not{E}_{\mathrm{T}}$ for (a) photon η, (b) leading jet p_{T}, (c) scalar sum of the jets (H_T), and (d) for the ≥3 jet selection.

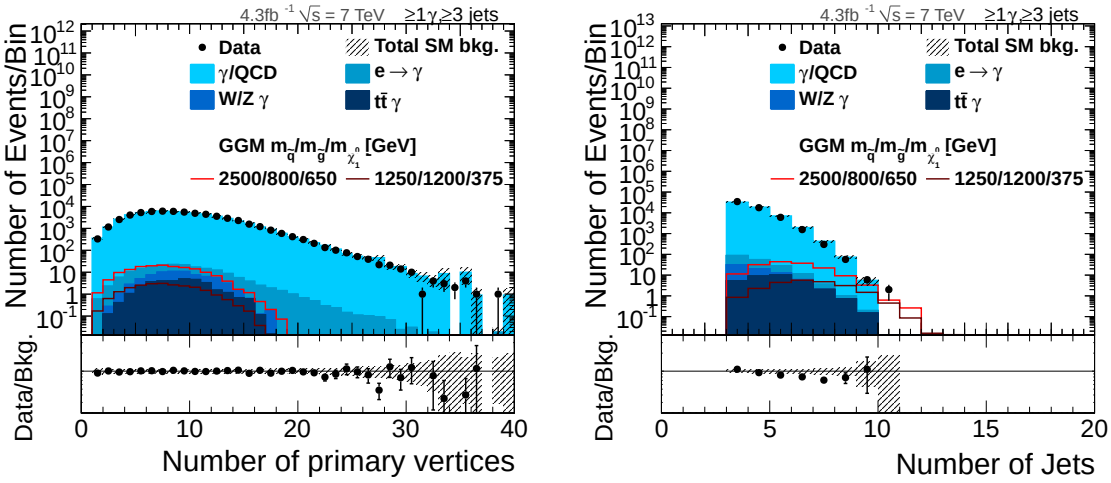

(a) (b)

Figure A.14: Total standard model background prediction, as discussed above, compared to the selected number of events in $4.32\,\mathrm{fb}^{-1}$and two exemplary GGM signal benchmark points ($m_{\tilde{q}}[\,\mathrm{GeV}]$/ $m_{\tilde{g}}[\,\mathrm{GeV}]$/ $m_{\tilde{\chi}_1^0}[\,\mathrm{GeV}]$) before the final cut on $\not\!\!E_{\mathrm{T}}$ for (a) the number of primary vertices and (b) the number of jets in the events.

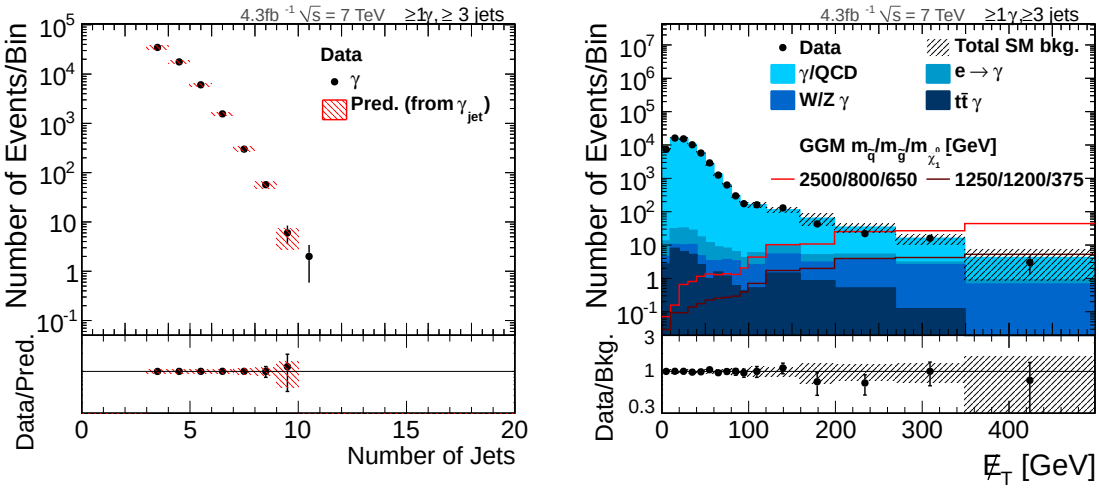

(a) (b)

Figure A.15: (a) Jet multiplicity distribution of the prediction (hatched) compared to the corresponding distribution of the data signal selection (black points) (b) $\not{E}_T$ distribution after the application of the additional correction in dependence of the number of jets.

A.8.2 Number of Jet Reweighting

As the resulting distribution of the number of jets in the event shows a slight difference between data and the combined background estimation, an additional correction depending on this variable and its effect on the $\not{E}_T$ prediction has been studied. The additional correction is applied very similarily to the photon p_T dependent corrections applied previously. Again, the ratio between the number of γ_{Jet} events and photon events in each bin is taken as inverse weight for the reweighting. As expected the jet multiplicity distribution shows no differences any more after the new reweighting as shown in Fig. A.15(a). The resulting combined $\not{E}_T$ prediction, with the number-of-jet correction applied on top is shown in Fig. A.15(b) and is, as expected, very similar to the current background estimation. E.g. for the $\not{E}_T \geq 200$ GeV signal region, the effect is in the order of 2%, which is negligible compared to the statistical and other systematic uncertainties. Therefore this additional correction is not applied in the analysis.

A.8.3 Photon vs. Jet p_{T} Reweighting

As discussed in section Sec. 5.1.3, the photon four-momentum is replaced by the corresponding jet momentum to account for the hadronic energy fraction of the γ_{Jet} objects. This is especially important for the the γ/QCD prediction, i.e. the reweighting in dependence of the photon-like object p_{T}.

The purpose of the reweighting is to model the hadronic recoil of the event as it is dominating the $\not\!\!E_{\mathrm{T}}$ in the γ/QCD events. If the γ_{Jet} definition allows objects with non-negligible hadronic fraction, the jet matching the γ_{Jet} object gives a better estimate for the hadronic recoil than the photon object only. The usage of the photon object only might introduce a bias between the γ_{Jet} control sample and the data, leading to a shift of the predicted $\not\!\!E_{\mathrm{T}}$ distribution to higher values. This becomes visible in a slight falling tendency of the ratio between data and background estimation.

However, the size of this effect is strongly dependent on the exact definition of the γ_{Jet} object. For a very loose definition of the γ_{Jet} object, i.e. changing the used definition such that no upper cut on the isolation is required, the predicted $\not\!\!E_{\mathrm{T}}$ distribution is shifted by $\sim$1 GeV if the photon-object p_{T} is used for the reweighting. The usage of the matched jet p_{T} instead removes the resulting bias as shown in Fig. A.16.

For the γ_{Jet} definition used in this analysis the resulting effect is negligible as shown in Fig. A.17, where the $\not\!\!E_{\mathrm{T}}$ prediction with the jet p_{T} reweighting is compared to the result achieved with the photon p_{T} reweighting for the γ_{Jet} definition used previously in the analysis. The difference between both methods on the signal event yield was found to be in the order of 5% .

A.8.4 Study of High $\not\!\!E_{\mathrm{T}}$ Events

The events with $\not\!\!E_{\mathrm{T}} \geq 300$ GeV have been studied in detail to identify possible effects due to noise or problems in the event reconstruction. As outlined in Sec. 5.3 no obvious indication of fake energies was found, neither in the signal nor in the selected control samples. However, a few events with possible contributions due to masked ECAL cells were identified utilising the methods described in chapter 4. To identify possible effects from punch-through the number of hits behind the jets

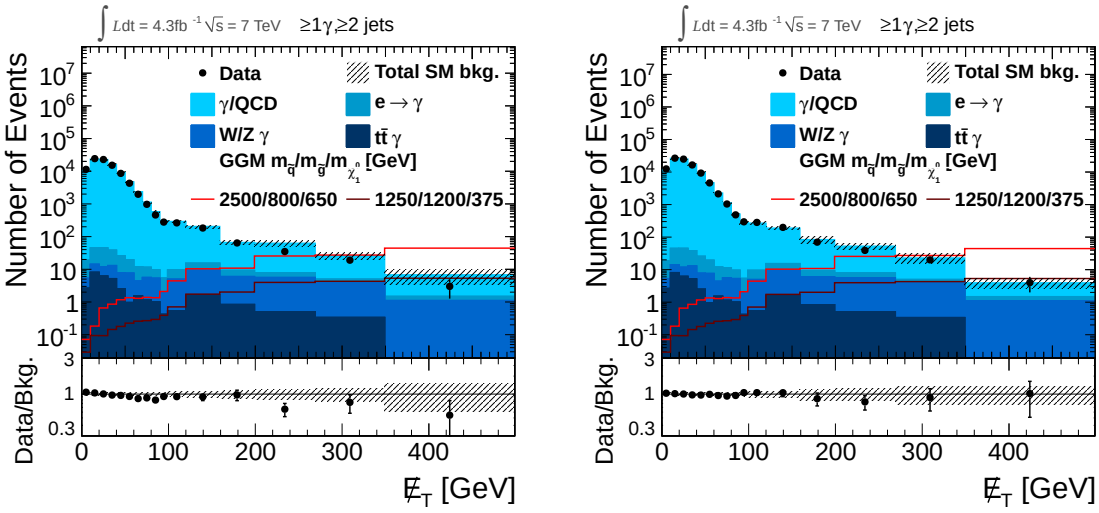

Figure A.16: Total standard model background prediction as discussed above compared to the selected number of events in $4.32\,\mathrm{fb}^{-1}$and two exemplary GGM signal benchmark points ($m_{\tilde{q}}$[GeV]/ $m_{\tilde{g}}$[GeV]/ $m_{\tilde{\chi}_1^0}$[GeV]) before the final cut on $\not{E}_{\mathrm{T}}$. For (a) the reweighting for the γ/QCD background is done using the photon-object p_{T}, while for (b) the reweighting is done using the matched jet $p_{\mathrm{T}}$for the reweighting. In both cases a very loose γ_{Jet} definition with no upper cut on the photon isolation is applied.

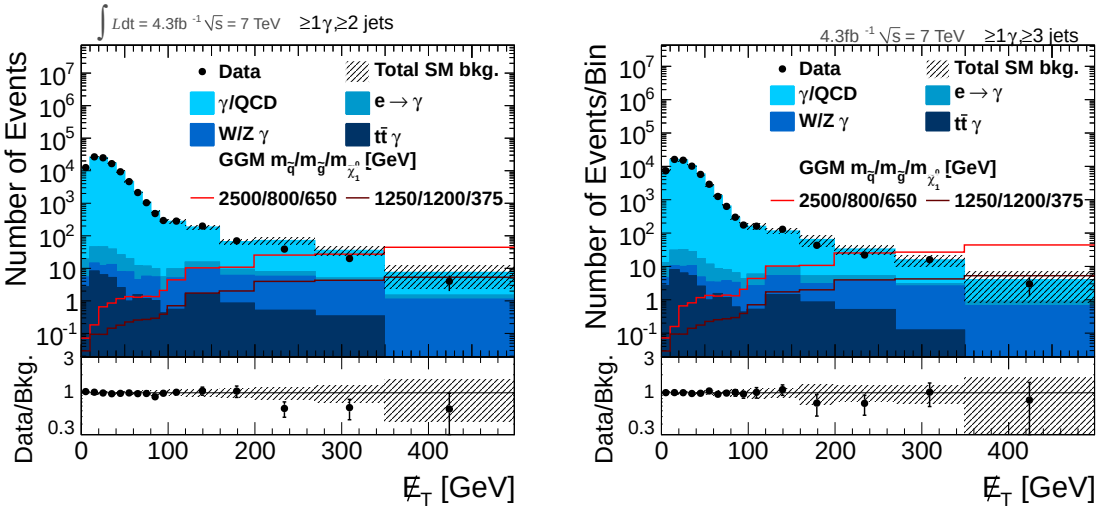

(a) (b)

Figure A.17: Total standard model background prediction as discussed above compared to the selected number of events in 4.32 $\mathrm{fb}^{-1}$and two exemplary GGM signal benchmark points ($m_{\tilde{q}}$[GeV]/ $m_{\tilde{g}}$[GeV]/ $m_{\tilde{\chi}_1^0}$[GeV]) before the final cut on $\not{E}_{\mathrm{T}}$. For (a) the reweighting for the γ/QCD background is done using the photon-object p_{T}, while for (b) the reweighting is done using the matched jet $p_{\mathrm{T}}$for the reweighting.

was checked. In a few events more than 9 hits in the muon RPC subsystem were found, while the jet was not tagged as a b jet. The affected events occur with a low rate and in data, as well as in the control distributions, therefore the effect on the resulting event yields and limits is expected to be negligible compared to the other uncertainties.

In principle these events can be excluded from the final selection to reduce the expected number of Standard Model background events and optimize the results. However, this needs careful studies about the efficiency of the selection on GGM signal and tuning of the cut parameters. The punch-through identification criteria are based on preliminary, simulation based, studies and should be refined on data to make final conclusions about the handling of these events.

In Table A.1 the number of events possibly affected by one of the discussed problems is summarised for the studied high $\not\!\!E_{\mathrm{T}}$ signal and control sample.

Table A.1: Summary of high $\not\!\!E_{\mathrm{T}}$ events scanned for punch-through and effects from masked ECAL cells. For each sample (γ,γ_{Jet},) the number of analysed events, number of events possibly affected by punch-through and masked cells identified by the criteria discussed above are shown.

Event type	No. of events possibly affected by		No. of analysed events
	masked ECAL cells	punch-through	
γ_{Jet}	2	0	9
γ	2	1	12
γ_e	4	7	150

A.9 Search for Supersymmetry: GGM Interpretation

A.9.1 Signal Contamination

As described in Sec. 5.4 the number of expected background events from signal is subtracted from the expected signal events passing the selection for the statistical interpretation of the result. The ratio between the expected background events from GGM signal and the expected number of GGM events passing the final selection is called signal contamination. It is shown in the studied GGM mass planes in Fig. A.18.

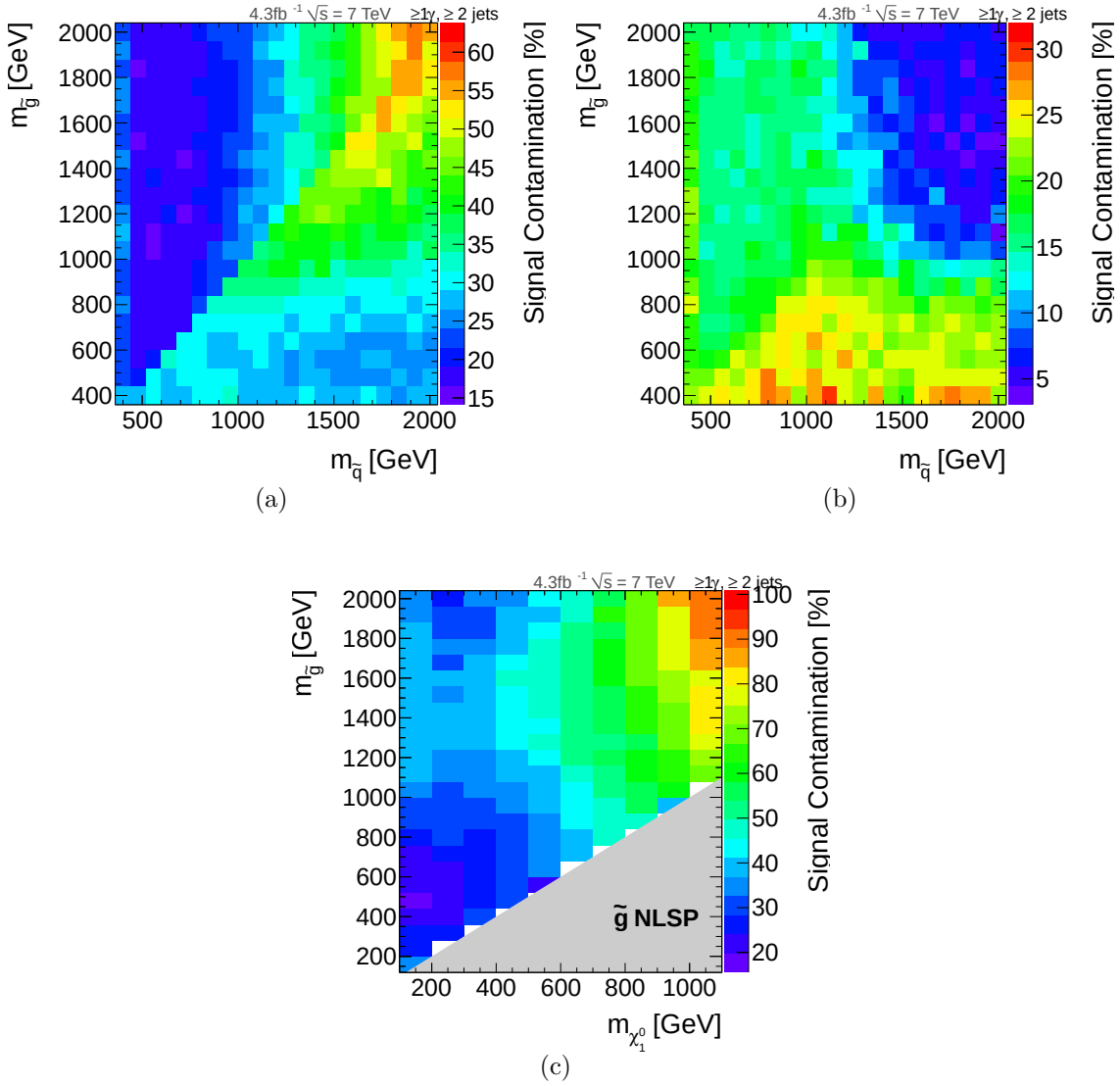

Figure A.18: Ratio between the expected background events from GGM signal and the expected number of signal events per GGM parameter point (signal contamination) in the squark-gluino mass plane of a (a) bino- and (b) wino-like neutralino with $M_{\tilde{\chi}_1^0} = 375\,\text{GeV}$ and (c) in the neutralino-gluino mass plane of a bino-like neutralino.

A.9.2 Comparison of Jet Selections (≥2 Jet vs. ≥3 Jet)

The interpretation of the results has been discussed in detail for the ≥2 jet selection in Sec. 5.4. The resulting 95% CL exclusion limits are compared between both jet selection in Fig. A.19. The expected limits are very similar between both results.

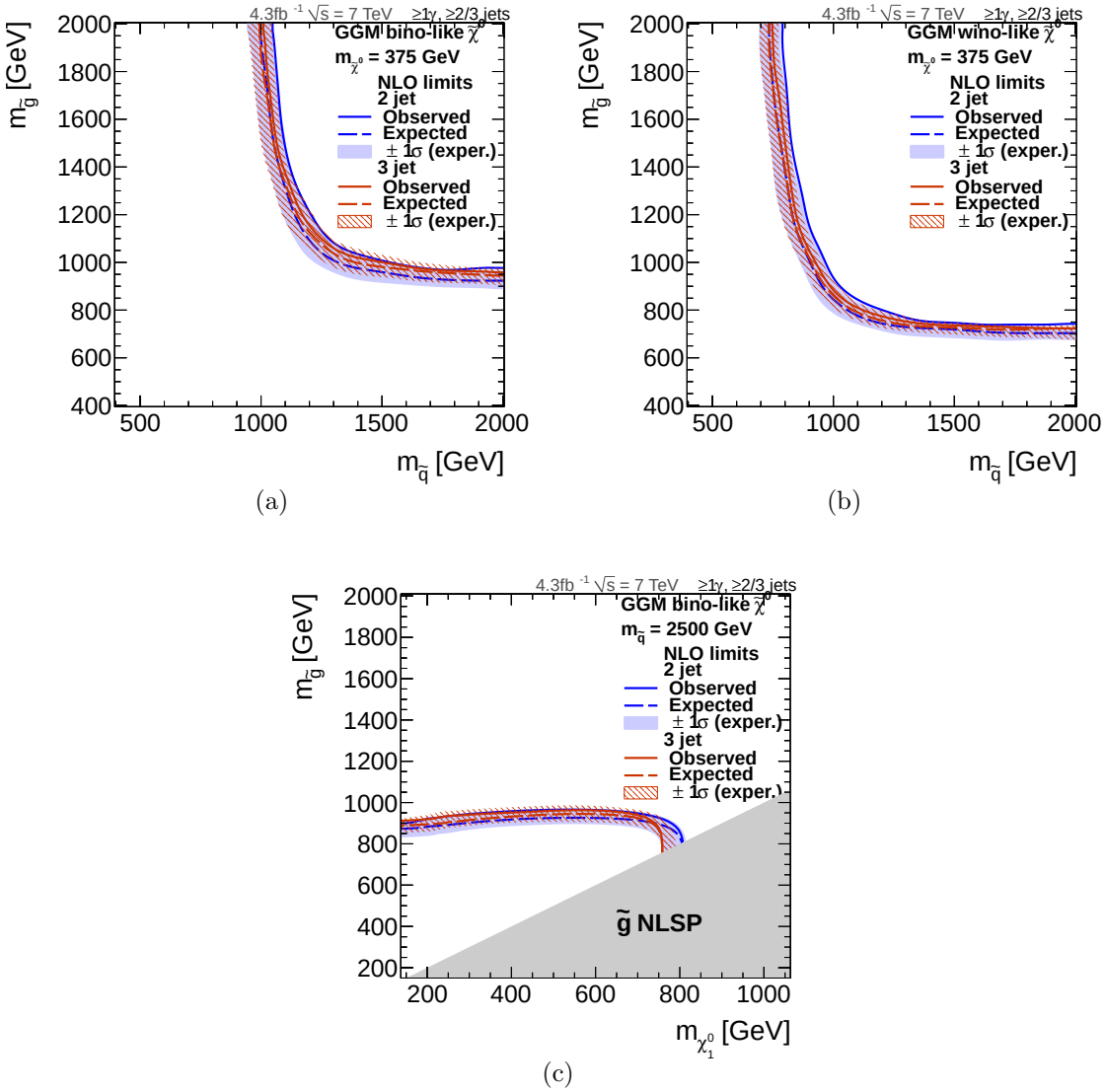

Figure A.19: Comparison of the resulting 95% CL exclusion limits between the ≥2 jet and ≥3 jet selection in the squark-gluino mass plane of a (a) bino- and (b) wino-like neutralino with $M_{\tilde{\chi}_1^0} = 375$ GeV and (c) in the neutralino-gluino mass plane of a bino-like neutralino. The shaded uncertainty band around the exclusion contours corresponds to the experimental uncertainties on the acceptance.

A. APPENDIX

List of Figures

List of Tables

LIST OF TABLES

References

[1] H. Spiesberger, M. Spira, and P. Zerwas, "The Standard model: Physical basis and scattering experiments," arXiv:hep-ph/0011255 [hep-ph]. 5

[2] **UA1** Collaboration, G. Arnison *et al.*, "Experimental observation of isolated large transverse energy electrons with associated missing energy at s**(1/2) = 540-GeV," *Phys. Lett.* **B122** (1983) 103–116. 5

[3] **UA1** Collaboration, G. Arnison *et al.*, "Experimental observation of lepton pairs of invariant mass around 95-GeV/c**2 at the CERN SPS collider," *Phys. Lett.* **B126** (1983) 398–410. 5

[4] **CDF** Collaboration, F. Abe *et al.*, "Observation of top quark production in $\bar{p}p$ collisions," *Phys.Rev.Lett.* **74** (1995) 2626–2631, arXiv:hep-ex/9503002 [hep-ex]. 5

[5] **D0** Collaboration, S. Abachi *et al.*, "Observation of the top quark," *Phys.Rev.Lett.* **74** (1995) 2632–2637, arXiv:hep-ex/9503003 [hep-ex]. 5

[6] **DONUT** Collaboration, K. Kodama *et al.*, "Observation of tau neutrino interactions," *Phys.Lett.* **B504** (2001) 218–224, arXiv:hep-ex/0012035 [hep-ex]. 5

[7] P. Meade, N. Seiberg, and D. Shih, "General Gauge Mediation," *Prog.Theor.Phys.Suppl.* **177** (2009) 143–158, arXiv:0801.3278 [hep-ph]. 5, 19, 20

[8] J. T. Ruderman and D. Shih, "General Neutralino NLSPs at the Early LHC," arXiv:1103.6083 [hep-ph]. 5, 21, 22, 23

[9] Y. Kats, P. Meade, M. Reece, and D. Shih, "The Status of GMSB After 1/fb at the LHC," arXiv:1110.6444 [hep-ph]. 5, 20, 21, 22, 23, 24, 118

[10] D. Griffiths, *Introduction to Elementary Particles*. John Wiley Sons, New York, USA, 1987. 5

[11] S. P. Martin, "A Supersymmetry primer," arXiv:hep-ph/9709356 [hep-ph]. 5

[12] I. Aitchison, *Supersymmetry in Particle Physics: An Elementary Introduction*. Cambridge Univ. Press, Cambridge, 2007. 5

[13] K. Nakamura and Particle Data Group, "Review of Particle Physics," *Journal of Physics G: Nuclear and Particle Physics* **37** no. 7A, (2010) 075021. http://stacks.iop.org/0954-3899/37/i=7A/a=075021. 7, 10

[14] P. W. Higgs, "Broken Symmetries and the Masses of Gauge Bosons," *Phys. Rev. Lett.* **13** (Oct, 1964) 508–509. 7

[15] F. Englert and R. Brout, "Broken Symmetry and the Mass of Gauge Vector Mesons," *Phys. Rev. Lett.* **13** (Aug, 1964) 321–323. http://link.aps.org/doi/10.1103/PhysRevLett.13.321. 7

[16] G. S. Guralnik, C. R. Hagen, and T. W. B. Kibble, "Global Conservation Laws and Massless Particles," *Phys. Rev. Lett.* **13** (Nov, 1964) 585–587. http://link.aps.org/doi/10.1103/PhysRevLett.13.585. 7

[17] Imperial College London. http://www.hep.ph.ic.ac.uk/cms/physics/higgs.html(13.11.2011). 8

[18] **LEP Working Group for Higgs boson searches, ALEPH , DELPHI, L3, OPAL** Collaboration, R. Barate *et al.*, "Search for the standard model Higgs boson at LEP," *Phys.Lett.* **B565** (2003) 61–75, arXiv:hep-ex/0306033 [hep-ex]. 8

[19] **CMS** Collaboration, "Combination of SM Higgs Searches," *CMS Physics Analysis Summary* **CMS-PAS-HIG-11-032** (2011) . http://cdsweb.cern.ch/record/1406347. 9

[20] **ATLAS** Collaboration, "Combination of Higgs Boson Searches with up to 4.9 fb-1 of pp Collisions Data Taken at a center-of-mass energy of 7 TeV with the ATLAS Experiment at the LHC," *Atlas Conference Note* **ATLAS-CONF-2011-163** (2011) . http://cdsweb.cern.ch/record/1406358. 9

[21] S. Glashow, "Partial-symmetries of weak interactions," **22** (Feb., 1961) 579–588. 9

[22] S. Weinberg, "A Model of Leptons," *Phys. Rev. Lett.* **19** (Nov, 1967) 1264–1266. http://link.aps.org/doi/10.1103/PhysRevLett.19.1264. 9

[23] A. Salam and J. C. Ward, "Electromagnetic and weak interactions," *Phys.Lett.* **13** (1964) 168–171. 9

[24] M. Gell-Mann, "A Schematic Model of Baryons and Mesons," *Phys.Lett.* **8** (1964) 214–215. 10

[25] D. Hooper, "Indirect searches for dark matter: Signals, hints and otherwise," arXiv:0710.2062 [hep-ph]. 12

[26] N. Jarosik, C. Bennett, J. Dunkley, B. Gold, M. Greason, *et al.*, "Seven-Year Wilkinson Microwave Anisotropy Probe (WMAP) Observations: Sky Maps, Systematic Errors, and Basic Results," *Astrophys.J.Suppl.* **192** (2011) 14, arXiv:1001.4744 [astro-ph.CO]. 12

[27] U. Amaldi, W. de Boer, and H. Furstenau, "Comparison of grand unified theories with electroweak and strong coupling constants measured at LEP," *Phys. Lett.* **B260** (1991) 447–455. 14

[28] F. D. Steffen, "Supersymmetric dark matter candidates: The Lightest neutralino, the gravitino, and the axino," arXiv:0711.1240 [hep-ph]. 14, 17

[29] G. Giudice and R. Rattazzi, "Theories with gauge mediated supersymmetry breaking," *Phys.Rept.* **322** (1999) 419–499, arXiv:hep-ph/9801271 [hep-ph]. 19

[30] S. P. Martin and P. Ramond, "Sparticle Spectrum Constraints," *Phys.Rev.* **D48** (1993) 5365–5375, arXiv:hep-ph/9306314 [hep-ph]. 22

[31] **ATLAS** Collaboration, G. Aad *et al.*, "Search for squarks and gluinos using final states with jets and missing transverse momentum with the ATLAS detector in sqrt(s) = 7 TeV proton-proton collisions," arXiv:1109.6572 [hep-ex]. 23

[32] **CMS** Collaboration, "Search for supersymmetry in all-hadronic events with missing energy,," *CMS Physics Analysis Summary* **CMS PAS SUS-11-004** (2011) . http://cdsweb.cern.ch/record/1378478. 23

[33] **CDF** Collaboration, D. Acosta *et al.*, "Search for anomalous production of diphoton events with missing transverse energy at CDF and limits on gauge-mediated supersymmetry-breaking models," *Phys.Rev.* **D71** (2005) 031104, arXiv:hep-ex/0410053 [hep-ex]. 23, 115

[34] **D0** Collaboration, V. M. Abazov *et al.*, "Search for diphoton events with large missing transverse energy in 6.3 fb^{-1} of $\mathbf{p\bar{p}}$ collisions at $\sqrt{\mathbf{s}} = \mathbf{1.96}$ TeV," *Phys.Rev.Lett.* **105** (2010) 221802, arXiv:1008.2133 [hep-ex]. 23, 115

[35] D. Alves, N. Arkani-Hamed, S. Arora, Y. Bai, M. Baumgart, *et al.*, "Simplified Models for LHC New Physics Searches," arXiv:1105.2838 [hep-ph]. 23

[36] W. Beenakker, R. Hopker, and M. Spira, "PROSPINO: A Program for the production of supersymmetric particles in next-to-leading order QCD," arXiv:hep-ph/9611232 [hep-ph]. 24

[37] L. Evans and P. Bryant, "LHC Machine," *JINST* **3** (2008) S08001. 27

[38] **ATLAS** Collaboration, "The ATLAS experiment at the CERN Large Hadron Collider," *JINST* **3** (2008) S08003. 28

[39] **CMS** Collaboration, "The CMS experiment at the CERN LHC," *JINST* **3** (2008) S08004. 28, 30, 32, 35

[40] **LHCb** Collaboration, "The LHCb Detector at the LHC," *JINST* **3** (2008) S08005. 28

[41] **TOTEM** Collaboration, "The TOTEM Experiment at the CERN Large Hadron Collider," *JINST* **3** (2008) S08007. 28

[42] **ALICE** Collaboration, "The ALICE Experiment at the CERN LHC," *JINST* **3** (2008) S08002. 28

[43] CERN, "The four main LHC experiments,". http://cdsweb.cern.ch/record/40525. 28

[44] LHC Programme Coordination, "LHC Luminosity Plots for the 2011 Proton Run,". http://lpc.web.cern.ch/lpc/. 29

[45] **CMS** Collaboration, "CMS Tracking Performance Results from early LHC Operation," *Eur. Phys. J.* **C70** (2010) 1165–1192, arXiv:1007.1988 [physics.ins-det]. 32

[46] **CMS** Collaboration, "Electromagnetic calorimeter commissioning and first results with 7 TeV Data," *CMS NOTE* **2010/012** (2010) . 33

[47] **CMS** Collaboration, "CMS TriDAS project: Technical Design Report. Volume 1, The Trigger Systems," *CERN-LHCC-2000-038* (2011) . 36

[48] **CMS** Collaboration, Trigger and Data Acquisition Group, "The CMS high level trigger," *Eur. Phys. J.* **C46** (2006) 605–667, arXiv:hep-ex/0512077. 36

[49] **CMS** Collaboration, "Identification and Filtering of Uncharacteristic Noise in the CMS Hadron Calorimeter," *JINST* **5** (2009) . 37

[50] **CMS** Collaboration, "Isolated Photon Reconstruction and Identification at $\sqrt{s} = 7$ TeV," *CMS Physics Analysis Summary* **CMS-PAS-EGM-10-006** (2010) . http://cdsweb.cern.ch/record/1324545. 37

[51] M. Cacciari, G. P. Salam, and G. Soyez, "The anti-k_t jet clustering algorithm," 2008. doi:10.1088/1126-6708/2008/04/063. 38

[52] **CMS** Collaboration, "Jet Plus Tracks Algorithm for Calorimeter Jet Energy Corrections in CMS," *CMS Physics Analysis Summary* **CMS-PAS-JME-09-002** (2009) . http://cdsweb.cern.ch/record/1190234. 38

[53] **CMS** Collaboration, "Particle–Flow Event Reconstruction in CMS and Performance for Jets, Taus, and $\not\!\!E_{\mathrm{T}}$," *CMS Physics Analysis Summary* **CMS-PAS-PFT-09-001** (2009) . http://cdsweb.cern.ch/record/1194487. 38, 46

[54] **CMS** Collaboration, "Determination of jet energy calibration and transverse momentum resolution in CMS," *JINST* **6** no. 11, (2011) P11002. http://stacks.iop.org/1748-0221/6/i=11/a=P11002. 38, 57

[55] CMS Jet Identification, "https://twiki.cern.ch/twiki/bin/view/CMS/JetID." 2010. 39

[56] **CMS** Collaboration, "Photon reconstruction and identification at $\sqrt{s} = 7$ TeV," *CMS Physics Analysis Summary* **CMS-PAS-EGM-10-005** (2010) . http://cdsweb.cern.ch/record/1279143. 40

[57] M. Paulini (ed.) *et al.*, "Search for Gauge Mediated Supersymmetry Breaking Using Two Photons and Missing Transverse Energy," *CMS Note* **2011/515** (2012) . 41, 93

[58] **CMS** Collaboration, "Missing ET in 0.9 and 2.36 TeV pp Collisions," *CMS Physics Analysis Summary* **CMS-PAS-JME-10-002** (2010) . http://cdsweb.cern.ch/record/1247385. 46

[59] **CMS** Collaboration, "Missing transverse energy performance of the CMS detector," *JINST* **6** no. 09, (2011) P09001. http://stacks.iop.org/1748-0221/6/i=09/a=P09001. 46, 47, 50, 68, 76

[60] **CMS** Collaboration, "Performance of Track-Corrected Missing E_{T} in CMS," *CMS Physics Analysis Summary* **CMS-PAS-JME-09-010** (2009) . http://cdsweb.cern.ch/record/1228297. 46

[61] **CMS** Collaboration, "Jet Performance in pp Collisions at $\sqrt{s}$=7 TeV," *CMS Physics Analysis Summary* **CMS-PAS-JME-10-003** (2010) . http://cdsweb.cern.ch/record/1279362. 47

[62] C. Autermann, J. Damgov, U. Gebbert, S.-W. Lee, P. Schleper, and D. Wang, "Type-I and Type-II CaloMET performances in 7 TeV data," *CMS Note* **2010/131** (2010) . 47

[63] C. Autermann, U. Gebbert, C. Sander, P. Schleper, and H. Stadie, "Derivation of type-II corrections from $Z \to ee$ events in 7 TeV data for Calo- and Pf MET," *CMS Note* **2010/396** (2010) . 47, 56

[64] **CMS** Collaboration, "Missing Transverse Energy Performance in Minimum-Bias and Jet Events from Proton-Proton Collisions at $\sqrt{s}$ =7 TeV," *CMS Physics Analysis Summary* **CMS-PAS-JME-10-004** (2010) . http://cdsweb.cern.ch/record/1279142. 47

[65] T. Sjöstrand, S. Mrenna, and P. Skands, "PYTHIA 6.4 Physics and Manual; v6.420, tune D6T," *JHEP* **05** (2006) 026, arXiv:hep-ph/0603175. 58, 91, 96, 150

[66] **CMS** Collaboration, "Plans for Jet Energy Corrections at CMS," *CMS Physics Analysis Summary* **JME-07-002** (2007) . http://cdsweb.cern.ch/record/1194485. 60

[67] F. Rebassoo and S. Eno, "MET resolution vs. sumEt in Minimum Bias 7 TeV events," *CMS Analysis Note 2010/142* (2010) . 68, 69

[68] **CMS** Collaboration, "Commissioning of b-jet identification with pp collisions at $\sqrt{s} = 7$ TeV," *CMS Physics Analysis Summary* **CMS-PAS-BTV-10-001** (2010) . http://cdsweb.cern.ch/record/1279144. 71

[69] **CMS** Collaboration, "Algorithms for b Jet Identification in CMS," *CMS Physics Analysis Summary* **CMS-PAS-BTV-09-001** (2009) . http://cdsweb.cern.ch/record/1194494. 71

[70] **D0 Collaboration** Collaboration, R. Engelmann *et al.*, "Response of a highly segmented extruded lead glass calorimeter to electrons and pions between 15-GeV/c and 45-GeV/c," *Nucl.Instrum.Meth.* **216** (1983) 45. 73

[71] H. Liu, K. Hatakeyama, U. Gebbert, K. Theofilatos, W. Flanagan, A. Gurrola, and T. Kamon, "Studies on ECAL Dead and Masked Channel Contributions to High MET and MHT," *CMS Note* **2010/354** (2010) . 76

[72] **CMS** Collaboration, CMS, "Search for Supersymmetry in *pp* Collisions at $\sqrt{s} = 7$ TeV in Events with Two Photons and Missing Transverse Energy," *Phys. Rev. Lett.* **106** (2011) 211802, arXiv:1103.0953 [hep-ex]. 77

[73] **CMS** Collaboration, CMS, "Search for supersymmetry in events with a lepton, a photon, and large missing transverse energy in pp collisions at sqrt(s) = 7 TeV," *JHEP* **1106** (2011) 093, arXiv:1105.3152 [hep-ex]. 77, 115

[74] **CMS** Collaboration, "Search for Supersymmetry in Events with Photons, Jets and Missing Energy," *CMS Physics Analysis Summary* **CMS-PAS-SUS-11-009** (2011) . http://cdsweb.cern.ch/record/1377324. 77, 118

[75] C. Autermann, U. Gebbert, and P. Schleper, "Search for Supersymmetry in Events with one Photon, Jets and Missing Transverse Energy," *CMS Note* **2011/213** (2011) . 77, 118

[76] LP 11, "25th International Symposium On Lepton Photon Interactions At High Energy," *Mumbai, India* **SPIRES Conf Num: C11/08/22.1** (2011) . 77, 118

[77] Supersymmetry 2011 (SUSY11), "19th International Conference On Supersymmetry And Unification Of Fundamental Interactions," *Batavia, Illinois, USA* **SPIRES Conf Num: C11/08/28.1** (2011) . 77, 118

[78] C. Autermann, U. Gebbert, M. Hoffmann, and P. Schleper, "Search for Supersymmetry in Events with one Photon, Jets and Missing Transverse Energy," *CMS Note* **2011/512** (2012) . 77

[79] D. Jang, "Trigger Performance,". https://twiki.cern.ch/twiki/bin/viewauth/CMS/RA3PhotonTriggerPerformanceV2. 80

[80] J. Alwall *et al.*, "MadGraph/MadEvent v4: The New Web Generation," *JHEP* **09** (2007) 028, arXiv:0706.2334 [hep-ph]. 96

[81] L. Moneta, K. Belasco, K. Cranmer, S. Kreiss, A. Lazzaro, D. Piparo, G. Schott, W. Verkerke, and M. Wolf, "The RooStats Project," arXiv:1009.1003v2 [physics.data-an]. 102

[82] **CMS** Collaboration, Higgs Physics Analysis Group, "Higgs Analysis Combined Limit,". https://twiki.cern.ch/twiki/bin/view/CMS/SWGuideHiggsAnalysisCombinedLimit. 102, 105

[83] **ATLAS** Collaboration, "Search for Diphoton Events with Large Missing Transverse Momentum in 1 fb^{-1} of 7 TeV Proton-Proton Collision Data with the ATLAS Detector," arXiv:1111.4116 [hep-ex]. 116

[84] **CMS** Collaboration, "Search for Supersymmetry in Events with Photons, Jets and Missing Energy," *CMS Physics Analysis Summary* **CMS-PAS-SUS-12-001** (2012) . 116, 118

Danksagung

Ich möchte mich gerne bei allen Personen bedanken, die mich in den letzten Jahren begleitet und zum Gelingen der Arbeit beigetragen haben. Insbesondere geht mein Dank an:

- Prof. Dr. Peter Schleper - vielen Dank für die Gelegenheit, die Arbeit in Deiner Gruppe anfertigen zu können. Die vielen wertvollen Hinweise und nicht zuletzt Deine ansteckende Begeisterung für die Teilchenphysik, haben mich in den letzten Jahren immer wieder motiviert.

- Prof. Dr. Teruki Kamon - thank you very much for acting as a referee of my thesis and for always timely response during the review process. It was really a pleasure to see you in Hamburg for my thesis defence!

- Prof. Dr. Johannes Haller and Dr. Isabell Melzer-Pellmann - vielen Dank für die Übernahme der Gutachten der Disputation.

- Dr. Christian Autermann - herzlichen Dank für die Begleitung und Betreuung meiner Arbeit über die ganze Zeit, viele sinnvolle und richtunggebende Hinweise und Verbesserungsvorschläge zu den Analysen und das viele Korrekturlesen in der Endphase.

- Jun.-Prof. Dr. Christian Sander und Dr. Hartmut Stadie - ich danke Euch für die geduldige Unterstützung bei Fragen jeglicher Art von technischen Problemen bis zum Korrekturlesen. Gerade wenn mal nicht alles so lief wie gewünscht, konnte man sich immer auf Euch verlassen!

DANKSAGUNG

- the various members of the CMS JetMET and SUSY working groups - thanks for many fruitful discussions and elaborate comments and suggestions for further studies. Here I would especially like to thank Prof. Dr. Sarah Eno, Prof. Dr. Teruki Kamon, and Prof. Dr. Kenichi Hatakeyama as well as Prof. Dr. Yuri Gershtein, Dr. David A. Mason, and Prof. Dr. Manfred Paulini.

- die ganze CMS Gruppe der Universität Hamburg: Vielen Dank für die stets nette Arbeitsatmosphäre, viele ermunternde Gespräche und die große Hilfsbereitschaft bei Problemen aller Art.

- meine gesamte Familie, insbesondere natürlich an meine Eltern und an Matthias: Vielen Dank für Eure Unterstützung in den vergangenen Jahren und natürlich die große Hilfe bei der Verteidigung.